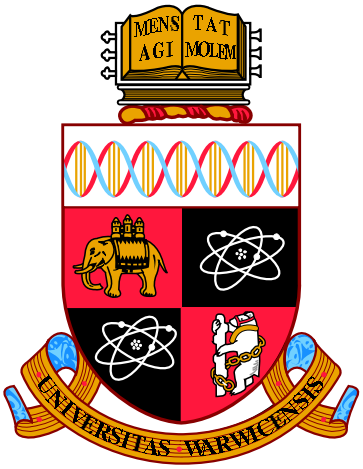

Nano-scale Computational Fluid Dynamics with Molecular Dynamics Pre-simulations

by

David M. Holland

Thesis

Submitted to the University of Warwick

for the degree of

Doctor of Philosophy

School of Engineering

June 2015

THE UNIVERSITY OF WARWICK

Contents

Acknowledgments

Firstly, I would like to thank my supervisor Dr Duncan Lockerby for his constant help, encouragement, enthusiasm and ideas; he truly is an inspiration.

Also, I would like to thank the other members of the Micro and Nano Flows for Engineering research group. Specifically, Dr Matthew Borg for always being more than willing to help with any problems and molecular dynamics simulations, and Professor Jason Reese for all of the insightful discussions and his ruthless attention to detail. My fellow PhD students Dave and Alex, plus post docturate researchers Dr Neil Haria and Dr Ajit Mahendra who have provided many fruitful discussions.

Finally, I am very grateful to all of my family, friends and girlfriend for their unwavering encouragement and support.

Declarations

This thesis is submitted to the University of Warwick in support of my application for the degree of Doctor of Philosophy. It has been composed by myself and has not been submitted in any previous application for any degree.

The work presented (including data generated and data analysis) was carried out by the author except in the cases outlined below:

List of data provided and/or analysis carried out by collaborators.

The Molecular Dynamics simulations, used to validate the model created in this thesis and collect data to be input into the model, were performed by Dr. M. K. Borg.

Parts of this thesis have been published by the author:

1. D. M. Holland, D. A. Lockerby, M. K. Borg, J. M. Reese. Molecular dynamics pre-simulation methodology for nano-scale computational fluid dynamics. *11th. World Congress on Computational Mechanics (WCCM XI), Barcelona, Spain, 2014.*

2. D. M. Holland, D. A. Lockerby, M. K. Borg, W. D. Nicholls, J. M. Reese. Molecular dynamics pre-simulations for nanoscale computational fluid dynamics. *Microfluidics and Nanofluidics*, 18(3):461-474, 2015.

3. D. M. Holland, M. K. Borg, D. A. Lockerby, J. M. Reese. Enhancing nanoscale computational fluid dynamics with molecular pre-simulations: unsteady problems and design optimisation. *under review.*

4. D. Stephenson, A. Patronis, D. M. Holland, D. A. Lockerby. Generalizing

Murrays law: an optimisation principle for fluidic networks of all shapes and sizes. *under review*.

Abstract

A procedure for using Molecular Dynamics (MD) simulations to provide essential fluid and interface properties for subsequent use in Computational Fluid Dynamics (CFD) calculations of nano-scale fluid flows is presented. The MD pre-simulations enable an equation of state, constitutive relations, and boundary conditions to be obtained for any given fluid/solid combination, in a form that can be conveniently implemented within an otherwise conventional Navier-Stokes solver.

The results presented demonstrate that these enhanced CFD simulations are capable of providing good flow field results in a range of complex geometries at the nano-scale. Comparison for validation is with full-scale MD simulations here, but the computational cost of the enhanced CFD is negligible in comparison with the MD. It is shown that this enhanced CFD can predict unsteady nano-scale flows in non-trivial geometries. A converging-diverging nano-scale channel is modelled where the fluid flow is driven by a time-varying body force. The time-dependent mass flow rate predicted by the enhanced CFD agrees well with a MD simulation of the same configuration. Conventional CFD predictions of the same case are wholly inadequate.

It is demonstrated that accurate predictions can be obtained in geometries that are more complex than the planar MD pre-simulation geometry that provides the nano-scale fluid properties. The robustness of the enhanced CFD is tested by application to water flow along a (15,15) carbon nanotube (CNT) and it is found that useful flow information can be obtained.

The enhnaced CFD model is applied as a design optimisation tool on a bifurcating two-dimensional channel, with the target of maximising mass flow rate for a fixed total volume and applied pressure. At macro scales the optimised geometry agrees well with Murray's law for optimal branching of vascular networks; however, at the nano-scale, the optimum result deviates from Murray's law, and a corrected equation is presented. However, it is found that as the mass flow rate increases through the channel high pressure losses occur at the junction of the network. These high pressure losses also have an impact on the optimal design of a network.

List of Figures

List of Tables

Nomenclature

Acronyms

CA	Continuous micro solution — asynchronous coupling
CAI	Continuous micro solution — asynchronous intermittent coupling
CFD	Computational fluid dynamics
CI	Continuous micro solution — intermittent coupling scheme
CNT	Carbon nanotube
CPU	Computational processing unit
DD	Domain decomposition
EMD	Equilibrium molecular dynamics
GPU	Graphical processing unit
HI	Heterogeneous micro solution — intermittent coupling scheme
HMM	Heterogeneous multiscale method
HSI	Hybrid solution interface
IMM	Internal-flow multiscale method
LJ	Lennard-Jones
MD	Molecular dynamics
MEMS	Microelectromechanical systems
MPI	Message passing interface
NEMD	Non-equilibrium molecular dynamics

NEMS	Nanoelectromechanical systems
NPT	Isothermal-isobaric ensembe
NVE	Microcanonical ensemble
NVT	Canonical ensemble
PISO	Pressure implicit with splitting of operators
PWC	Point-wise coupling
RDF	Radial distribution function
SIMPLE	Semi-implicit method for pressure-linked equations
SIMPLER	SIMPLE revised
SPC	Simple point charge
SPC/E	Extended simple point charge
TIP3P	Transerable intermolecular potential 3 points
TIP4P	Transerable intermolecular potential 4 points
TIP4P/2005	2005 version of TIP4P
TIP5P	Transerable intermolecular potential 5 points
WPOD	Window proper orthogonal decomposition

Symbols

$\bar{\rho}_i$	Volume average density [kg/m^3]
$\bar{F}$	Magnitude of force [N]
$\bar{v}$	Average velocity [m/s]
δ	Surface displacement [m]
Δt	Time-step [s]
$\dot{\gamma}$	Strain rate [1/s]
$\dot{m}$	Mass flow rate [kg/s]
$\hat{\mathbf{f}}_i$	Intermolecular force on molecule i [N]

$\mathbf{f}_{ext}$	External body force [N]
$\mathbf{f}_i$	Force on molecule i [N]
$\mathbf{n}$	Normal vector [-]
$\mathbf{r}_i$	Position of molecule i [m]
$\mathbf{T}$	Stress tensor [Pa]
$\mathbf{v}$	Velocity [m/s]
$\mathbf{v}_i$	Velocity in cell i, velocity of molecule i [m/s]
μ	Dynamic viscosity [Pa s]
$\Omega_{C,D,O}$	Continuum, discrete and overlap regions [-]
ρ	Density [kg/m^3]
ρ_0	Reference density [kg/m^3]
ρ_i	Density in cell i [kg/m^3]
σ	Finite distance at which the inter-particle potential is zero [m]
σ_s	Standard deviation [m]
τ	Time constant that defines the coupling strength of heat bath [s]
τ_{xy}	Shear stress [Pa]
ε	Depth of the potential well [J]
ε_0	Vacuum permittivity [C^2/(Nm^2)]
ξ	Slip length [m]
f_{f-s}	Friction force between fluid and solid wall [N]
g	Gearing [-]
h	Channel width [m]
K	Pressure loss coefficient [-]
L	Length [m]
m_i	Mass of molecule i [kg]

N	Number of [-]
P	Power [W]
p	Pressure [Pa]
p_0	Reference pressure [Pa]
q_i	Charge of a site in a molecule [C]
R	Flow resistance [1/m]
r_c	Cut-off separation [m]
r_{ij}	Distance between molecules i and j [m]
S_i	Control surface [m^2]
T	Temperature [°C], Period [s]
t	Time [s]
$U(r_{ij})$	Potential energy between two molecules separated by r_{ij} [J]
V	Volume [m^3]
V_i	Control volume [m^3]
v	Magnitude of velocity [m/s]

Chapter 1

Introduction

1.1 Nanofluidics

Nanofluidics is the study of the behaviour of fluids confined in structures of length scales on the order of nanometers. At these length scales surface effects from the wall dominate the behaviour of the fluid. The standard no-slip boundary condition, which is used at larger length scales, is no longer applicable. Also, fluid molecules form layers at the interfaces between a fluid and a solid and where two fluids meet, this causes variations in viscosity and stresses within the fluid that do not conform to the typical assumptions for modelling fluids.

Nanofluidic technologies have recently received significant attention due to the many different possible applications. These applications take advantage of the different physical effects that dominate at small scales. Examples can be found in air and water purification [3, 93], heat removal and control in high heat-flux systems such as nuclear reactors, micro/nano electro mechanical systems (MEMS/NEMS), and micro chemical reactors [128, 156].

The design of these technologies would be greatly facilitated by performing numerical simulations that predict mass flow rates and heat transfer. Computational fluid dynamics (CFD) has been successfully applied to a range of different engineering problems such as aerodynamics and modelling heart vessels. However, when trying to model at the nano/micro scale, where the scale is comparable to those of the molecular interactions, there exist non-continuum effects, such as molecular layering and velocity slip near to liquid-solid interfaces, which causes the continuum assumption to falter [14].

Molecular Dynamics (MD) [5, 121] can be used to perform highly-detailed simulations of nano-scale systems; it has been successfully used to study the be-

haviour of protein folding [77], crystal formation [114] and chemical reactions [132]. The drawback is that MD is extremely computationally intensive, especially when used to model systems relevant to engineering applications, typically comprising hundreds of thousands of molecules. There is a large amount of noise in the measurement of bulk properties of the fluid (such as velocity, viscosity and stress), therefore the simulations have to be performed over long periods of time to average these properties. For example, to simulate $200\,\mathrm{nm}^3$ of water for 1 nano second, with a modern MD code running on 8 CPUs in parallel, can require approximately 2 days of computational time. To simulate the liquid over much larger time and space scales is beyond the reach of current computational capabilities (even with the improved computational efficiency offered by Graphical Processing Units, GPUs). This certainly prevents using such simulations within a practical iterative design process.

In an attempt to strike a balance between CFD and MD, Hybrid methods have been in development in which continuum descriptions of the flow are combined with molecular descriptions. These take advantage of the detail of molecular but reduce the computational cost by using the continuum, for a review see [99]. There are two main approaches to hybrid methodologies: domain decompostion (DD) [108] and Heterogeneous Multiscale Method (HMM) [4, 124], also known as Point-wise coupling (PWC) [9].

The continuum fluid assumptions become inaccurate for gas flows as the smallest characteristic scale of the geometry (e.g. channel height) approaches the mean distance between molecular collisions (i.e. the mean free path) [123]. When modelling dense liquids (as in this thesis) there is not a well-defined condition for when the fluid assumptions become inaccurate. However, it appears that they fail when water is confined in channels of width ~1–2 nm (see [17] and references therein), and MD simulations have been used to show that Lennard-Jones fluids confined in geometries of ~2–3 nm still show continuum behaviour [59, 134, 147]. At the nano-scale the fluid molecules form layers parallel to an interface, which causes the strain rate to vary rapidly within several molecular diameters [146]. These large variations mean the stress no longer has local linear behaviour [25, 145].

1.2 Thesis overview

In chapter 2, a description of the different numerical methods that can be used to model nano-scale confined fluids is given. A presentation of the finite volume CFD and the MD methodologies that is used in the rest of the thesis is given. Also, a

literature review of the hybrid methodologies that have been proposed is provided.

In chapter 3 is a discussion the possible methods that could be used to obtain fluid properties to be input into a CFD model. A convenient pre-simulation MD framework that enables us to measure CFD-type properties (e.g. boundary conditions and constitutive relations) for a given solid/liquid combination is proposed.

In chapter 4 is a demonstration that these fluid properties can be used to obtain highly accurate CFD predictions in complex geometries at the nano-scale, provided that a significant portion of the flow exhibits continuum bulk-like behaviour. This is distinct from previous studies (e.g. [161]) that focused mainly on 1D flow configurations. It is also shown that the CFD model is robust enough to predict the unsteady flow behaviour of a fluid in a non-trivial geometry (a converging-diverging channel), using various forms of applied forcing to generate unsteadiness within it.

In chapter 5, the CFD model is applied to highly non-continuum 3D flows, where no significant bulk flow exists (such as flow through some small diameter carbon nanotubes), qualitatively accurate, and so useful, CFD predictions can be obtained. Importantly, it is shown that accurate CFD predictions can be obtained in cases that are more complex than the MD flow configuration from which the CFD fluid parameters were obtained.

In chapter 6, the CFD model is shown to be efficient enough to be applied to the design optimisation of a small fluidic network. It is found that applying slip-boundary conditions has an affect on the optimal design of a network of channels. Equations are proposed to extend the well-known Murray's law to predict the optimal geometry of a bifurcating channel at the nanoscale. However, we find that as the mass flow rate increases, when high slip lengths are applied, the pressure loss at the junction became significant, meaning that the predictions from the simple analytical model became inaccurate.

In chapter 7, some concluding remarks are given and some future research ideas to develop our model further are proposed.

Chapter 2

Numerical methods for simulating liquids at the nano-scale

2.1 Introduction

In this thesis, both Molecular dynamics (MD) and Computational fluid dynamics (CFD) are used to describe flows at the nano-scale. In this chapter both of these numerical methodologies are described and we follow this with some of the methodologies that have been created over the past 15 years to couple the two together; these are known as hybrid atomistic-continuum methods.

There have been many different pieces of software developed for performing CFD simulations (e.g. ANSYS Fluent, COMSOL, OpenFOAM and Star-CCM+) and for MD simulations (e.g. LAMMPS, GROMACS, NAMD, AMBER, DL_POLY), which are all widely used within industry and academia.

In this thesis, the OpenFOAM software libraries [112] are used for both the CFD and MD simulations. More specifically, the *sonicLiquidFoam* solver for the CFD simulations, as described in section 2.2, and the *mdFoam* solver [23, 89, 90] for the MD simulations, as described in section 2.3.

The OpenFOAM framework was chosen for this work as it is open-source, developed in the C++ language, and is easily parallelisable using MPI libraries. This is ideal for the purposes of this thesis as the ability to customise the solvers, create boundary conditions for CFD, create measurement tools and controllers for MD, and perform large simulations in parallel over many processors for both CFD and MD is required. As both methods are in the same framework, there is more

consistency between the code for both CFD and MD, meaning that any coupling between the two becomes much simpler.

2.2 Computational fluid dynamics (CFD)

In this section the fundamentals of CFD are described, with emphasis on the implementation in OpenFOAM of the laminar, compressible *sonicLiquidFoam* solver, which will be used in this thesis. More in-depth detail on CFD can be found in the books [40, 151] and more details on the implementations in OpenFOAM can be found in the programmers guide and the user guide [110, 111].

2.2.1 Navier-Stokes equations

The fundamental equations of motion for a fluid are the Navier-Stokes equations:

$$\rho\left(\frac{\partial \mathbf{v}}{\partial t} + \mathbf{v}\cdot\nabla\mathbf{v}\right) = -\nabla p + \nabla\cdot\mathbf{T} + \mathbf{f}_{ext}, \tag{2.1}$$

where ρ is the density, t is time, $\mathbf{v}$ is the fluid velocity, p is the pressure, $\mathbf{T}$ is the stress tensor and $\mathbf{f}_{ext}$ is a body force. In this work we assume that the liquid is weakly compressible [135] and Newtonian, therefore, $\nabla\cdot\mathbf{T} = \nabla\cdot\mu\nabla\mathbf{v}$, where μ is the dynamic viscosity [55]. The derivation of these equations depends on the continuum assumption, as discussed in section 1, is not always applicable at the nano-scale.

The ratio of inertial forces to viscous forces, which is a dimensionless quantity, is known as the Reynolds Number, $\mathrm{Re} = \rho v L/\mu$, where L is a characteristic length scale and $v = |\mathbf{v}|$. This is used to characterise flow conditions as either laminar or turbulent. In nano-scale flows, the characteristic length scale is $O(10^{-9})$ and the velocities are low, therefore, the Reynolds number is always small and thus the flow is always laminar. Due to this we have a Stokes flow and equation (2.1) can be simplified to

$$\rho\frac{\partial \mathbf{v}}{\partial t} = -\nabla p + \nabla\cdot\mu\nabla\mathbf{v} + \mathbf{f}_{ext}. \tag{2.2}$$

In addition to momentum conservation, the system must also adhere to mass conservation, which for a compressible fluid can be represented by

$$\frac{\partial \rho}{\partial t} + \nabla\cdot(\rho\mathbf{v}) = 0. \tag{2.3}$$

The *sonicLiquidFoam* solver was designed to model liquids which are weakly compressible and be able to resolve waves at a finite speed. To do this the equation of state (the relationship between pressure and density) is assumed to be a simple

barotropic function,

$$\frac{\partial \rho}{\partial p} = \frac{\rho}{K} = \psi, \tag{2.4}$$

where K is a compressibility constant; this is linearised to give

$$\rho = \rho_0 + \psi(p - p_0), \tag{2.5}$$

where ρ_0 and p_0 are reference density and pressure values such that $\rho(p_0) = \rho_0$. We choose to use this solver because, despite the low Mach numbers that we will be modelling, substantial fluid compressibility can occur due to high viscous forces at the nano-scale, as discussed by Gad-el-Hak in [43].

Other CFD solvers may model more complex physics such as heat transfer by incorporating an energy equation. This is not required for the cases modelled in this work but the methodologies could easily be extended to handle heat transfer.

2.2.2 Pressure calculation

In general, in CFD, the velocity field and the pressure fields are both unknown and dependent on each other. To get around this issue many different algorithms have been developed, such as: Pressure implicit with splitting of operators (PISO), Semi-implicit method for pressure-linked equations (SIMPLE), and SIMPLE revised (SIMPLER) loops. In the *sonicLiquidFoam* solver a PISO loop has been implemented to couple the equations, see Algorithm 1. In the PISO loop, a predictor-corrector loop is used. This means that the momentum equations are solved using an initial pressure field to give an approximate (predicted) velocity field. These velocities are then corrected using an equation for pressure. This correction is performed as many times as required until the continuity equation is satisfied; typically, only two corrections are required.

For transient and compressible models, an equation for pressure can be derived by taking the divergence of the momentum equations (2.1) and is simplified using equations for continuity (2.3) and density (2.5), giving a Poisson equation for pressure:

$$\nabla \cdot \nabla p = -\nabla^2 \cdot (\rho(\mathbf{u} \cdot \mathbf{u}) - \mu \nabla \mathbf{u}) + \frac{\partial^2 \rho}{\partial t^2}. \tag{2.6}$$

In the rest of this thesis equations (2.1), (2.3) and (2.6) will be collectively referred to as the Navier-Stokes equations.

Algorithm 1 PISO loop

```
initialise v
initialise p
while t < t_end do
    Solve continuity equation (2.3)
    Solve momentum equation (2.1)
    for n corrector loops do
        Calculate mass fluxes through cell faces
        Solve pressure equation (2.6)
        Correct mass fluxes through cell faces
        Correct velocity field with new pressure field
        Update boundary conditions
    end for
    Update density field, equation (2.5)
end while
```

2.2.3 Finite-volume method

There are many different numerical techniques developed for solving partial differential equations, such as: finite-difference, finite-volume, finite-element and spectral methods. Each of these have their own advantages and disadvantages; for example, spectral methods are extremely quick, but are not easily applied to complex geometry; whereas the finite-element method is very slow but is far more flexibly applied to complex geometries. Commonly, CFD packages use finite-volume methods to solve the Navier-Stokes equations as they are naturally conservative, simple to code and accurate [40, 151].

In the finite-volume method, the solution domain is split into small cells and the governing equations (in our case the Navier-Stokes equations) are then integrated and converted into surface integrals (via Gauss' theorem) for each cell. This means that equations are derived for each cell of the domain , which are collectively solved by some form of matrix inversion.

The two different types of grid that are commonly used to discretise the domain are co-located grids or staggered grids. In OpenFOAM a co-located grid is used; this means that the equations are solved at the cell centers and information is interpolated to the cell faces when required.

This method is now demonstrated by applying it to the continuity equation (2.3). The method is easily applied to the rest of the Navier-Stokes equations in the same way. For cell i with control volume V_i, equation (2.3) can be written as

$$\frac{\partial \rho_i}{\partial t} + \nabla \cdot (\rho_i \mathbf{v}_i) = 0. \tag{2.7}$$

where ρ_i and $\mathbf{v}_i$ are the density and velocity at the center of cell i. These equations are integrated over the cell:

$$\int_{V_i} \frac{\partial \rho_i}{\partial t} \mathrm{d}V_i + \int_{V_i} \nabla \cdot (\rho_i \mathbf{v}_i)\, \mathrm{d}V_i = 0. \tag{2.8}$$

Gauss' Theorem is stated as follows. Let V be a region in space with a boundary $\mathrm{d}\mathbf{S}$. Then the volume integral of the divergence $\nabla \cdot \mathbf{F}$ of $\mathbf{F}$ over V and the surface integral of F over the boundary $\mathrm{d}\mathbf{S}$ of V are related by

$$\int_V (\nabla \cdot \mathbf{F}) \mathrm{d}V = \int_S (\mathbf{F} \cdot \mathbf{n}) \mathrm{d}\mathbf{S}. \tag{2.9}$$

This means that the outward flux of a vector field through a closed surface is equal to the volume integral of the divergence over the region inside the surface. This can be applied to equation (2.8) to give

$$\frac{\partial}{\partial t} \int_{V_i} \rho_i \mathrm{d}V_i + \int_{S_i} \rho_i (\mathbf{v}_i \cdot \mathbf{n}) \mathrm{d}\mathbf{S}_i = 0 \tag{2.10}$$

where S_i is the control surface of the cell and $\mathbf{n}$ is the normal vector to the surface. If $\bar{\rho}_i$ is the cell's *volume average* density, i.e.

$$\bar{\rho}_i = \frac{1}{V_i} \int_{V_i} \rho_i \mathrm{d}V_i, \tag{2.11}$$

then equation (2.10) becomes

$$V_i \frac{\partial \bar{\rho}_i}{\partial t} + \int_{S_i} \rho_i (\mathbf{v}_i \cdot \mathbf{n}) \mathrm{d}\mathbf{S}_i = 0. \tag{2.12}$$

The term $\int_{S_i} \rho (\mathbf{v}_i \cdot \mathbf{n}) \mathrm{d}\mathbf{S}_i$ is the total mass flow rate over the surface of the cell. It is then possible to solve for the fluxes for each cell.

2.3 Molecular dynamics (MD)

Over the past 50 years, computational simulations of molecular systems have been performed [2] using numerical schemes to solve Newton's equations of motion. They have since been used to perform highly-detailed simulations of nano-scale systems, and has been successfully used in various different disciplines, such as: in biology to study the behaviour of protein folding [77]; in material science to study crystal formation [114] and in chemistry to study chemical reactions [132] among a wide

range of other applications.

Most modern codes are developed using the books by Allen and Tildesley [5] and Rapport [121]. In this section, the fundamentals of the simulation methodology are described including the equations which are solved, a numerical algorithm to solve these equations, how atoms interact with each other, and common tools which are used to control and measure within the simulations.

2.3.1 Equations of motion

In MD it is assumed that all atoms are point particles (i.e. all the mass of the atom is at an infinitesimally small point) and the intra- and inter-molecular forces can be averaged out and represented as functions of distance. The non-equilibrium motion of liquid molecules is implemented using Newton's equations of motion with added external forcing, $\mathbf{f}_{ext}$:

$$\frac{\mathrm{d}}{\mathrm{d}t}\mathbf{r}_i = \mathbf{v}_i, \tag{2.13}$$

$$m_k \frac{\mathrm{d}}{\mathrm{d}t}\mathbf{v}_i = \hat{\mathbf{f}}_i + \mathbf{f}_{ext} = \mathbf{f}_i, \tag{2.14}$$

where $\mathbf{f}_i$, $\mathbf{r}_i$ and m_i are the total force, position and mass, respectively, of an arbitrary molecule i of a system of N molecules, at a time t. The intermolecular force $\hat{\mathbf{f}}_i$ on each molecule is calculated

$$\hat{\mathbf{f}}_i = \sum_{j=1}^{N} -\nabla U(r_{ij}) \text{ for all } i \neq j, \tag{2.15}$$

where $U(r_{ij})$ is the potential energy when molecules i and j are separated by $r_{ij} = |\mathbf{r}_i - \mathbf{r}_j|$.

2.3.2 Numerical algorithm

To calculate the trajectory of all of the molecules the Velocity Verlet algorithm [150] (Algorithm 2) is used to numerically integrate the equations of motion in space and time, at each time-step t to the new time-step $t + \Delta t$, until $t = t_{end}$. This algorithm is 2nd-order accurate and constraints and controllers on the molecules can be easily included within the algorithm.

Algorithm 2 Velocity Verlet

while $t < t_{\text{end}}$ **do**
  for i to N **do**
    Update velocity by $\Delta t/2$:

$$\mathbf{v}_i\left(t + \Delta t/2\right) = \mathbf{v}_i(t) + \mathbf{a}_i(t)\Delta t/2 \tag{2.16}$$

    Advance time by Δt using $\mathbf{v}_i\left(t + \Delta t/2\right)$:

$$\mathbf{r}_i(t + \Delta t) = \mathbf{r}_i(t) + \mathbf{v}_i(t + \Delta t)\Delta t \tag{2.17}$$

    Compute force $\hat{\mathbf{f}}_i$ using equation (2.15).
    Calculate acceleration:

$$\mathbf{a}_i(t + \Delta t) = \mathbf{f}_i(t + \Delta t)/m_i \tag{2.18}$$

    Update velocity using new acceleration

$$\mathbf{v}_i(t + \Delta t) = \mathbf{v}_i(t + \Delta t/2) + \mathbf{a}_i(t + \Delta t)\Delta t/2 \tag{2.19}$$

  end for
  set $t = t + \Delta t$
end while

2.3.3 Potentials

There are many different potentials which have been developed to model the interactions between atoms. The simplest and computationally least expensive of these is the Lennard-Jones potential, but it is also the least realistic. These potentials are additions of functions which represent different forces occurring between atoms such as van der Waals forces and Paulis repulsion. As the potential only has a minor effect when molecules are separated by a large distance, a cut-off separation distance is introduced; when two molecules are separated by more than the separation distance the potential is set to zero, this reduces computational time with only a small affect on the results.

Lennard-Jones

In chapters 4 and 6 the Lennard-Jones (LJ) model of liquid argon is used, where the solid wall atoms are fixed/frozen [143]. We use a simple monatomic fluid with

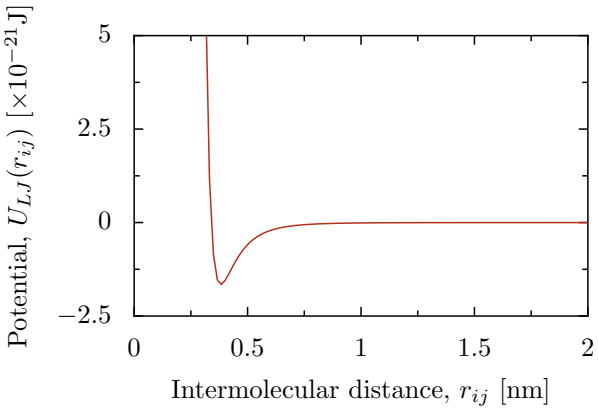

Figure 2.1: The Lennard-Jones 6-12 potential as described by equation (2.20).

the LJ 6-12 potential with a cut-off radius:

$$U_{LJ}\left(r_{ij}\right) = \begin{cases} 4\epsilon\left[\frac{\sigma^{12}}{r_{ij}^{12}} - \frac{\sigma^{6}}{r_{ij}^{6}}\right] & \text{if } r_{ij} \leq r_c, \\ 0 & \text{if } r_{ij} > r_c, \end{cases} \tag{2.20}$$

where σ and ϵ are the length in the system and energy characteristics of the potential, and r_c is the cut-off separation. The σ and ε properties for the liquid-liquid and wall-liquid interactions are taken from [143]: $\sigma_{l-l} = 3.4 \times 10^{-10}$ m, $\epsilon_{l-l} = 1.657 \times 10^{-21}$ J, $\sigma_{w-l} = 2.55 \times 10^{-10}$ m, $\epsilon_{w-l} = 0.33 \times 10^{-21}$ J and $r_c = 1.36$ nm. The solid mass density is $\rho_w = 6.809 \times 10^3\,\mathrm{kg/m^3}$, and the liquid mass density is $\rho_l = 1.431 \times 10^3\,\mathrm{kg/m^3}$, where the mass of one wall or liquid molecule is 6.6904×10^{-26} kg. The time-step in the MD simulations is 5.4 fs. Figure 2.1 shows a graphical representation of how this potential changes with distance from another molecule.

Water TIP4P/2005 model

Over the past 30 years over 40 different models have been developed for water [56]. None of these models are able to recreate all of the basic properties of water e.g. the viscosity and diffusion coefficient [48]. Some of the most commonly used water models are: SPC [12], SPC/E [10], TIP3P [64], TIP4P [65] and TIP5P [91].

In chapter 5 the rigid TIP4P/2005 water model [1, 61, 149] is used in modelling water through a carbon nanotube. The polar water model consists of four interacting sites: one oxygen atom (O) with no charge which is the centre of the Lennard-Jones potential, two hydrogen sites (H) each with a fixed point charge of $q_H = 0.5564\,e$, and a massless site (M) with charge $q_M = -1.1128\,e$; see Figure 2.2. All oxygen atoms interact using the Lennard-Jones potential, Eqn. (2.20) with

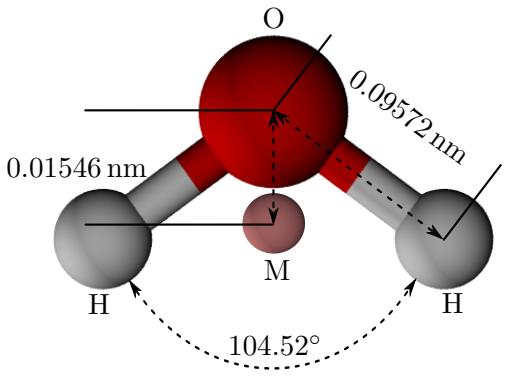

Figure 2.2: A graphical representation of the TIP4P/2005 water molecule.

$\varepsilon_{O-O} = 0.7749\,\mathrm{kJ\,mol^{-1}}$ and $\sigma_{O-O} = 3.1589 \times 10^{-10}\,\mathrm{m}$, while the other charged sites interact via the Coulomb potential:

$$U_C(r_{ij}) = \frac{1}{4\pi\varepsilon_0}\frac{q_i q_j}{r_{ij}}, \tag{2.21}$$

where q_i, q_j are the site charges and ε_0 is the vacuum permittivity. To reduce computational time, this potential is shifted to be zero at $r_c = 1.0\,\mathrm{nm}$:

$$U\left(r_{ij}\right) = \begin{cases} U_C(r_{ij}) - U_C(r_c) & \text{if } r_{ij} \leq r_c \\ 0 & \text{if } r_{ij} > r_c \end{cases}, \tag{2.22}$$

this means that the electrostatics of a molecule will not affect a molecule more than 1 nm away without introducing artefacts in the system by having a jump in potential. Not including these long-range interactions, whether using large cut-off radii or Ewald summations [69, 42], can have a significant effect on large macromolecular systems [53, 160]. But, in a recent paper, it has been found that including them does not guarantee accurate results [7]. The time-step for all MD water simulations is set to 2.16 fs. Figure 2.3 shows a graphical representation of how this potential changes with distance from another molecule.

More complex molecules

For small molecules, like water, the bonds can be modelled as rigid rods, rather than using an algorithm like SHAKE or RATTLE [127] to model the bonds vibrations, without losing much accuracy. This means that the time-step used can be relatively large as the fast vibrations do not need to be resolved. To model the intra-molecular structure of more complex molecules such as DNA and proteins, the bonds between

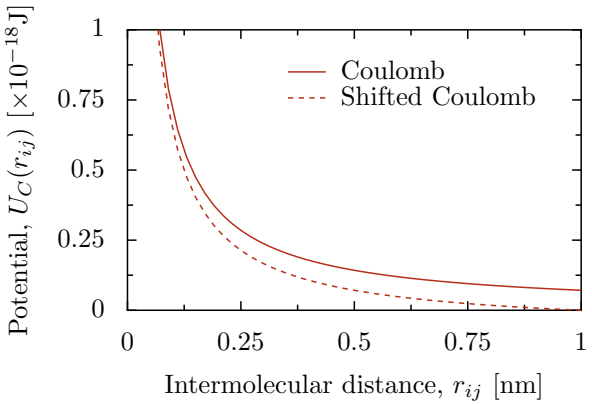

Figure 2.3: The Coulomb potential as described by equation (2.22).

atoms (or groups of atoms within the molecule) must be modelled. This is done using a potential energy equation similar to the inter-molecular bonds (equation (2.20) or (2.22)), but are generally about an order of magnitude stronger.

2.3.4 Model constraints

The thermodynamic behaviour of equilibrium molecular dynamics simulations is described with statistical mechanics. As each simulation is an isolated system they can be placed into different ensembles [45], which are known as:

- Microcanonical ensemble (constant-NVE), a constant-sized box and number of molecules with a prescribed total energy, this represents an adiabatic process;
- Canonical ensemble (constant-NVT), a constant-sized box is attached to a heat bath to keep the set number of molecules at a constant average temperature;
- Isothermal-isobaric ensemble (constant-NPT), keeps a constant amount of fluid as well as constant pressure and temperature.

By using these ensembles, average mechanical properties of the fluid can be represented.

For the measurements of the MD simulations to be useful as input to the CFD simulations, we require efficient and accurate controlling algorithms. There are different methods to constrain molecular dynamics simulations so as to be able to perform numerical experiments on the system. Many different algorithms have been developed to maintain and control these constraints. The algorithms of importance in this thesis are described here.

Density

It is very important to simulate the correct density of fluid otherwise the wrong pressure and viscosity measurements, for example, will be obtained. In this work, the recently developed FADE algorithm [22] is used to introduce and remove molecules from simulations. This approach is preferred to the popular USHER algorithm [32] because it allows molecules to be introduced quickly, without introducing artefacts to the simulation.

The difficulty in density control of a simulation is if a molecule is positioned too close to another molecule the repulsive potential between these two molecules will be large. This potential will cause each molecule to move away from each other at a very high speed, higher than the speed that the time-step is able to resolve accurately. This will trigger a chain reaction, leading to further molecular overlaps, resulting in a large amount of erroneous energy being introduced into the system. This is known as simulation blow-up.

In the FADE algorithm, molecules are introduced or removed over a relaxation period. When a molecule is being introduced (FADE-in), the strength of the intermolecular potential is slowly increased by multiplying it by a weighting factor, which increases from 0 to 1, over the relaxation period. Conversely, when a molecule is being removed (FADE-out), the weighting factor is decreased from 1 to 0 over the relaxation time. This ensures a smooth gain or loss of potential energy in the system.

Thermostat

In this work all of the cases are isothermal and we require an algorithm to keep the average temperature of the fluid constant. Common thermostats are the Berendsen [11], Nosé-Hoover [107] and the Andersen thermostat [6], each adopt different approaches to controlling temperature; such as velocity rescaling or having random collisions with molecules. The choice of thermostat is important as some can be computationally intensive, while others can introduce errors and artefacts into the system. In this thesis the Berendsen thermostat is used for all the MD simulations. This thermostat can introduce artificial effects [54, 13] into the system, but in a recent paper it has been shown to be physically accurate for the types of cases it is applied to in this thesis [141].

The Berendsen thermostat couples the molecules to a hypothetical heat bath, which is set to a target temperature. This is done by scaling the velocities perpen-

dicular to the streaming direction of the flow by the factor

$$\chi_Z = \left[1 + \frac{\Delta t}{\tau}\left(\frac{T_Z^{req}}{T_Z^{meas}} - 1\right)\right]^{1/2}, \tag{2.23}$$

where τ is a time constant that defines the coupling strength, T_Z^{req} is the required temperature and T_Z^{meas} is the measured temperature.

External force

In this thesis, we are performing Non-equilibrium molecular dynamics (NEMD) so we apply an external body force to the atoms to drive the fluid. In the simplest cases this may involve applying the same force to all molecules in the system $\mathbf{f}_{ext}$ or in a zone of the full domain to create a pressure difference. In other cases the intensity of the external force we apply is spatially varying, and has the form of a Gaussian distribution:

$$\mathbf{f}_{ext} = \bar{F} e^{(-x^2/2\sigma_s^2)}, \tag{2.24}$$

where $\bar{F}$ is the magnitude of the force and σ_s is the standard deviation of the distribution. This enables a smooth application of force and obtain smooth velocity and pressure profiles.

2.3.5 Measurements

To couple MD and CFD, macroscopic properties of the fluid need to be extracted. There are many different techniques that exist to measure the different properties of the fluid being simulated. The tools used in this work have been described in detail by Borg [18] and Nicholls [103].

2.4 Hybrid methods

As detailed in Chapter 1, CFD is not always an applicable tool for modelling systems on the nano-scale, which is why MD is commonly used. However, with current computational capabilities, MD is only capable of modelling geometries $O(100)\,\mathrm{nm}^3$ and for time scales of nano seconds. This is not a large enough geometry or long enough time for engineering applications.

A hybrid method is one that seeks to couple a continuum method (such as CFD) with a molecular or particle simulation (such as MD), such as to obtain the computational efficiency of the former with the accuracy of the latter. Hybrid methods were first developed to couple MD and finite-element method for use in

solid mechanics [73]. Some of the methodologies used are: the quasicontinuum method, the CLS method and the FEA method. Reviews of these methods have been written by Curtin and Miller [28] and Liu *et al.* [85]. However, the techniques that are used in solid mechanics are, generally, not applicable to fluids because in solid mechanics it is assumed that the molecules do not move significantly.

Hybrid methodologies for fluid flow were first introduced by O'Connell *et al.* [108] in an attempt to take some of the computational efficiency from CFD and combine it with the accurate, detailed data produced by MD. There have been a few different methodologies proposed to achieve this: Domain decomposition (DD) [108, 51, 157], Heterogeneous multiscale method (HMM) [35, 9, 159], equation-free method [72, 71] and the Internal-flow multiscale method (IMM) [20, 21, 115]. In the rest of this section the two most common types, DD and HMM, will be discussed.

2.4.1 Domain decomposition (DD)

In DD, the domain of the simulation is split up into areas where a molecular description is required to describe the fluid (such as at boundaries) and areas where continuum equations can safely be applied. The hybrid solution interface (HSI) is the interface between the two numerical methodologies. For the hybrid simulation to be valid it is important that the transport and thermodynamic properties are continuous across the HSI. There are two different types of coupling used in DD, coupling by state and coupling by fluxes, which will be discussed further in this section. A full review of DD has been written by Mohamed and Mohamed [99].

Coupling by state properties

The first DD methodology, proposed by O'Connell *et al.* [108], and subsequent refinements by Hadjicoustantinou [51] and Werder *et al.* [157], will be discussed in this section. These authors all coupled the continuum to the discrete via the state properties of the fluid in an overlap region to achieve the continuity required over the HSI. In this overlap region, any molecular layering caused by the finite size of the MD box, and forcing applied to the fluid to maintain a bulk pressure, are contained.

In the following the notation used is: Ω_C to denote the continuum region, Ω_D to denote discrete region, and Ω_O to represent the overlap region; as shown in Fig. 2.4.

To pass information from the discrete to the continuum ($\Omega_D \rightarrow \Omega_C$) is simply done by averaging the required properties of the fluid (e.g. velocity or temperature) around the HSI, which is applied as a boundary condition to the domain; see Fig.

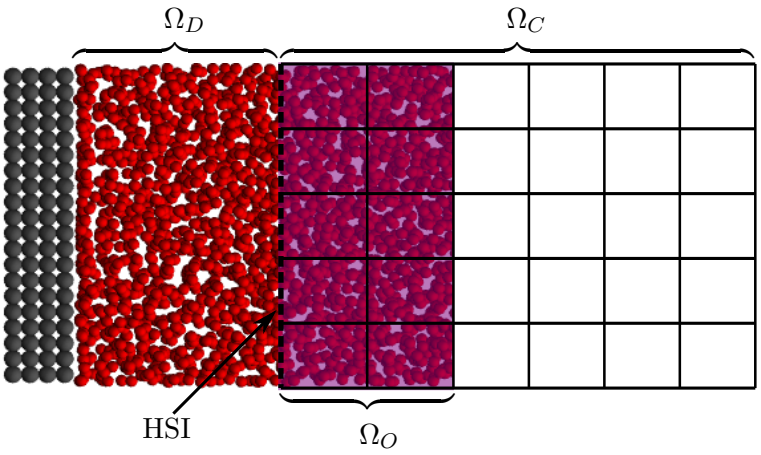

Figure 2.4: Schematic of a typical domain decomposition domain with coupling by state.

2.4. Passing information from the continuum to the discrete ($\Omega_C \rightarrow \Omega_D$) requires more finesse as the continuum will provide a single value for the coupled property, while the discrete has many more degrees of freedom.

O'Connell *et al.* suggested using a constraint procedure to relax the velocities of the molecules in the MD within the overlap region to the velocity provided by the continuum simulation, thereby creating momentum and stress continuity across the HSI. The method was compared to full MD simulations of Couette flow through a channel and good agreement was found.

The drawbacks of the methodology proposed were that there was no decoupling of time stepping schemes between the discrete and continuum, and it could not cope with mass fluxes across the HSI. Hadjicoustantinou and Patera [51] provided some modifications to overcome these limitations. Firstly, they introduced a Schwarz alternating method [84] to decouple the two timescales. They then added a 'reservoir' of particles surrounding Ω_O to handle mass fluxes over the HSI and drew velocities from the corresponding Maxwell distribution to control the MD molecules within the overlap region, as they found it to be more accurate.

Generally, in MD simulations, periodic boundary conditions are used, which creates an infinitely cyclic domain. However, in hybrid simulations this is often not desirable and, in certain problems, can necessitate simulating more molecules than are required, increasing computational cost [136]. In [108], a finite-sized box was used with a wall of molecules at one end and a body force applied to the molecules in Ω_O directed into the domain. This force is used to hold the molecules in the domain and maintain the correct pressure at the HSI. The magnitude of the force applied

was $\bar{F} = -\alpha p \rho^{-2/3}$, where p is pressure, α is a constant which controls the amount of structure induced and ρ is density. The use of this force introduces oscillations in the density and stress profiles that dictates the size of Ω_O. Werder *et al.* [157] found that by making the force applied depend on the RDF $g(r)$ [52] they could minimise these oscillations and therefore reduce the size of Ω_O, thus reducing computational cost.

Despite the application of this force some molecules may still be able to escape the domain. In [157], they suggest the use of a specular wall that reflects the molecules back by reversing the velocity of any molecules hitting the wall. This maintains the overall number of molecules in the molecular subdomain and can be thought of as a plane of symmetry.

Another major issue in hybrid methods is the amount of statistical noise in the data produced in the MD simulations by thermal fluctuations. This means that the exact value of fluid properties cannot be found in a finite amount of sampling time. Hadjiconstantinou *et al.* [50] derived estimates for the number of independent samples required for measured properties to have a chosen amount of uncertainty (variance). These estimates depend on properties of the fluids acoustic number and Mach number (i.e. speed).

Probabilistic methods have also been proposed to predict the most-likely value of the measured variables. Two possibilities that have been proposed are: the maximum likelihood inference method by Li *et al.* [79, 80, 81] and Bayesian inference by Salloum *et al.* [129].

In contrast to these methods, in a chapter of Reduced Order Methods for Modeling and Computational Reduction, Grinberg *et al.* [47] began work on the use of window proper orthogonal decomposition (WPOD) to perform data analysis on the MD data, by removing the thermal noise, for input into hybrid simulations. This technique is quite common and well developed for the analysis of turbulent data in continuum simulations and many other scientific fields.

Coupling by fluxes

Coupling by fluxes of variables was introduced by Flekkøy *et al.* [41]. The computational domain is split up in a similar way as with coupling via state properties, but the Ω_O region is divided up into 3 *cells*; see Fig. 2.5. In the region $\Omega_C \rightarrow \Omega_D$ the fluxes calculated in the continuum are passed to the discrete domain, and the reverse happens in $\Omega_D \rightarrow \Omega_C$. By coupling via fluxes, this method automatically abides by conservation laws and can be used to naturally couple to a finite-volume CFD simulation, see section 2.2.3. Flekkøy *et al.* only coupled mass and momentum

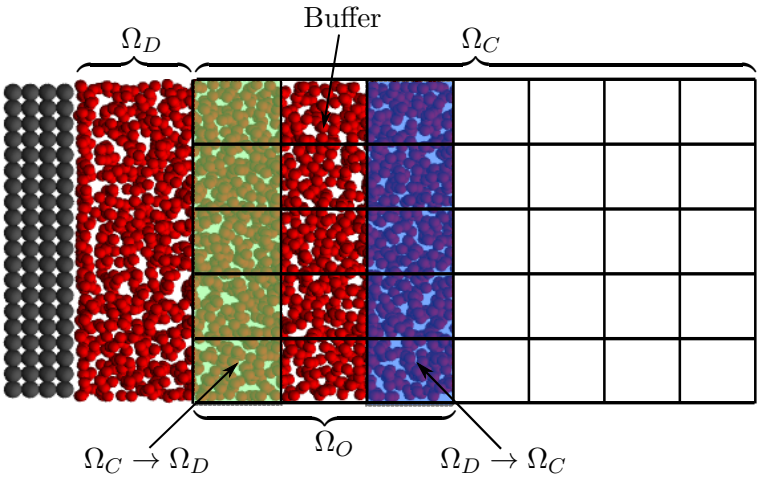

Figure 2.5: Schematic of a typical domain decomposition domain with coupling by flux.

but the method was extended to couple energy by Delgado-Buscalioni and Coveney [31].

Different methods of imposing the $\Omega_C \rightarrow \Omega_D$ flux were discussed by Kalweit and Drikakis in [68]. Both Flekkøy *et al.* and Delgado-Buscalioni and Coveney used an external force to transfer momentum fluxes for $\Omega_C \rightarrow \Omega_D$ coupling. However, Kalweit and Drikakis found that such a force was shown to induce a relaxation zone in the buffer region with a width that increases linearly with the number of atoms in that zone subjected to the force. It was demonstrated that confining atoms via the momentum flux force, to limit the width of the relaxation zone, results in a drop in energy due to the reduction of the external potential energy of the atoms as they are moved closer to the HSI. Therefore, Kalweit and Drikakis proposed a velocity reversing scheme that separates the transfer of momentum and energy. Momentum is transferred by reversing the velocities of enough molecules to induce the correct momentum flux and energy is transferred by scaling velocities. This scheme was found to be more stable and reduce fluctuations in the system properties.

Both De Fabritiis *et al.* [30] and Delgado-Buscalioni *et al.* [33] demonstrated the importance of including extra terms in the continuum equations to account for the statistical fluctuations. If these fluctuations are not included then the position of the HSI in the continuum domain becomes visible in the results.

Despite their demonstrated success in a number of applications, DD methods have some disadvantages in certain classes of flow [49]. The main disadvantages of DD are that the time-stepping is restricted by the molecular solver and that in long

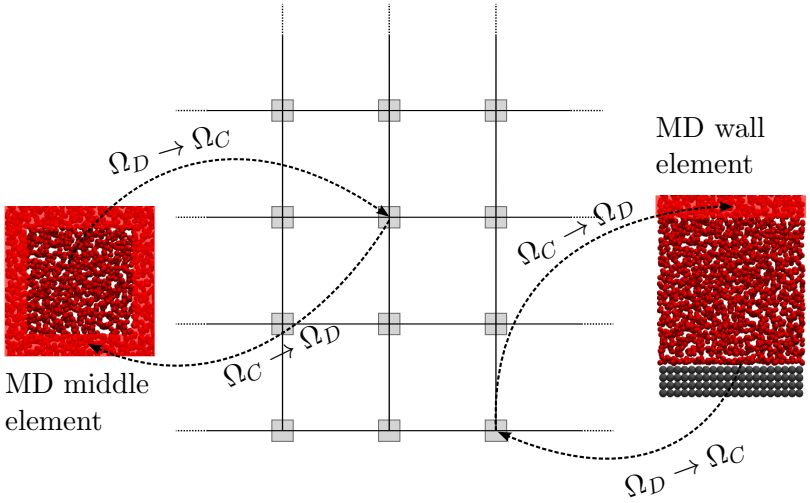

Figure 2.6: A schematic representation of a HMM simulation.

confined channels the molecular solver is required along the whole boundary in order to capture the slip and other near-wall phenomena. This, therefore, restricts the length of channel it can be applied to.

2.4.2 Heterogeneous multiscale method (HMM)

In the HMM, continuum equations are solved over the whole domain, but at each time-step, properties of the fluid (such as viscosity or shear stress) and boundary information (such as slip velocity) are updated using molecular simulations. This removes the need for knowledge of constitutive relationships of the fluid or for phenomenological slip boundary conditions [124] *a priori*. Similar techniques have been proposed by E *et al.* [35], Asproulis *et al.* [9] and Yasuda and Yamamoto [159].

HMM can be utilised in cases where the continuum equations are nearly valid but require some correction from molecular resolution simulations. For instance, if the boundary condition at a wall is unknown or if a constitutive relationship is required, such as the stress tensor field. This is done by performing an MD simulation at each computational node of the continuum simulation to obtain the desired property. A representation of this is shown in Fig. 2.6. The motion of the fluid in the subdomains is controlled in the shaded regions using data from the continuum simulation.

In Fig. 2.6, the black lines represent the continuum grid and the intersections are the computational nodes. In both [35] and [159], for every computational node an atomistic simulation is performed to obtain the data for that point in space. However, a lot of the simulations in the MD subdomains will be under similar

conditions. This means that many of the simulations may not be necessary as data already produced can be reused. Asproulis *et al.* [9] used a neural network algorithm to optimise the number of simulations being performed and reduce redundancy, thereby minimising computational cost.

For highly-confined channels, in which the molecular scale is comparable to the transverse scale, the molecular subdomains will be forced to overlap. This is due to the minimum size required to capture fluid properties and the resolution of the continuum grid needed to obtain an accurate velocity profile. This is inefficient and less accurate than using a molecular solver over the whole domain. Therefore, Borg *et al.* [19] have proposed a field-wise coupling approach by decoupling the molecular subdomains from the computational nodes of the continuum domain. Instead, they spatially distribute the subdomains and data is interpolated to the computational nodes of the continuum domain. However, to guarantee accurate results a dependency study on the number and spacing of the subdomains must be performed.

Alternately, Alexiadis *et al.* [4] have developed an HMM technique in which they evaluated the Laplacian (2nd derivative) of the constitutive properties that are being coupled. By doing this they were able to use fewer atomistic subdomains than with standard HMM. However, it was more susceptible to noise and uncertainty from the MD data.

Time-stepping schemes

In this discussion, we use the naming scheme defined by Lockerby *et al.* [86] because they give a clear description of the time-stepping, decoupled from the (spatio-temporal) hybrid scheme as a whole. We will refer to the time-step of the continuum as Δt_{CFD} and the MD as Δt_{MD}. A representation of all the schemes can be found in Fig. 2.7.

As mentioned earlier, O'Connell *et al.* [108] used a *fully-coupled* scheme in which $\Delta t_{\mathrm{CFD}} = \Delta t_{\mathrm{MD}}$ and performed the coupling of state properties at each time-step. This means that the time evolution of the system is constrained by the smallest required time-step from the two methods, and does not take advantage of any scale separation.

Rather than coupling at every time-step, the continuum model can be given a larger time-step such that $\Delta t_{\mathrm{CFD}} = N\Delta t_{\mathrm{MD}}$, where N is a set number of time-steps, see Fig. 2.7(b). This reduces computational cost by reducing the number of continuum time-steps used and any overhead in performing the coupling, this has been used by Nie *et al.* [106]. This can be referred to as the Continuous micro

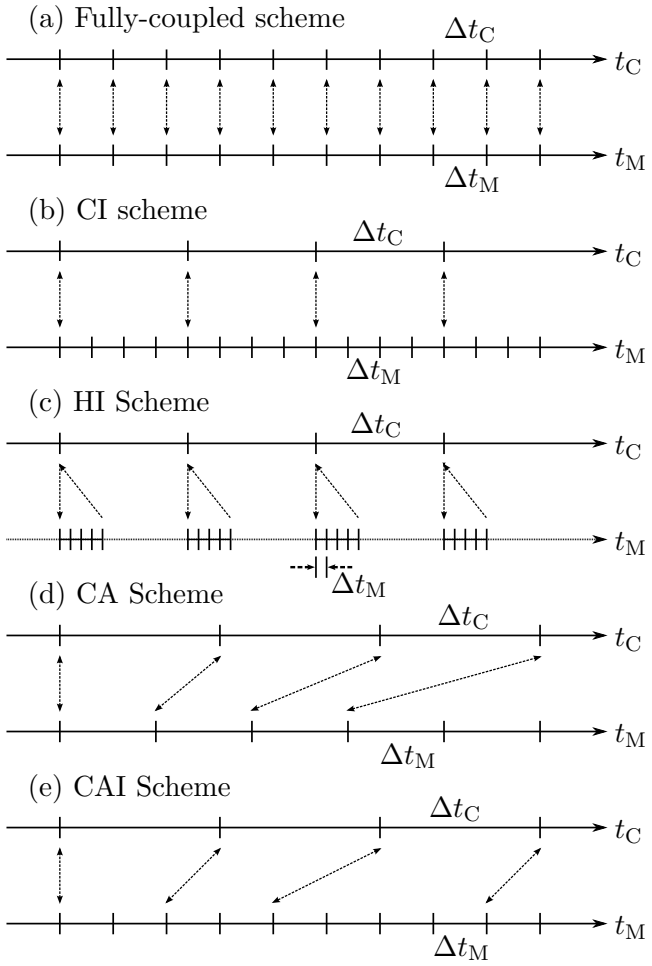

Figure 2.7: Representations of the different possible time schemes: (a) fully-coupled scheme, (b) CI scheme, (c) HI scheme, (d) CA scheme, and (e) CAI scheme.

solution — Intermittent coupling, or CI.

In the HMM as proposed by E *et al.* [35], enough MD time-steps are performed for each continuum time-step such that the MD simulation has *quasi*-steadily equilibrated. Therefore, all of the MD time-steps after the coupled property has been measured accurately can be skipped, thus reducing computational time, see Fig. 2.7(c). This means that for every Δt_{CFD} there are $N\Delta t_{\mathrm{MD}}$ preformed, but unlike in the CI scheme $\Delta t_{\mathrm{CFD}} \neq N\Delta t_{\mathrm{MD}}$. However, this time-scheme is only valid when the continuum is quasi-steady, as demonstrated in [86]. This is because all of the fine-scale data from the MD is lost, which is acceptable if all that is required is the macro-scale information. This method is named Heterogeneous micro solution — intermittent coupling, or HI, see Fig. 2.7(c).

In [36], some improvements to the HMM were suggested to create a *seamless* HMM. One of the improvements was to propose an asynchronous time coupling, denoted here as Continuous micro solution — asynchronous coupling, or CA scheme. In this scheme time-scale separation is exploited by performing the MD and continuum model with different time-steps, such that $\Delta t_{\mathrm{CFD}} = g\Delta t_{\mathrm{MD}}$, where g is a constant known as the *gearing*. The coupling is performed at each time-step, see Fig. 2.7(d).

Lockerby *et al.* [86, 87] have proposed a general version of these time-stepping schemes in what they call Continuous micro solution — asynchronous intermittent coupling, or CAI scheme. As the name suggests, they continuously perform the MD simulation (as in the CI and CA schemes), coupling intermittently (as in the HI and CI schemes) asynchronously (as in the CA scheme) and means that $\Delta t_{\mathrm{CFD}} = gN\Delta t_{\mathrm{MD}}$. By doing this it is possible to achieve full control over the time-scale separation that is taken advantage of, thus, can perform multiscale simulations as efficiently as possible for a given accuracy.

2.5 'Sequential' hybrid schemes

So far all of the hybrid methods discussed can be categorised as 'concurrent' hybrid schemes. This means that the atomistic and continuum simulations are performed at the same time and data is passed from one to the other as needed. An alternative to these are 'sequential' hybrid schemes. This means that the atomistic simulations are performed before the continuum simulations. These simulations gather data over the expected parameter space of the domain and build constitutive relations from this data.

Sequential methodologies have been well developed in solid mechanics where

they are known as hierarchical multiscale modelling. In these methods they couple between different hierarchies of length scale from quantum mechanics through molecular dynamics all the way up to continuum mechanics. They are used to design new lightweight, strong materials, such as magnesium alloys [98] and polymers [139], and have been useful in the development of automotive components [58]. Several reviews of the techniques used exist [24, 74, 139].

Near to a solid bounding surface in rarefied gas dynamics there exists what is known as a Knudsen Layer, in which there is significant departure from the standard Navier-Stokes equations. For this reason, wall-distance scaling functions have been proposed that take data from Kinetic theory and input it into the continuum simulations to alter constitutive relations for stress/strain rate close to the wall [69]. In addition, Lockerby *et al.* [88] measured coefficients for a slip model from a kinetic model, BGK Boltzman equation, to be input into continuum simulations.

Joseph and Aluru [66] performed sequential multiscale simulation to model the water and ion transport in silica nanochannels. They measured quantum effects to create a molecular electrostatic potential, using density functional theory, which can be used in MD simulations. Transport coefficients, such as mobilities and diffusion coefficients, are computed from MD simulations to be input into continuum simulations. This meant that they were able to accurately study channels with micrometer lengths but nanometer widths.

The decision as to whether a concurrent or sequential scheme will be more effective (or efficient) for modelling a problem comes down to the size of the parameter space that boundary conditions, and other fluid properties, are required for. For complex problems (where the information you need to extract from MD depends on many parameters) it is more efficient to run concurrently, than sequentially. But for some problems (where look-up tables and interpolants can be constructed) the sequential approach is more efficient.

2.6 Summary

In this chapter, some of the modelling techniques that have been used for simulating dense liquids have been described. In section 2.2, the basics of CFD are described, this is now widely used in engineering design but is not always applicable at the nano-scale due to the breakdown of the continnum assumption. Section 2.3 describes the fundementals of MD. MD is able to accurately model nano-scale fluids but is too computationally expensive to model domains on a scale relevant to engineering applications. A review of hybrid discrete-continuum methods is presented

in section 2.4, these try to take the highly-detailed results of MD and couple with computationally efficient MD. Despite much success in using them, hybrid schemes are still far too computationally expensive to perform in an engineering design process. In the rest of this thesis a 'sequential' hybrid MD-CFD model is developed which uses MD to provide constitutive relationships and boundary conditions for the CFD.

Chapter 3

Sequential hybrid methodology

3.1 Introduction

In this chapter the development of a sequential hybrid methodology is described. The methodology we are proposing involves performing molecular dynamics simulations (MD) to gather fluid properties and fluid-solid interface properties. This data is turned into a form that can be input into computational fluid dynamics (CFD) simulations. This is done so that nano-scale fluids can be modelled more efficiently and accurately than can be done by either one of these methodologies alone.

We will discuss different possible methodologies before presenting a thorough description of the MD pre-simulations that we will perform to gather the data for the transport properties and boundary conditions that are required for the CFD simulations.

3.2 Possible methodologies

There have been many different methods/algorithms developed for measuring different fluid properties in MD. For our simulations we want to measure all of the required fluid properties as efficiently as possible. This means performing as few simulations, for as little time as possible, while maintaining physical accuracy. The first major decision we must make to design an efficient methodology is whether to measure the properties using Equilibrium molecular dynamics (EMD) or non-equilibrium molecular dynamics (NEMD).

One possible methodology would be to measure all of the properties using Green-Kubo relations [75] within EMD simulations. These relations use the spontaneous molecular fluctuations that occur within a fluid in equilibrium. These fluctua-

Property	Definition	Green-Kubo formula
Diffusion Coefficient (D) ($J = v$)	$\dot{n} = -D\frac{\partial n}{\partial x}$	$\frac{1}{3}\int_0^\infty \langle v_i(t) \cdot v_i(0)\rangle dt$
Shear Viscosity (μ) ($J = P_{xy}$)	$\tau_{xy} = \mu\frac{\partial u_x}{\partial y}$	$\frac{V}{k_B T}\int_0^\infty \langle P_{xy}(t)P_{xy}(0)\rangle dt$
Thermal Conductivity (κ) ($J = q_x$)	$q_x = -\kappa\frac{\partial T}{\partial x}$	$\frac{V}{k_B T^2}\int_0^\infty \langle q_x(t)q_x(0)\rangle dt$

Table 3.1: Auto correlation function of current due to particle flux, shear stress tensor, and heat flux vector give corresponding transport coefficients. Where k_B is the Boltzmann constant.

tions decay and follow the same linearised equations as those for small macroscopic deviations of the mean value from equilibrium. This is Onsager's assumption of the regression of fluctuations [109] and is the basis of one form of the fluctuation-dissipation theorem [75] relating equilibrium fluctuations to transport coefficients like viscosity, thermal conductivity, and diffusion in a non-equilibrium system that is perturbed slightly from its equilibrium state. Linear response theory states that the linear response of these macroscopic properties can be expressed in terms of the fluctuation properties of the system in equilibrium. The Green-Kubo relations are formulated in terms of correlation functions of the equilibrium fluctuations of the corresponding thermodynamic property J, i.e.

$$\Psi_{J,J(t)} = \langle J(0)J(t)\rangle, \tag{3.1}$$

where the angular brackets denote the average over the canonical ensemble of the system. Various transport coefficient are given in Table 3.1. These relations can be used to calculate the slip length for a slip boundary condition, as was first developed by Bocquet and Barrat [15]. This is done by measuring the viscosity, as above, and then measuring the forces between the fluid and the wall. The slip length is then

$$\xi = \frac{\mu}{C_f}, \tag{3.2}$$

where ξ is the slip length and C_f is a friction coefficient between the wall and the fluid via the force exerted by the liquid on the solid:

$$C_f = \frac{S}{k_B T}\int_0^\infty \mathrm{d}t\langle f_x(t)f_x(0)\rangle, \tag{3.3}$$

where S is the surface area and $f_x(t)$ is the tangential stress exerted by the fluid on the solid at time t.

An advantage of this methodology is that it can be performed on a fairly small computational box, meaning that the simulations are less computationally expensive. However, this comes at the cost of a poor signal-to-noise ratio; it can therefore require a long averaging time to guarantee an accurate measurement. As the Green-Kubo relations are based on linear response theory they are only capable of capturing the linear behaviour of properties at equilibrium [138]. If the system is taken far from equilibrium and fluid properties behave non-linearly, such as slip length at high shear rates or the viscosity of a non-Newtonian fluid, then the Green-Kubo relations will not be able to accurately resolve properties.

The alternative is to use NEMD simulations. By applying a constant known force to a fluid with a chosen density, to develop a velocity profile, fluid properties and relations in these conditions can be measured. The signal-to-noise ratio in NEMD simulations depends on the departure from the equilibrium, the further the departure from equilibrium the higher the signal-to-noise ratio. NEMD simulations are also capable of obtaining the non-linear behaviour of fluids that occur and, therefore, are capable of measuring properties with more physical accuracy than with EMD. For these reasons we have chosen to use the NEMD methodology that is described in the rest of this chapter.

3.3 MD pre-simulations

For the isothermal CFD simulations of nano flows we consider in this thesis, we require the following fluid properties and boundary conditions: the viscosity coefficient as a function of density, the pressure as a function of density, the slip length as a function of density and shear rate, and what we here define as the 'surface displacement' (δ) which defines the position of the surface, as modelled by the CFD, relative to some atomistic reference point (in this thesis, the atomic centres). For efficiency and convenience we propose a single MD configuration from which all of these fluid properties can be measured and/or controlled. This enables efficient concurrent MD simulations over any range of variables considered by multiple realisations of the same MD geometry/setup.

Figure 3.1 (far left) shows the MD pre-simulation domain; it is symmetrical about its centrelines and uses periodic boundary conditions in the streamwise direction (i.e. in the x-direction) and into the page (i.e. in the z-direction). The domain has *bulk*, *shear* and *interface* zones (as labelled) for measuring state, constitutive

and boundary properties, respectively. Pressure and density (and also temperature, if simulating non-isothermal cases) are measured in the bulk zone. In addition to this, in the bulk zone an artificial streamwise body force ($\bar{F}$) is applied (see Figure 3.1, centre left), which creates a velocity profile in the domain similar to that illustrated (centre right). We assume that the equation of state in the bulk zone is unaffected by the magnitude of strain rate generated. In the shear zone the fluid is subject to a constant shear stress, τ_{xy}, directly resulting from the bulk-zone forcing. A linear flow velocity profile is developed in the shear zone, and this is least-squares fitted to obtain properties of the fluid, as described below.

Across multiple simulations, we obtain the bulk pressure, a viscosity coefficient, the slip length, and the surface displacement, for a range of combinations of bulk density and applied shear stress. In the MD simulations the applied shear stress and bulk density are varied by modifying the body force and by adding / removing molecules, respectively, using the FADE algorithm [22]. Finally, once all data is collected over the expected range of density and shear stress[1], functional relationships are constructed for the desired fluid properties (using, for example, fitted polynomials) which are then used in the CFD model. The behaviour of this CFD model ultimately depends on these functional relationships, and this choice requires some experience or needs to form part of an iterative approach . For the cases considered in this thesis, we adopt the following: for pressure, $p = p(\rho)$; for dynamic viscosity, $\mu = \mu(\rho)$; surface displacement, $\delta = \delta(\rho)$; and slip length $\xi = \xi(\rho, \dot{\gamma})$, where ρ is the bulk fluid density and $\dot{\gamma}$ is the strain rate in the shear zone. This dependence on density would normally imply a high-speed high-Mach number flow, but in nano-scale internal flows it is possible to have substantial fluid compressibility at extremely low Mach numbers due to viscous-related pressure losses (see [43] for a discussion of this). For this reason, capturing the influence of density on fluid properties is critical to the accurate prediction of nano-scale flows. For all of the examples considered, the influence of strain rate can be safely ignored, but we consider its effect on slip length for demonstration purposes. The fluids we consider are therefore Newtonian in the bulk; a non-Newtonian fluid, for example, would at least require $\mu = \mu(\rho, \dot{\gamma})$. Note that for the simulation of well-understood fluids it would not be necessary to extract all of these properties from MD pre-simulations.

[1] in most cases, the expected ranges can be comfortably over predicted — in less familiar simulations an iterative or trial-and-error approach might need to be adopted.

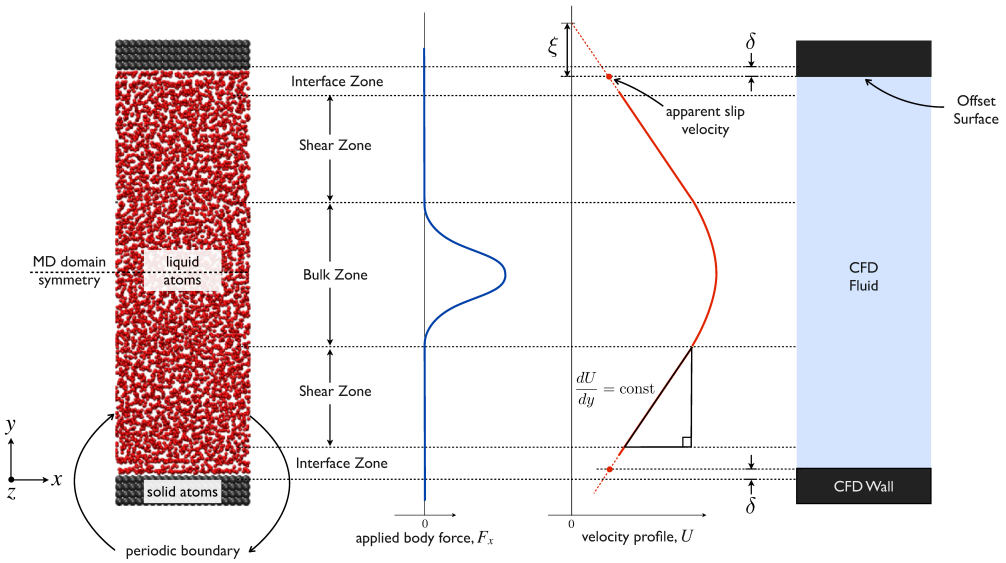

Figure 3.1: Schematic of Molecular Dynamics pre-simulation for extracting fluid dynamic properties that are essential inputs to an enhanced CFD solver for nano-scale flows.

3.3.1 Slip boundary conditions

In fluid dynamics, the commonly used boundary condition for when a fluid meets a wall is the no-slip boundary condition, which means that the velocity of the fluid is the same as the velocity of the wall. When modelling nano-scale liquids (and rarefied gases), it has been found that this standard boundary condition is no longer valid. For liquids, velocity at surfaces can, instead, be defined using the Navier slip condition:

$$u_{slip} = \xi \dot{\gamma} \tag{3.4}$$

where ξ is the slip length and $\dot{\gamma}$ is the shear-rate at the bounding surface. The slip length is defined as being the distance from the wall to the point where the velocity of the fluid becomes zero, see Fig. 3.1. There have been many studies on how the slip length depends on different properties of fluid and wall, for full review see Ref. [16]. These properties include the ratio of wall-liquid density [142], the mass and stiffness of the wall molecules [8], strain rate [143, 94, 119], wettability of the wall [60] and wall-fluid interactions [118].

In this work, we only investigate steady isothermal liquid flows, therefore our slip boundary condition only needs to depend on the strain-rate (as in [143]) and the density [17]. In fact, the strain-rate dependence is not necessary for the example cases we consider due to the relatively low shear-rates, but here it is included for the

purposes of illustration. Based on the strain-rate/slip-length relationship proposed in [143], and assuming a linear dependence on density, a least-squares fit is performed to the following equation:

$$\xi = \frac{(c_1\rho + c_2)}{\sqrt{1 - \dot{\gamma}/\dot{\gamma}_c}}, \tag{3.5}$$

where ρ is the density, $\dot{\gamma}_c$ is the critical shear rate (see [143]), and c_1, c_2 and $\dot{\gamma}$ are parameters of the fit to our MD pre-simulations.

3.3.2 Constitutive relationships

To accurately model nano-scale flows our CFD simulations will require equations to describe the transport properties. The relationships we require are the viscosity coefficient as a function of density and the pressure as a function of density.

As discussed in §2.2.1, at the nano-scale there is significant compressibility even within dense liquids due to the high pressure drops required to overcome high viscous forces [43]. These pressure changes are large relative to absolute pressure, and thus we are using a weakly compressible Navier-Stokes solver. This means that we require an equation of state that relates the pressure and density. We measure the pressure using the Irving-Kirkwood equations [62] for the different densities that are simulated for the measurement of slip length.

Due to this compressibility and the high pressure differences used in this work to compare to full MD simulations, the viscosity of the liquid varies significantly. Different methodologies have been developed to measure the viscosity of fluids in MD simulations, such as using Green-Kubo relations in EMD simulations or by using one of the variants of the NEMD SSLOD algorithm [39, 148, 37]. As we have already chosen to perform a set of NEMD simulations to obtain the slip length we choose to calculate the viscosity from the same simulations to reduce computational costs. The methodology we use is to extract the strain-rate from the MD shear zone by a least-squares linear fit to the relaxed and time-averaged velocity profile. The applied shear stress is measured using the Irving-Kirkwood equation [62]. The measured strain rate and shear stress are then used to obtain a viscosity coefficient, μ, through

$$\tau_{xy} = -\mu \frac{\mathrm{d}U}{\mathrm{d}y}. \tag{3.6}$$

We assume that shear viscosity is sufficient to describe the fluid constitutive behaviour, while accepting that the pre-simulation configuration would need to be modified to deal with the extensional viscosities found in non-Newtonian fluids. A possible way to do this would be to use NEMD SSLOD, which has been shown to

be able to capture extensional viscosity [29]. Note, due to the breakdown of the continuum assumption and the existence of non-local stress, this state-dependent viscosity becomes only approximate when applied to a nano-confined fluid.

3.3.3 Surface displacement

Between the surface atoms of the solid and the liquid is a thin depletion layer where molecules rarely exist [131], as shown in Fig. 3.2. In some works it is thought that the lower viscosity of this layer compared to the bulk fluid is the cause of the slip length and a linear relationship exists between slip length and depletion layer [152]. This has been shown to be false, but it does depend on the fluid-wall interactions [131].

We define the surface displacement to be the distance δ that the location of the CFD boundaries relative to the atomic (actual) walls has to be altered due to the depletion layer, see Fig. 3.2. In Figure 3.2, the solid lines across both images indicate where the atomic centers of the wall in the MD simulation are located. The dotted lines represent where the CFD surface would be placed to simulate this domain. In previous work the surface offset has been set to the liquid-solid interaction length [67] or chosen in another arbitrary way, and in some cases neglected altogether. We take this displacement to be the distance from the centre of the surface wall atoms to where the fluid density becomes at least 10 % of the bulk, i.e. $\rho \geq a\rho_{bulk}$, where $a = 0.1$. Note, the surface displacement is quite insensitive to the percentage of the bulk density chosen as the threshold, since the density increases from zero to well above the bulk density over a very short distance. For example, had we chosen the threshold to be at 20 % of the bulk density, the surface displacement would have only been 1–2 % larger, for a typical case.

If δ varies substantially with density (or any other fluid property), the geometry of the enhanced CFD domain becomes dependent on the CFD solution itself, this would cause re-meshing issues. In certain cases the value of δ will itself be dependent on the geometry, particularly for high curvatures, such as around sharp corners and obstructions. It is beyond the scope of the current work to attempt to accommodate these influences, while noting that, later, we obtain good agreement with full MD simulations without doing so. To tackle geometry-dependent flow properties (including surface displacement) would dramatically increase the parameter space that the pre-simulations would be required to supply information for; in fact, for such problems a 'concurrent' hybrid approach is likely to be more efficient.

As the spatial-scale of the geometry increases, the relative significance of the surface displacement reduces. We can develop a simple gauge of its impact by

considering the percentage that it modifies the mass flow rate in a simple channel in two limiting cases: assuming no-slip at the walls (i.e. $\xi = 0$); and for very high slip (i.e. $\xi \gg h$, where h is the channel width). In the no-slip case, for Poiseuille flow, the mass flow rate is proportional to the cube of the channel width; the percentage difference of using the surface displacement is then

$$\epsilon = \left(1 - \frac{(h - 2\delta)^3}{h^3}\right) \times 100\,\%. \tag{3.7}$$

For high-slip cases, where the velocity profile becomes plug-like, the mass flow rate becomes proportional to the square of the channel width, giving a percentage difference:

$$\epsilon = \left(1 - \frac{(h - 2\delta)^2}{h^2}\right) \times 100\,\%. \tag{3.8}$$

Based on the estimates of equations (3.7) and (3.8), the impact of a surface displacement δ~0.2 nm will be less than 1% for channels larger than 75–100 nm. In the no-slip case, for Hagen-Poiseuille flow, the mass flow rate is proportional to the 4th power of the channel radius; the percentage difference of using the surface displacement is then

$$\epsilon = \left(1 - \frac{(r - \delta)^4}{r^4}\right) \times 100\,\%. \tag{3.9}$$

For high-slip cases, where the velocity profile becomes plug-like, the mass flow rate becomes proportional to the square of the channel radius, giving a percentage difference:

$$\epsilon = \left(1 - \frac{(r - \delta)^2}{r^2}\right) \times 100\,\%. \tag{3.10}$$

Based on the estimates of equations (3.9) and (3.10), the impact of a surface displacement δ~0.2 nm will be less than 1 % for channels with radius larger than 100 nm.

3.4 Summary

We have presented a sequential hybrid MD-CFD methodology, and the MD pre-simulation framework that is used to obtain the data required by the CFD. EMD simulations, although more efficient, are not accurate for obtaining properties in conditions that are significantly departed from equilibrium (e.g. for high strain rates). As such, for generality, we have employed NEMD simulations to obtain properties within a single framework of simulations. This framework could be extended with relative ease to include temperature dependence or to model complex polymer fluids, which would require measuring extensional viscosity.

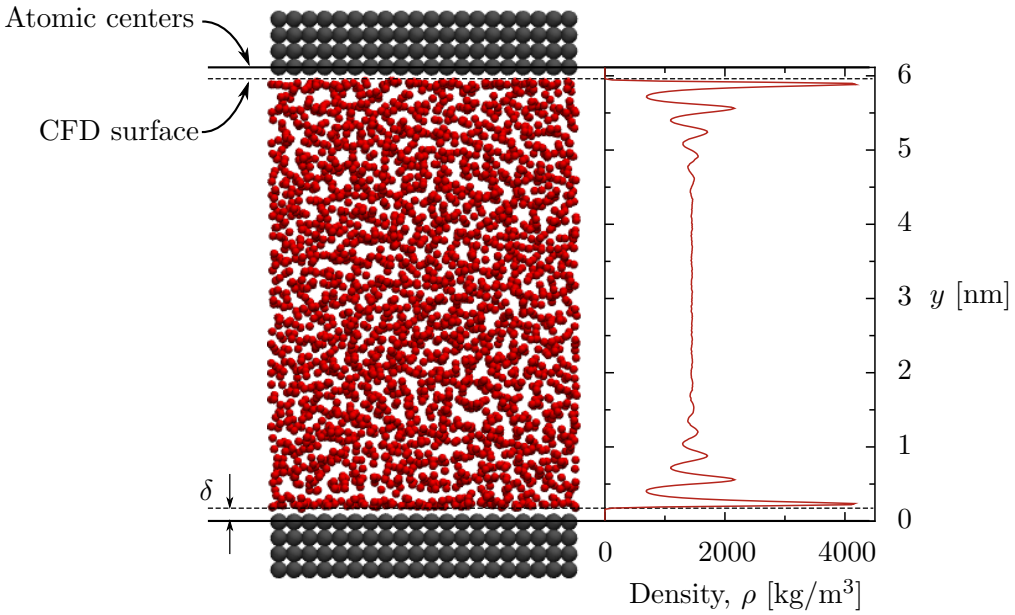

Figure 3.2: A representation of the depletion layer and the surface offset. Left: an image of an MD simulation through a 6 nm channel. Right: the density profile of this simulation.

Chapter 4

Steady and unsteady simulations of Lennard-Jones fluids

4.1 Introduction

In this chapter we demonstrate that computational fluid dynamics (CFD) simulations can still play a major role in nano flow prediction for engineering design or, alternatively, for the initiation of steady-state molecular dynamics (MD) simulations. We show that useful predictions can be readily and reliably obtained in non-trivial nano-scale geometrical domains, up to the limits of the continuum-fluid assumption, if appropriate fluid state models, viscosity relationships, and slip models are provided.

Owing to the lack of detailed and reliable experimental flow measurements at the nano-scale, in this section we compare our enhanced CFD predictions with full-scale MD simulation results. This comparison is intended to test whether flow field solutions of comparable accuracy to full MD can be obtained from our enhanced CFD in complex nano-scale geometries, without the need for *ad hoc* corrections, and at only a fraction of the cost of full MD. A Lennard-Jones (LJ) model of liquid argon is chosen, where the solid wall atoms are fixed/frozen [143]; the exact interatomic potentials used are given in §2.3.3.

In this chapter, we describe the results obtained by performing the pre-simulation methodology set out in Chapter 3 for a Lennard-Jones fluid. The model for the Lennard-Jones fluid is then used in our CFD model for steady simulations (Section 4.3) and unsteady simulations (Section 4.4).

4.2 Pre-simulation results for a Lennard-Jones fluid

Figure 4.1 (a) shows MD pre-simulation measurements of pressure, obtained from the standard Irving-Kirkwood expression [62], varying with the mass density. The MD pre-simulation results are least-squares-fitted to a 2nd order polynomial. This then serves as an equation of state within the enhanced CFD solver to connect the mass continuity equation to the momentum equation. In this case the polynomial is $p = 0.001559\rho^2 - 3.387\rho + 2020.6$. For reference, data from the NIST database for argon [83] is also plotted in Figure 4.1 (a), and is in close agreement with our MD pre-simulation data.

The strain-rate is extracted from the MD shear zone by a least-squares linear fit to the relaxed and time-averaged velocity profile. The applied shear stress is measured using the Irving-Kirkwood equation, from which we obtain a dynamic shear viscosity coefficient for LJ argon at a given bulk density. The viscosity coefficients measured from our MD pre-simulations of Lennard-Jones argon are shown in Figure 4.1 (b). A least-squares polynomial fit of 2nd order in density is also plotted: $\mu = 7.96 \times 10^{-10}\rho^2 - 1.774 \times 10^{-6}\rho + 0.001106$. This is then used in our enhanced CFD simulations to close the momentum equation.

The surface displacement δ defines the location of the CFD boundaries relative to the atomic (actual) walls. If δ varies substantially with density (or any other fluid property), the geometry of the enhanced CFD domain becomes dependent on the CFD solution itself. However, for the fluid/solid combination considered in this paper, over the density ranges considered, δ is effectively constant, see Figure 4.2. By using equations (3.7) and (3.8) we can approximate the error of the mass flow rate due to not including this displacement for the cases in this chapter as being between 15–25 %.

Liquid slip velocity at surfaces is calculated using the Navier slip condition:

$$u_{slip} = \xi\dot{\gamma}, \tag{4.1}$$

where ξ is the slip-length and $\dot{\gamma}$ is the shear-rate at the bounding surface. The least-squares-fitted linear velocity profile is used to calculate the slip-length (as defined from the CFD surface). Based on the strain-rate/slip-length relationship proposed in [143], and assuming a linear dependence on density, a least-squares fit is performed to the following equation:

$$\xi = \frac{(c_1\rho + c_2)}{\sqrt{1 - \dot{\gamma}/\dot{\gamma}_c}}, \tag{4.2}$$

where ρ is the density, $\dot{\gamma}_c$ is the critical shear rate (see [143]), and c_1, c_2 and $\dot{\gamma}$ are

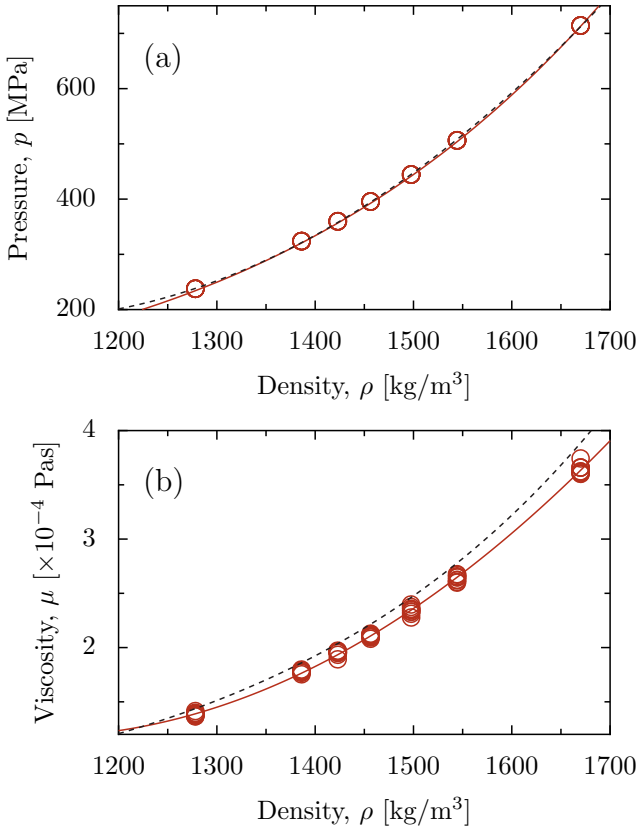

Figure 4.1: Data for the Lennard-Jones fluid properties: (a) pressure variation with density, and (b) viscosity variation with density. MD data points from pre-simulation (circles), fitted polynomial (solid lines) and NIST data [83] (dashed lines).

parameters of the fit to our MD pre-simulations, which are $-1.2052 \times 10^{-12}\,\mathrm{kg^{-1}m^4}$, $3.7468 \times 10^{-9}\,\mathrm{m}$ and $1.5431 \times 10^{11}\,\mathrm{s^{-1}}$, respectively. Figure 4.3 shows our MD pre-simulation data and the least-squares fit of equation (4.2); results are shown for three different values of density. The slip model approximated by equations (4.2) and (4.1) is directly introduced as a Robin boundary condition in the enhanced CFD solver.

4.3 Steady Simulations

4.3.1 Cases

To test the reliability of our predictions using CFD enhanced with MD pre-simulation input, we compare them to results from full-domain MD calculations. We also compare results with predictions from compressible CFD with no-slip at the wall, and

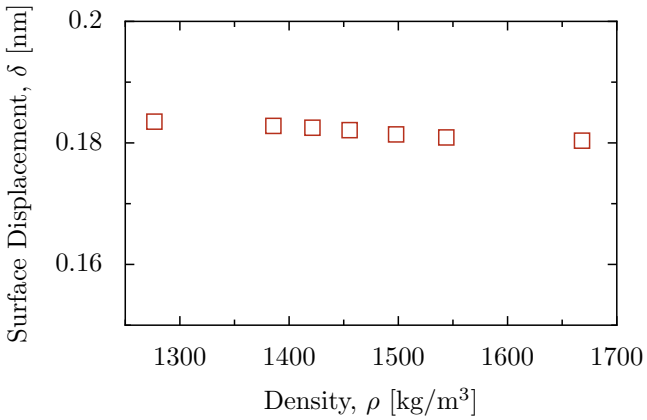

Figure 4.2: Surface displacement δ varying with fluid density ρ, measured from each MD pre-simulation.

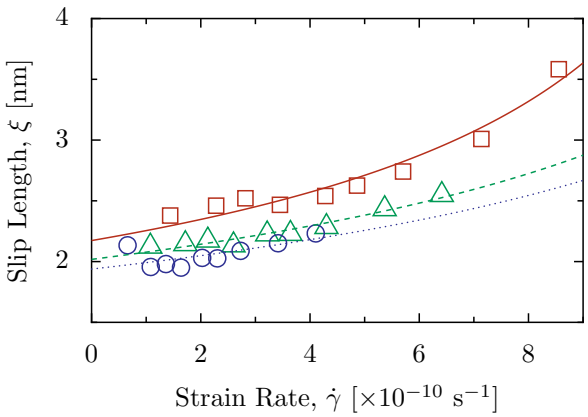

Figure 4.3: Slip length ξ varying with strain rate $\dot{\gamma}$ for three density values $\rho_1 = 1276\,\mathrm{kg/m^3}$, $\rho_2 = 1447\,\mathrm{kg/m^3}$ and $\rho_3 = 1668\,\mathrm{kg/m^3}$. MD pre-simulation data points (symbols) and fit to equation (4.2) (dashed lines).

without modelling the CFD surface displacement (referred to as 'no-slip CFD'). We also compare with incompressible CFD with the same slip model but no surface displacement (referred to below as 'incomp. slip CFD'). As test cases, we choose flows that all exhibit non-continuum behaviour (e.g. slip at surfaces), but also contain a significant bulk flow region, even within the smallest features of the geometry. In Chapter 5 we consider the quality of CFD predictions in cases where such a bulk region does not exist.

The two-dimensional cases we consider in this section involve connected reservoirs that are held at different pressures; an example of a filtration configuration, say. The first case has the reservoirs connected by a straight channel 108.8 nm long (Case 1), the second by a straight channel 231.2 nm long (Case 2), and the third by

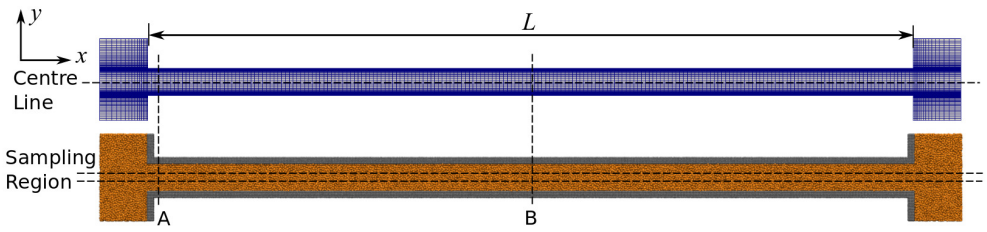

Figure 4.4: Two-dimensional CFD mesh (top) and MD domain (bottom): Case 1, $L = 108.8\,\text{nm}$; Case 2, $L = 231.2\,\text{nm}$. Both channels are of width $4.08\,\text{nm}$.

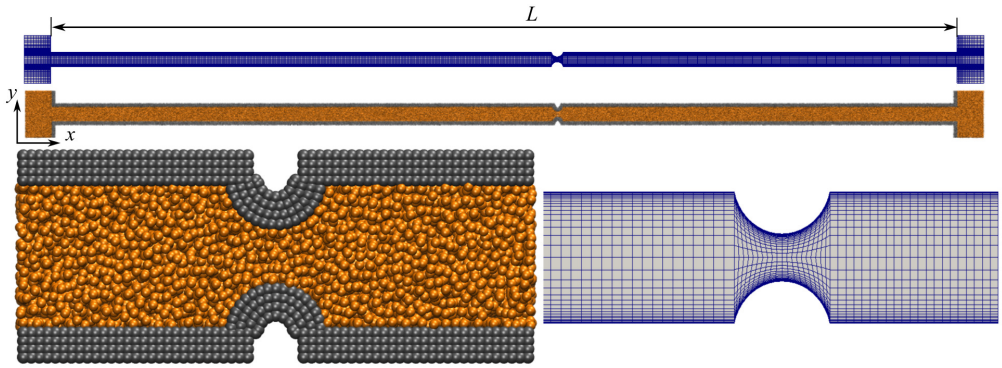

Figure 4.5: Two-dimensional CFD and MD domains for Case 3 (top); close-up view of the channel irregularity (bottom) as an MD realisation (left) and a CFD mesh (right).

a $231.2\,\text{nm}$ long straight channel with a cylindrical geometrical irregularity / defect with radius $0.68\,\text{nm}$ (Case 3). The channel width (measured as the distance between the centre of opposite solid surface atoms) is $4.08\,\text{nm}$ for all three cases. Figure 4.4 shows the CFD meshes for Case 1 and case 2 alongside the corresponding full MD domain. Figure 4.5 shows the CFD and MD domain for Case 3 ($L = 231.2\,\text{nm}$, with channel width of $4.08\,\text{nm}$; the width at the defect is $1.7\,\text{nm}$). For all three cases, the pressure at the inlet and outlet reservoir are $650\,\text{MPa}$ and $300\,\text{MPa}$, respectively. The full MD simulations are used to evaluate the accuracy[1] of the enhanced CFD predictions by comparison.

4.3.2 Mesh dependency study

A mesh dependence study is performed on Case 2. The domain of Case 1 is just a shortened version of Case 2, and Case 3 is essentially the same as Case 2, but with the added defect; therefore, performing the study on Case 2 should be representative of all cases cases. This study is performed using the same simulation for each domain,

[1]Strictly speaking, we mean 'MD accuracy' here, but for brevity we just refer to 'accuracy'.

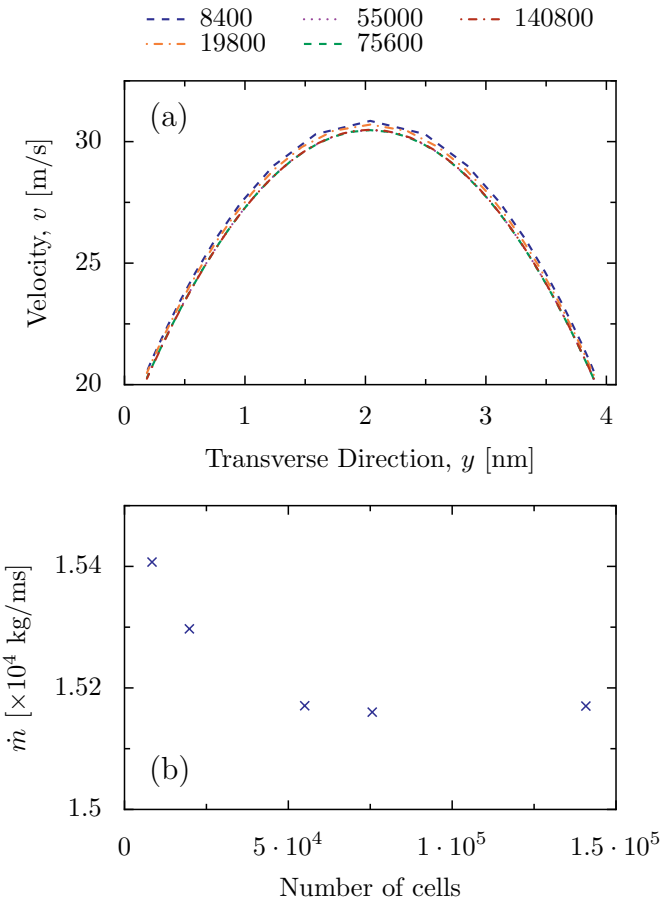

Figure 4.6: The results from the mesh dependency study are shown: (a) velocity profiles across the middle of the channel, (b) mass flow rate at the middle of the channel for each number of cells.

but with different numbers of cells. The mesh is said to be independent of the result when the result (here the steady-state mass flow rate and certain velocity profiles) do not change significantly as the number of cells increase.

We have performed simulations of Case 2 with meshes having cell numbers in the range between 8,400 and 140,000. We found that the percentage difference in the calculated mass flow rate between 55,000 and 140,000 cells was less than 0.1 %, with the velocity also not changing significantly; therefore, we use 55,000 cells for Case 2 and 3 in this section. As Case 1 is about half the length of Case 2 we use 30,000 cells. The results from these mesh dependency studies are shown in Fig. 4.6.

Table 4.1: Mass flow rate predictions (per unit length, because of the 2D geometry) for each channel case and model. The percentage difference (error) between the mass flow rates predicted by the CFD models and the full MD results are presented in parentheses.

	full MD $\dot{m}_{md} \times 10^{-4}$ [kg/m/s]	enhanced CFD $\dot{m}_A \times 10^{-4}$ [kg/m/s]	no-slip CFD $\dot{m}_B \times 10^{-4}$ [kg/m/s]	incomp. slip CFD $\dot{m}_C \times 10^{-4}$ [kg/m/s]
Short Channel	3.25	3.18 (-2.3%)	1.13 (-65%)	4.21 (+29%)
Long Channel	1.57	1.51 (-3.7%)	0.53 (-66%)	2.09 (+33%)
Defect Channel	1.32	1.35 (+2.2%)	0.49 (-63%)	1.87 (+41%)

4.3.3 Results

Figure 4.7 (a-c) and Figure 4.8 (a-c) show results of pressure and density, respectively, along the centreline of each domain for each case. Both the centre line and the sampling region (where averaging is performed) are indicated on Figure 4.4. In Figures 4.7 and 4.8, differences between the CFD and MD results can be seen near the outermost boundaries of the reservoirs. This is because in the full-domain MD, for convenience the reservoirs are connected by periodic boundary conditions, with a body force imposing the pressure drop (see [34] for details of this approach); in the CFD, however, boundary pressures can be specified directly and so periodicity need not be enforced.

Velocity profiles cross-channel are presented in Figures 4.9 and 4.10 at cross-sections A and B (as indicated on Figure 4.4) for Cases 1 and 2. The streamwise velocity along the centre line of the channel for Case 3 is presented in 4.11. Finally, in Table 4.1, predictions for the mass flow rate through each channel are given.

In all three cases, the agreement between our enhanced CFD model (the dashed lines in Figures 4.7, 4.8, 4.9, 4.10, and 4.11) and the MD results (solid lines) is extremely good for all of the flow variables considered. Also, CFD predictions of mass flow rate (arguably the most important bulk property in nano channel flow cases, and one that no-slip CFD underpredicts very substantially) are all within 4 % of the values obtained from full MD simulations. This very positive result is reassuring given the non-trivial nature of the geometry considered in Case 3, with the small non-planar irregularity in the channel. The MD simulation results show this small defect reduces the mass flow rate by more than 10 % (compared to the otherwise identical Case 2). Again, our enhanced CFD technique captures this effect accurately: the flow rate is reduced by 12 %.

Table 4.3 provides an indication of the computational cost for the three full-

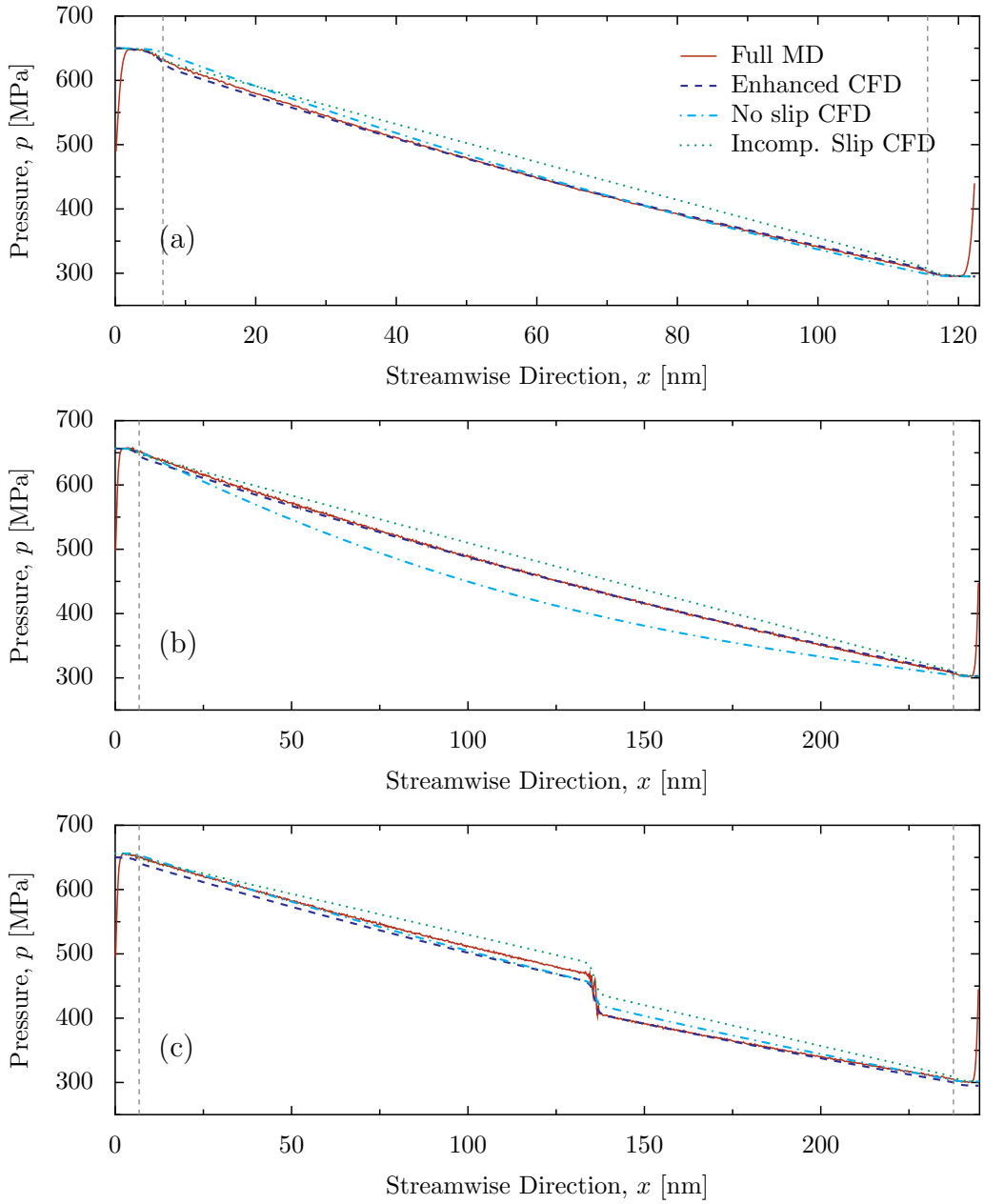

Figure 4.7: Pressure along the centerline of (a) Case 1 (short channel), (b) Case 2 (long channel), and (c) Case 3 (defect channel). The vertical lines at $x = 6.8\,\text{nm}$ and $x = 115.6\,\text{nm}$ (for Case 1) and at $x = 6.8\,\text{nm}$ and $x = 238\,\text{nm}$ (for Cases 2 and 3), indicate the inlet and outlet positions, respectively. Full MD (solid), enhanced CFD (dashed), no-slip CFD (dotdashed) and incomp. slip CFD (dotted).

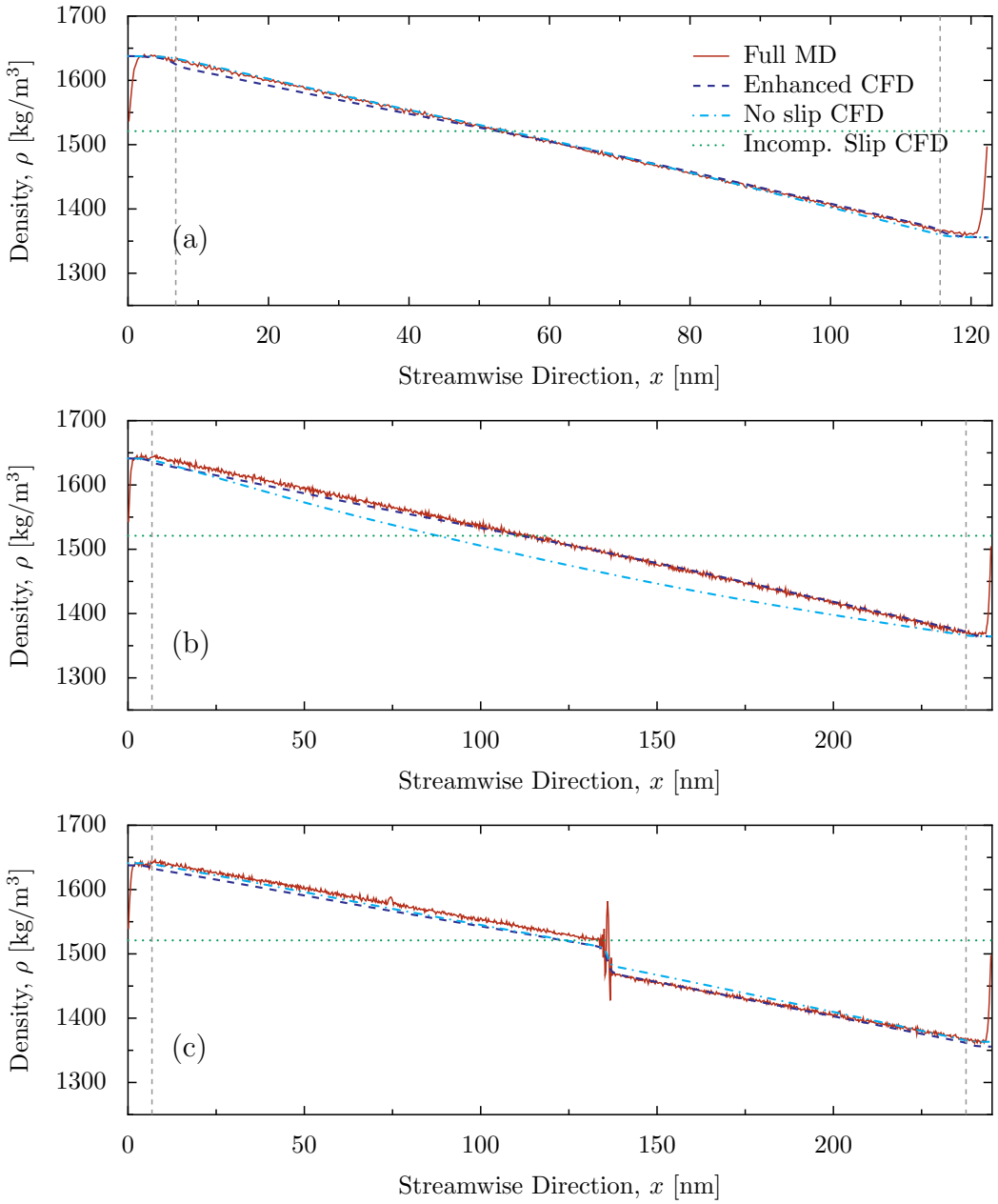

Figure 4.8: Pressure along the centerline of (a) Case 1 (short channel), (b) Case 2 (long channel), and (c) Case 3 (defect channel). The vertical lines at $x = 6.8\,\text{nm}$ and $x = 115.6\,\text{nm}$ (for Case 1) and at $x = 6.8\,\text{nm}$ and $x = 238\,\text{nm}$ (for Cases 2 and 3), indicate the inlet and outlet positions, respectively. Full MD (solid), enhanced CFD (dashed), no-slip CFD (dotdashed) and incomp. slip CFD (dotted).

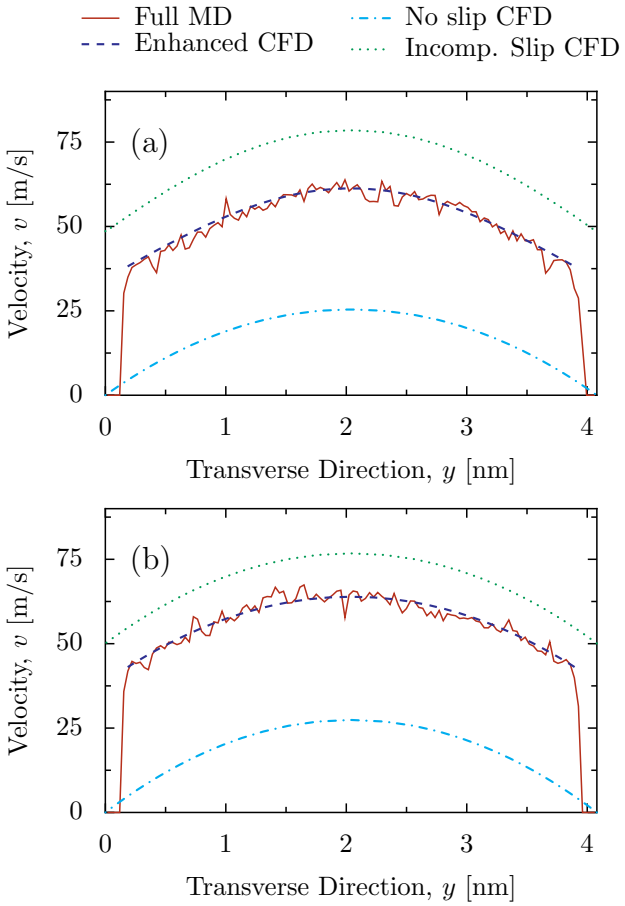

Figure 4.9: Streamwise velocity profiles for Case 1 at (a) section A; (b) section B. Full MD (solid), enhanced CFD (dashed), no-slip CFD (dotdashed) and incomp. slip CFD (dotted).

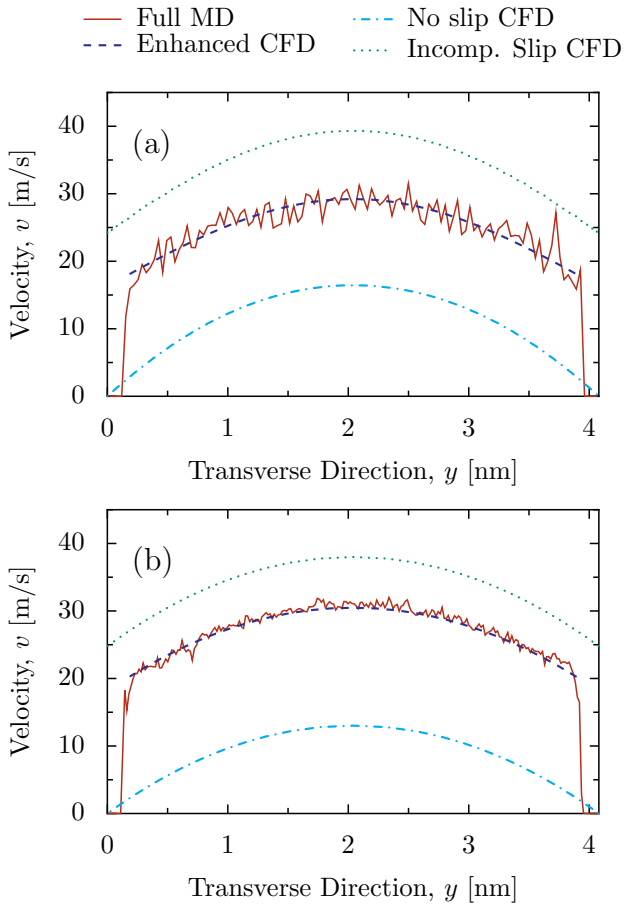

Figure 4.10: Streamwise velocity profiles for Case 2 at (a) section A; (b) section B. Full MD (solid), enhanced CFD (dashed), no-slip CFD (dotdashed) and incomp. slip CFD (dotted).

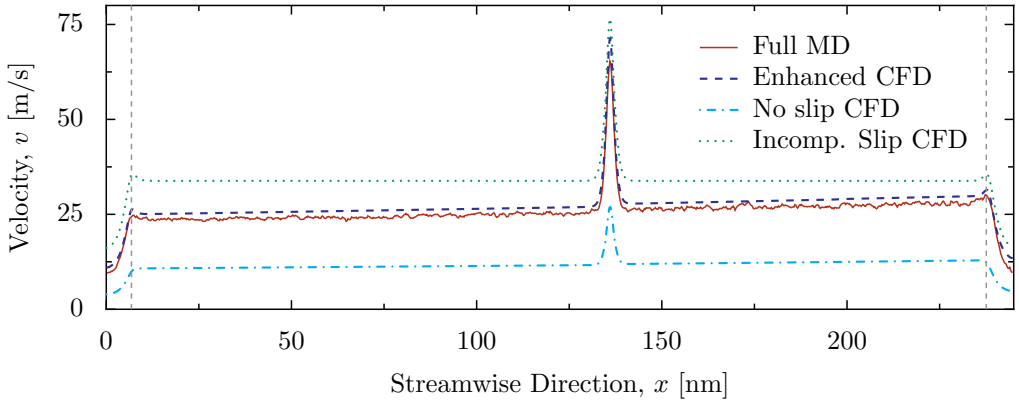

Figure 4.11: Streamwise velocity profiles for Case 3 along the centre line. The vertical lines at $x = 6.8\,\text{nm}$ and $x = 238\,\text{nm}$ represent the inlet and outlet, respectively. Full MD (solid), enhanced CFD (dashed), no-slip CFD (dotdashed) and incomp. slip CFD (dotted).

Table 4.2: Computational costs: the first three rows are the full MD simulations, while the last row is the MD pre-simulation that is used to collect the data for the enhanced CFD.

	CPUs	Liquid molecules	Wall molecules	time per MD time-step	total computational time
Short Channel	24	89,146	133,424	0.7 s	10 days
Long Channel	24	162,084	275,280	1.3 s	18 days
Defect Channel	24	161,369	276,830	1.3 s	18 days
MD pre-simulations	24	5073 to 6668	4160	0.14 s	4 days per liquid/solid combination

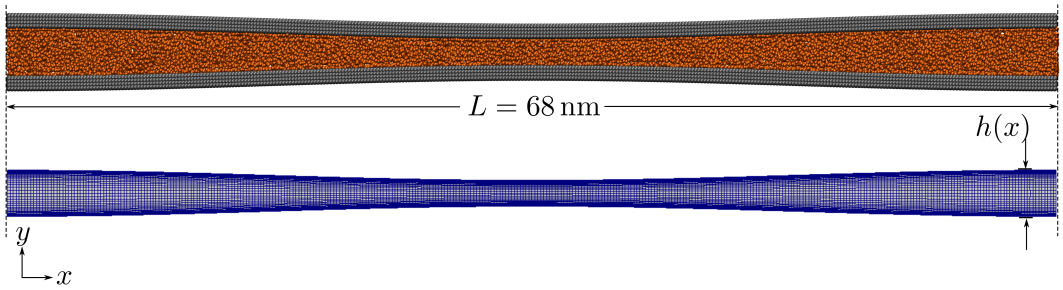

Figure 4.12: The converging-diverging channel used in the unsteady cases. Top is the MD domain, and bottom is the CFD domain.

domain MD simulations. The longest simulations presented in this chapter ran in parallel (on 24 CPUs) for 18 days. The laminar-flow CFD itself has a negligible cost by comparison, although, the MD pre-simulations also require the computational resources indicated in the last row of Table 4.3. However, these pre-simulations need only be performed once for a particular fluid/solid combination, and then used for any number of flow geometries thereafter.

4.4 Unsteady simulations

4.4.1 Cases

We consider a two-dimensional geometry: a converging-diverging channel with a smoothly varying height in the streamwise direction. A gravity-type force is applied to the fluid to generate an unsteady/transient flow. As test cases, we choose flows that exhibit non-continuum behaviour (e.g. slip at surfaces), and do not contain a

significant bulk flow region, i.e., the width of the channel is at the 2–3 nm continuum-fluid limit for a Lennard-Jones fluid.

The converging-diverging channel is shown in Figure 4.12 and has a length $L = 68\,\text{nm}$ in the streamwise direction x, a depth of 5.44 nm, and heights of 3.4 nm and 2.04 nm at the inlet and throat sections, respectively. The channel is periodic in both the streamwise and spanwise direction. The height between top and bottom walls $h(x)$ varies in the streamwise direction according to a sinusoidal function,

$$h(x) = 2a\left[\cos\left(\frac{2\pi x}{l}\right) - 1\right] + h_{\text{inlet}}, \tag{4.3}$$

where $4a = 1.36\,\text{nm}$ is the change of height from inlet to throat, and h_{inlet} is the height of the channel at the inlet.

The full MD domain is divided into 200 bins in the x-direction of bin-width $\delta x = 0.34\,\text{nm}$, and the instantaneous mass flow rate and density are measured in each bin. In the enhanced CFD, we define a plane across the channel at equivalent positions, and sum the mass flux from each cell the plane crosses, at each time-step, to get the instantaneous data.

All the flows start from rest, then a time-varying gravity force $\bar{F}(t)$ is applied. We consider four different forces applied to the fluid:

1. **Startup flow**: a steady gravity force of $\bar{F} = 0.487\,\text{pN}$;

2. **Short oscillations**: an unsteady, oscillating gravity force with amplitude 0.487 pN and period of $T = 0.22\,\text{ns}$, i.e.

$$F_g(t) = 0.487 \times 10^{-12} \sin\left(\frac{2\pi t}{0.22 \times 10^{-9}}\right), \tag{4.4}$$

   where t is the simulation time;

3. **Long oscillations**: an unsteady oscillating gravity force of the same amplitude, but with a larger period $T = 10.8\,\text{ns}$, i.e.

$$F_g(t) = 0.487 \times 10^{-12} \sin\left(\frac{2\pi t}{10.8 \times 10^{-9}}\right), \tag{4.5}$$

   where t is the simulation time;

4. **Varying oscillations**: an unsteady oscillating gravity force with the same amplitude but with increasing period of $0.2 \rightarrow 10.8\,\text{ns}$ as shown in Figure 4.13(d), where the dashed line indicates how the period of the oscillation changes.

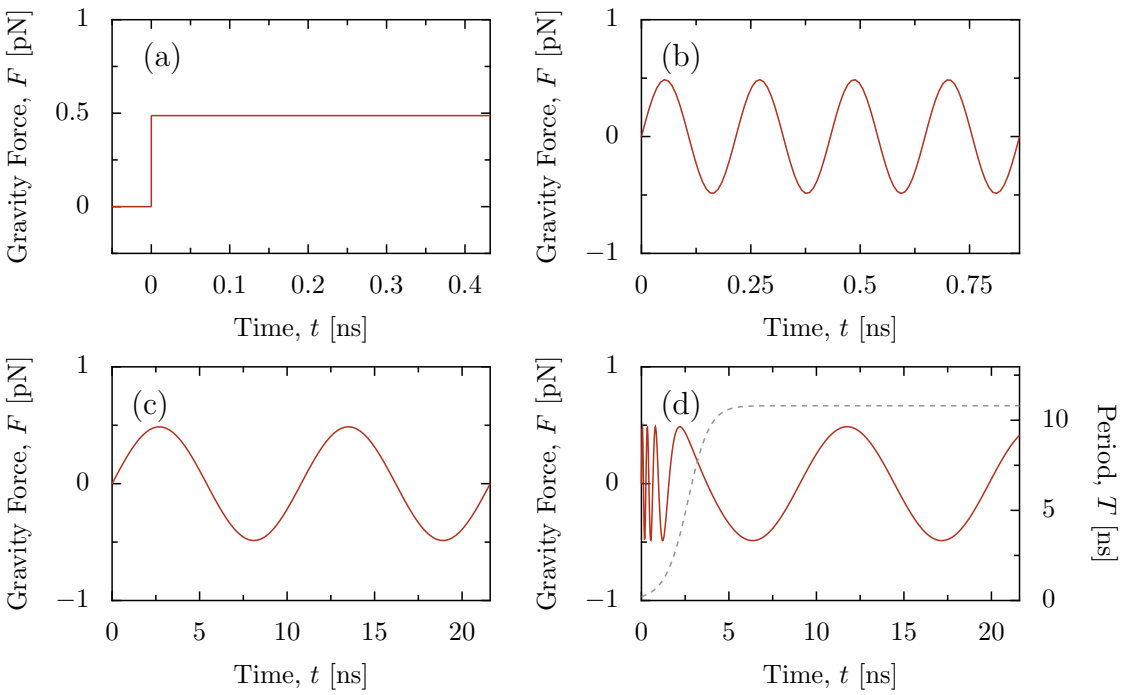

Figure 4.13: The applied gravity forces varying with time for the four different cases: (a) step force, (b) oscillating gravity force with period $T = 0.22\,\text{ns}$, (c) oscillating gravity force with period $T = 10.8\,\text{ns}$, and (d) oscillating gravity force with increasing period $T = 0.22\,\text{ns} \rightarrow 10.8\,\text{ns}$, where the dashed line shows how the period of oscillation changes.

Graphical representations of how the forces vary are shown in Figure 4.13.

4.4.2 Dependency studies

Similar to section 4.3, we must perform dependency studies to make sure that the results are not dependent on the mesh, but as these are unsteady simulations we must also guarantee that the results are independent of the time-step and the number of PISO loops used. As we require accurate results through time, the dependency studies performed compare temporal variations in the mass flow rates. The geometry of the channel remains the same for each case, we only perform this study on Case 1, the startup flow, as we expect the most rapid variations in this case, so if the number of cells, time-step and number of PISO loops is sufficient for this case we need not consider the other cases for this dependency study.

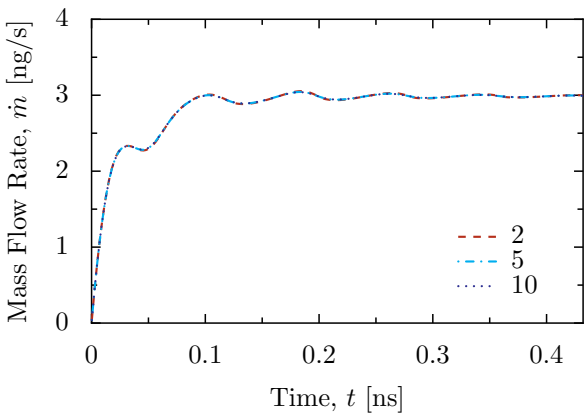

Figure 4.14: Mass flow rate versus time for different numbers of PISO loops.

Number of PISO loops dependency study

We performed simulations in which we used 2, 5 and 10 PISO corrector loops. We found that the results are not significantly affected; see Figure 4.14. Therefore, only 2 PISO corrector loops are used for the rest of this section, as is typical in CFD.

Mesh dependency study

To test that the results are both mesh and time-step independent, we must perform simulations of a range of different meshes and for each mesh use a range of different time steps. Five different numbers of cells are chosen ranging from 2,000 cells to 400,000 cells, to find the optimum number of cells. For each mesh we check that the time-step used is small enough to obtain accurate temporal results, for each mesh, we compare how the time variation of mass flow rate for different time-step sizes.

For each mesh we choose the maximum time-step for which the mass flow rate is unaffected. The results for all the meshes with their maximum time-steps are then compared in Fig. 4.17(a). The mass flow rate at steady state for each mesh are shown in 4.17(b). We found that for a time-step of 21.6 fs and number of cells of 36,000 cells the results are unaffected.

4.4.3 Results

To test the reliability of our predictions using CFD with MD pre-simulation input, we compare results with full-domain Molecular Dynamics calculations (referred to as Full MD). To test whether our enhanced CFD model is an improvement over conventional CFD, we also compare results with predictions from compressible CFD with no-slip at the wall, and without incorporating a CFD surface displacement

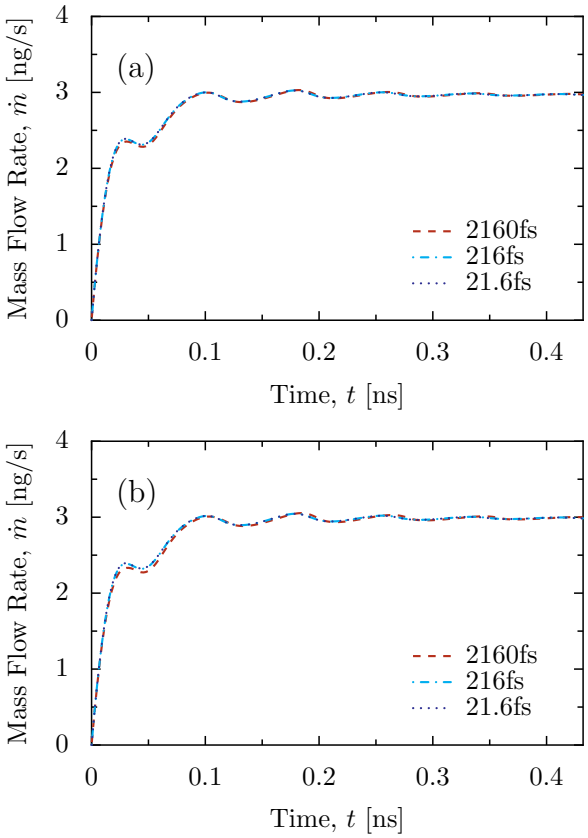

Figure 4.15: Mass flow rate versus time for different time-steps for meshes with (a) 2,000 cells and (b) 36,000 cells.

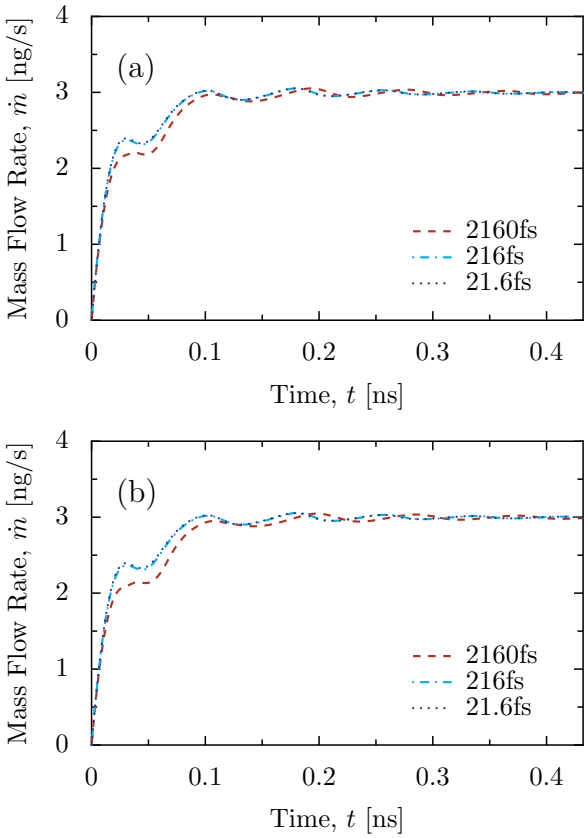

Figure 4.16: Mass flow rate versus time for different time-steps for meshes with (a) 196,000 cells and (b) 400,000 cells.

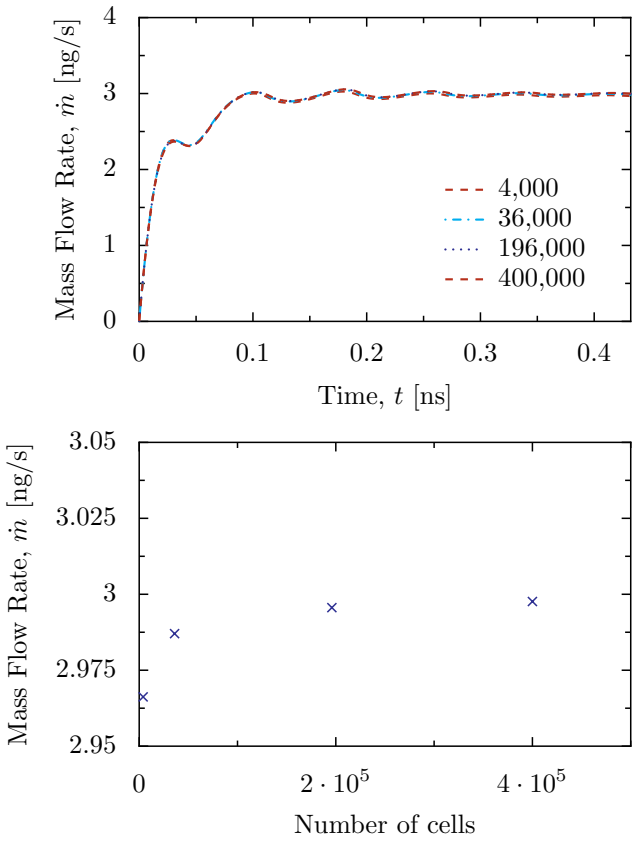

Figure 4.17: (a) Mass flow rate versus time comparing different numbers of cells, (b) Steady-state mass flow rate versus number of cells.

(referred to as 'no-slip CFD'). We also compare with incompressible CFD with slip incorperated but no surface displacement (referred to below as 'incomp. slip CFD').

In Figures 4.18 and 4.19 we plot the mass flow rate variation with time in a single bin near the inlet of the channel for each case. We see that in all cases the enhanced CFD model is able to accurately predict how the mass flux will change in time. Figure 4.18(a), in which a constant force is applied throughout the channel, shows that the CFD reaches steady state at the same time as the MD simulation and that a similar final mass flow rate is reached. There are, however, substantial differences between the enhanced CFD, the no-slip CFD, and the incomp. slip results. The oscillations that are observed at the early times in Figure 4.18(a) in the enhanced CFD results and also the MD data are due to an acoustic response of the nano channel to impulse forcing. A first estimate of the natural acoustic period is obtained by $T = L/c = 0.07\,\text{ns}$ where c is the speed of sound [2]. This corresponds reasonably closely with the observed kinks in the mass flow rate.

In Figure 4.18(b) shows the results when an oscillating force with period 0.22 ns is applied. The mass flux in the enhanced CFD oscillates with the right frequency, the correct amplitude, and is also in phase with the Full MD results. The no-slip CFD, on the other hand, appears to have the correct frequency but the amplitude is incorrect and it is oscillating out of phase, while the incomp. slip is in phase but over predicts the amplitude.

In Figure 4.19(a) we have an oscillating force with period 10.8 ns. The mass flux in the enhanced CFD oscillates with the right frequency, correct amplitude, and is in phase, whereas the no-slip CFD appears to have the correct frequency and it is oscillating in phase, but the amplitude is incorrect. In Figure 4.19(b) the period of the oscillating force increases from 0.22 ns to 10.8 ns; even in this more elaborate case, the enhanced CFD prediction is accurate.

Table 4.3 provides an indication of the computational cost for the full-domain MD simulations. The longest simulations presented in this paper ran in parallel (on 24 CPUs) for 48 days. The enhanced CFD itself has negligible computational cost by comparison, although the MD pre-simulations require the computational resources indicated in the last row of Table 4.3. However, these pre-simulations need only be performed once for a particular fluid/solid combination, and then can be used for any number of flow geometries thereafter.

[2] Measured for a Lennard-Jones fluid at the correct state point using MD simulations. It is calculated using the equation $c = \sqrt{\mathrm{d}p/\mathrm{d}\rho}$. For this calculation $c = 971\,\text{m/s}$.

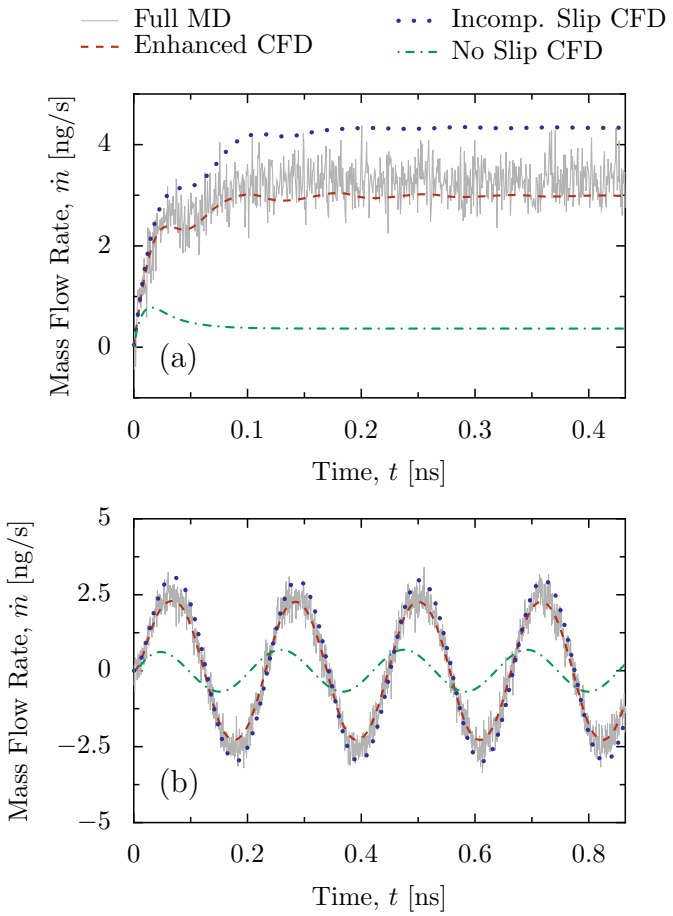

Figure 4.18: The mass flow rate near the inlet of the channel varying with time, for each case. The solid lines are the Full MD results, the dashed lines are the enhanced CFD results, the dotted lines are the incomp. slip CFD results and the dot dashed lines are the no-slip CFD results. (a) step force, (b) oscillating gravity force with period $T = 0.22\,\text{ns}$.

Table 4.3: Computational costs: the first four rows are the Full MD simulations, while the last row is the MD pre-simulation that is used to collect the data for the enhanced CFD.

	CPUs	Liquid molecules	Wall molecules	time per MD time-step	total computational time
Startup flow	24	69,264	19,677	0.68 s	16 hours
Short oscillations	24	69,264	19,677	0.68 s	30 hours
Long oscillations	24	69,264	19,677	0.68 s	48 days
Varying oscillations	24	69,264	19,677	0.68 s	48 days
MD pre-simulations	24	5,073 to 6,668	4,160	0.14 s	4 days per liquid/solid combinatio

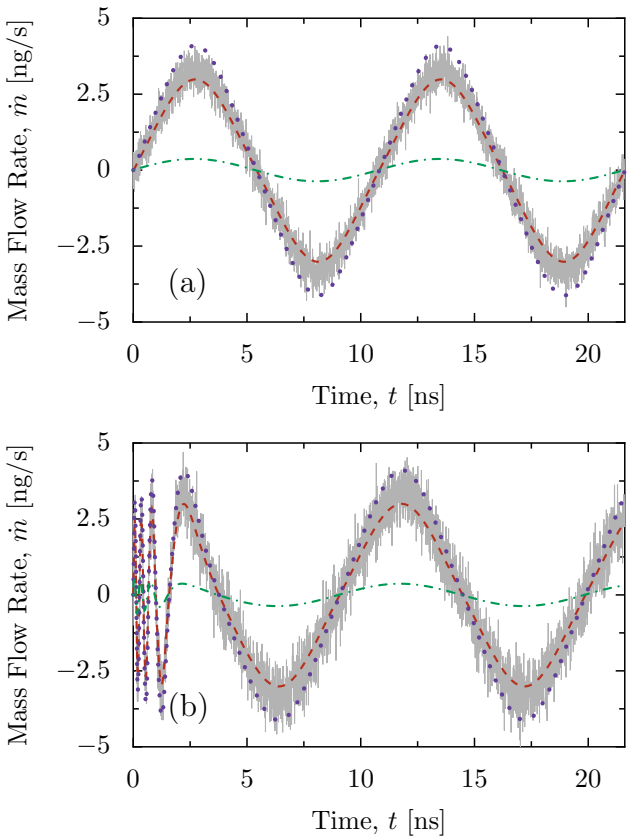

Figure 4.19: The mass flow rate near the inlet of the channel varying with time, for each case. The solid lines are the Full MD results, the dashed lines are the enhanced CFD results, the dotted lines are the incomp. slip CFD results and the dot dashed lines are the no-slip CFD results. (a) oscillating gravity force with period $T = 10.8\,\text{ns}$, and (b) oscillating gravity force with increasing period $T = 0.22 \rightarrow 10.8\,\text{ns}$.

4.5 Summary

In this chapter we have demonstrated our procedure for solving nano-scale flows using CFD. The state, constitutive, and boundary condition information for the CFD solver is extracted from MD pre-simulations, using the methodology presented in Chapter 3. We have shown that this enhanced solver can then provide good predictions for a range of nano-scale flow geometries and under varying conditions to capture steady and unsteady phenomena. This was done by applying it to straight channels under a constant pressure difference and to a converging-diverging channel with gravity-type forces applied, which varied in time. For all cases the mass flow rates measured agreed well with MD simulations performed under the same conditions.

Chapter 5

Application 1: carbon nanotubes (CNTs)

5.1 Introduction

In this chapter we test the robustness of our enhanced CFD technique for cases where, in some region of the flow field, the continuum-fluid assumption is far from being valid, and where there also exist large regions of bulk fluid for which MD is prohibitively expensive. Clearly, this kind of flow is difficult to describe accurately with a continuum-fluid model, but we demonstrate that reasonable results can still be obtained for some spatially- and temporally-averaged properties.

Water desalination is one of a number of applications that have been proposed for CNTs. To filter out the ions in this application the nanotubes would need to be of the order ∼0.8 nm — well below the applicable range of a continuum model. As such, we will study larger CNTs, with diameters ∼2 nm. These sized nanotubes are found in biological channels such as the protein cavity inside tetrabrachion [122], ion channels [27], and orifices created by membrane electroporation [144].

5.2 Modelling of CNTs

The flow of water through CNTs has recently been the focus of substantial research effort [3] mainly due to the extremely high flow rates that have been both predicted [104] and measured [96, 158]. These flow rates are often expressed as an enhancement factor, which is the ratio of water flow rates along the CNT to those predicted by classical fluid dynamics (i.e. the Hagen-Poiseuille equation). The low friction associated with this water transport, and the high selectivity of CNTs, makes CNTs

(and other nanotubes) excellent candidates for high-efficiency desalination and other filtration applications. The high flow rates, often reported as being orders of magnitude greater than classical flow theory predicts [158], are typically attributed to both weak surface-fluid interactions and molecular ordering/layering that enables water molecules to pass efficiently along the CNT in a semi-ordered or structured manner.

The majority of studies performed on CNTs have been either experimental [57, 92] or using molecular dynamics (MD) [34, 104, 105, 126]. However, the experimental results that have been obtained have been extremely varied [57, 92, 120], the enhancement factors that have been measured range from one (no enhancement) to thousands. MD simulations are extremely computationally expensive, using a GPU a 50 nm CNT takes ~15 days to measure 2 ns. This means that a realistic simulation of a CNT, which are commonly in the μm or mm range, is unfeasible with today's computational power. In addition, to obtain results above the thermal noise a significantly higher pressure gradient is applied to the fluid than would be used in a realistic industrial application. Therefore, CFD and hybrid MD-CFD simulations have a piece to play in the understanding of fluid flow through nanotubes.

To find when the continuum assumption breaks down in CNTs, Thomas *et al.* [140] performed MD simulations and studied the structure of the fluid using an axial distribution function. They found that when the diameter of a CNT is greater than 1.66 nm that the water molecules are smoothly distributed along the channel and, therefore, suggest this as the continuum limit for water in a CNT.

Wang *et al.* [154] performed MD simulations of CNTs with diameters below 1.66 nm, and used a more realistic pressure difference than other MD studies. They compared their results to no-slip Hagen-Poiseulle equations; they found that the continuum results were not able to match the MD because of the lack of a slip boundary condition. The velocity profiles were dissimilar due to the layering of the molecules in such small tubes.

A comparison between MD and CFD was performed by Huang *et al.* [59]; using a CNT with a diameter of 2.2 nm. Despite their use of the no-slip boundary condition they obtained good agreement in the streamwise profiles, but not in the radial profiles. Again, this was due to the structure that the liquid molecules form near the boundaries of the tube.

Both Popadić *et al.* [116] and Jamali and Shoghl [63] have performed incompressible CFD simulations with partial-slip boundary conditions to model nanopores. Popadić *et al.* found good agreement with MD simulations and used their simulations to study curvature effects on the pressure drop that occurs at the entrance

and exit to the nanopore. By introducing a curved entrance and exit they were able to reduce the pressure drops and thus increase the flow rate through the nanopore. Jamali and Shoghl studied the effects different physical attributes (such as temperature, length and inlet pressure) have on the enhancement of flow rates compared to no-slip Hagan-Poiseulle flow. As expected, they found that only by changing the slip length did they obtain any enhancement.

Gărăjeu *et al.* [44] have created a continuum model using a second gradient theory and a varying viscosity towards the wall of the nanotube that they believe naturally includes and explains the slip at the wall. However, it is likely that this explanation for slip generation is incorrect, because it has been shown by Sendner *et al.* [131] that the slip length is dependent on the fluid-wall interaction.

There has also been work to create an analytical model by modifying the classical Hagen-Poiseuille equation for the velocity of the fluid. Mattia and Calabrò [95] have developed a two viscosity model and a partial slip boundary condition. They try and take into account the high variation in density close the wall by having an effective viscosity near to the wall and a bulk viscosity in the center of the channel.

In addition, the Hagen-Poiseulle equations have been modified to include partial-slip boundary conditions and the pressure drop at the inlet and outlet [133, 153, 155], to give an equation for the pressure loss in terms of the mass flow rate. The inlet and outlet pressure loss Δp_e can be approximated [130, 137, 155] by

$$\Delta p_e = \frac{3\dot{m}\mu}{\rho r^3}, \tag{5.1}$$

and the pressure drop along a cylinder Δp_{HP} can be predicted from the Hagen-Poiseuille equations as

$$\Delta p_{HP} = \frac{8\mu L\dot{m}}{\pi\rho r^3(r+4\xi)}. \tag{5.2}$$

Therefore, the total pressure drop Δp can be approximated as

$$\Delta p = \left[3 + \frac{8L}{\pi(r+4\xi)}\right]\frac{\dot{m}\mu}{\rho r^3}. \tag{5.3}$$

None of the continuum models described here have taken into account the compressibility that occurs at the nano-scale, or include a notion of a surface displacement to obtain the continuum result. By using our enhanced CFD model we will be able to accurately model the surface offset and the compressibility, as well as the slip length.

5.3 Pre-Simulation results for water

The MD pre-simulations for this case are constructed identically to those of Chapter 3, including the dimensions of the geometry. Here, though, the TIP4P/2005 molecular water model is used to describe the condensed phase of water, while the solid boundary walls consist of atom-thick graphene sheets that are modelled using 663 frozen carbon atoms. The exact interatomic potentials used and a description of the water model are given in Section 2.3.3. As water is a well-known fluid, we use data from NIST [83] for the pressure-density and density-viscosity relationships, both of which are fitted to quadratic polynomials. For the pressure-density relationship the equation used is $p = 0.00684\rho^2 - 11.49\rho + 4655$, and for the density-viscosity relationship we use: $\mu = 1.413 \times 10^{-8}\rho^2 - 2.879 \times 10^{-5}\rho + 0.01555$.

MD pre-simulations provide values for the surface displacement (i.e. from the carbon atoms to the fluid) and the slip length over the range of densities within the channel. As the strain rate is low we only use three data points to model a linear dependency of the slip length on density i.e.

$$\xi = c_1\rho + c_2, \tag{5.4}$$

where c_1 and c_2 are parameters of the fit and are $-2.8248 \times 10^{-10}\,\mathrm{kg^{-1}m^4}$ and $3.3117 \times 10^{-7}\,\mathrm{nm}$, respectively, the slip length relationship is shown in Figure 5.1. In this case, for the enhanced CFD simulations we take $\delta = 0.266\,\mathrm{nm}$. By using equations (3.9) and (3.10) we estimate that this value of surface displacement will impact the mass flow rate by ~45–70 %; therefore, it is highly significant.

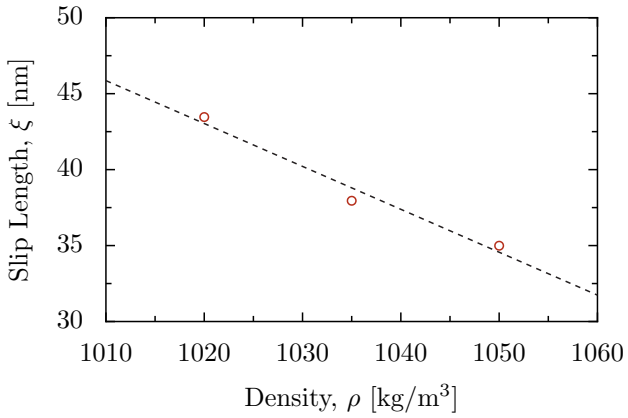

Figure 5.1: Slip length ξ varying with density ρ in the water/graphene case. MD pre-simulation data (circles) with linear fit (dashes).

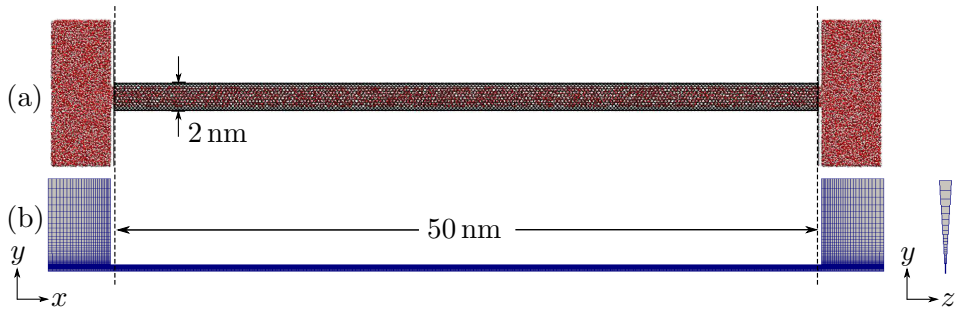

Figure 5.2: A representation of the domain modelled for (a) the MD domain (b) the CFD domain.

5.4 Case setup

The three-dimensional geometry consists of two reservoirs of water, held at different pressures, separated by a (15,15) carbon nanotube (CNT) of length 50 nm and diameter approximately 2 nm, see Figure 5.2(a); since the domain is periodic in the y- and z-directions this setup represents a regularly repeated array of CNTs. To save computational time of the CFD only a 6° wedge of the domain is simulated, with symmetry boundary conditions are used so that the mesh represents the full cylinder, see Figure 5.2(b).

We again compare our enhanced CFD predictions against full MD results and against the standard CFD models outlined in §4.3.1. The pressure difference between the reservoirs is set to be 200 MPa because it is very challenging to obtain useful information from MD using only low pressure differences due to the extended sampling times required to filter low-velocity signals from the thermal noise [104]. These high pressure (and consequently density) differences make the CFD predictions even more challenging. The full MD simulation was performed in parallel on 48 CPUs, with the majority of the computational effort attributable to the two reservoir regions. These have dimensions $4.4 \times 10.6 \times 10.3$ nm and are chosen to be large enough to avoid any effects on the CNT flow due to reservoir boundaries. The intermolecular potentials used are the same as those in the pre-simulation, as given in Section 2.3.3.

5.5 Mesh dependency study

As in the previous chapter, we must perform a dependency study on the number of cells required to obtain results that are independent of the mesh. We measure the mass flow rate at the center of the channel for meshes with between 10,000 and

650,000 cells. The results are plotted in Figure 5.3 and show that the results become effectively mesh independent when 160,000 cells are used. Therefore, the remainder of the simulations presented in this chapter have been performed with 160,000 cells.

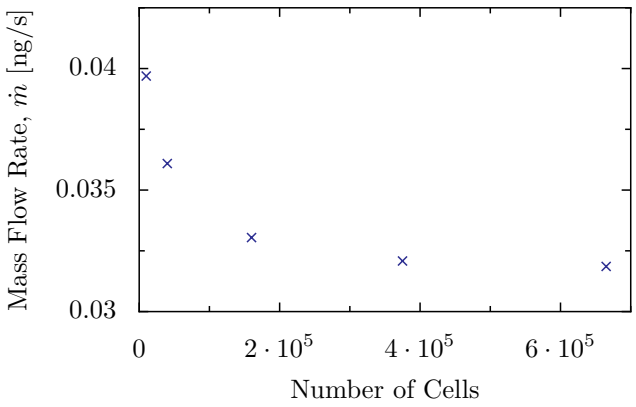

Figure 5.3: Mass flow rate (measured in the middle of the CNT) versus the total number of cells used in the simulation.

5.6 Results

Figure 5.4 shows pressure and density plots along the centreline of the CNT; in the MD this data is collected within a cylinder of radius 0.1577 nm about the centerline. Due to the substantial molecular layering within the CNT (see Figure 5.5(b)) a bulk density effectively does not exist, and the choice of the size of this sampling region can substantially affect the 'bulk' density measured.

The no-slip CFD model does not exhibit large pressure drops at the inlet and the outlet (shown in Figure 5.4 at the grey dashed lines) due to the much lower velocity in the tube (and therefore there are lower accelerations at the inlet and outlet) than in the slip cases; this is shown in equation (5.1) by the dependence on mass flow rate. The classical continuum pressure drop along a cylinder Δp_{HP} can be predicted using equation (5.2); using this the pressure drop is predicted to be ~50 MPa, in good agreement with our CFD results. The MD results, on the other hand, show a channel pressure drop much lower than this. This might suggest that the slip length is larger in the MD than was used in the CFD (as $\xi \to \infty, \Delta p_{HP} \to 0$), possibly due to a geometry dependence, e.g. curvature effects, which is not captured by the pre-simulation methodology.

Despite this the cross-sectional velocity profiles in the centre of the CNT, plotted in Figure 5.5 (a), shows good agreement. The mass flow rate in the full

MD simulation is measured to be 4.3×10^{-14} kg/s, which is 23 % greater than that predicted by our enhanced CFD. That this is a significant improvement on conventional CFD model predictions is indicated in Table 5.1. The under prediction for the enhanced CFD could be explained partly by a lower slip length used than was exhibited in the Full MD and partly by the high variation in the fluid density as shown in Figure 5.5 (b).

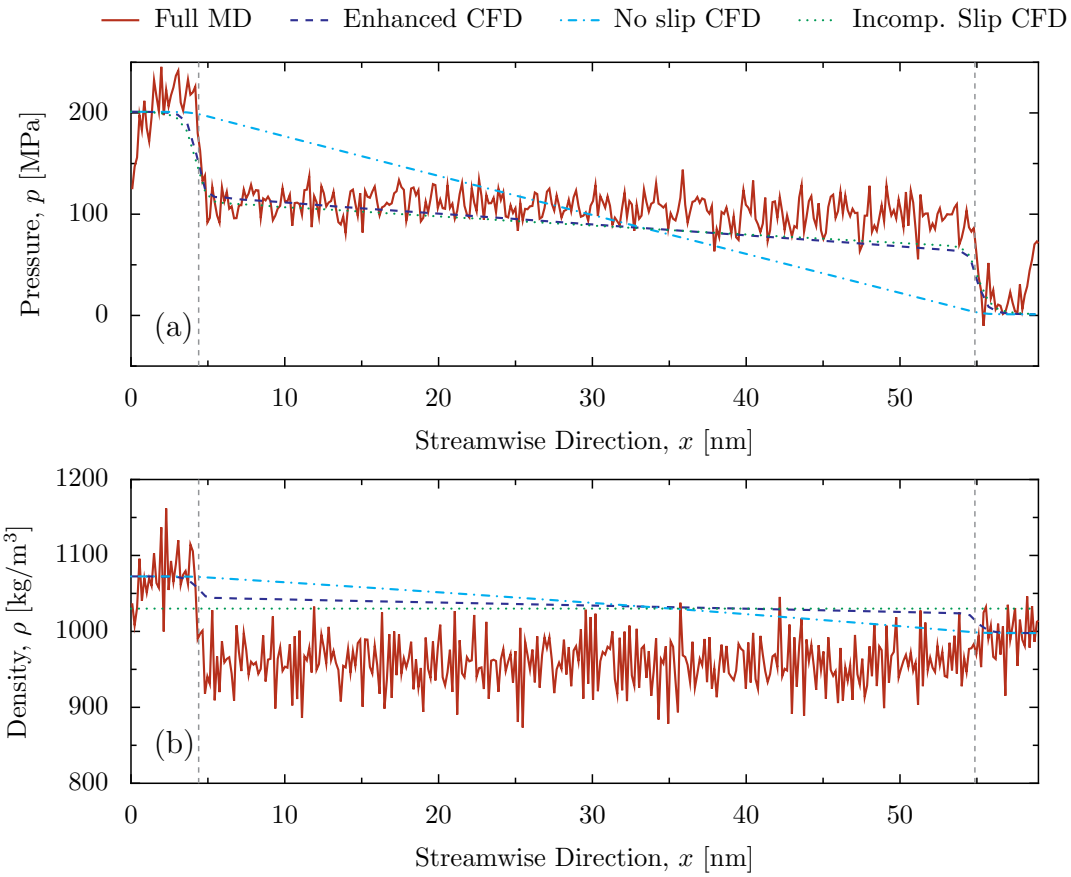

Figure 5.4: Water density and pressure along the centerline of the CNT. The noise in the MD data is due to the relatively small number of molecules being sampled in the absence of a well defined 'bulk-flow' region. The vertical lines at $x = 4.4$ nm and $x = 54.8$ nm represent the inlet and outlet, respectively. Full MD (solid), enhanced CFD (dashed), incomp. slip (dotted) and no-slip CFD (dash-dotted).

Given the ∼2 nm diameter of the (15,15) CNT and despite the molecular layering that actually occurs within the flow field, as evidenced in Figure 5.5 (b), our enhanced CFD approach can be considered reasonably robust in predicting important averaged fluid properties to the correct order of magnitude. These CFD results are obtained with negligible cost in comparison to full MD simulations.

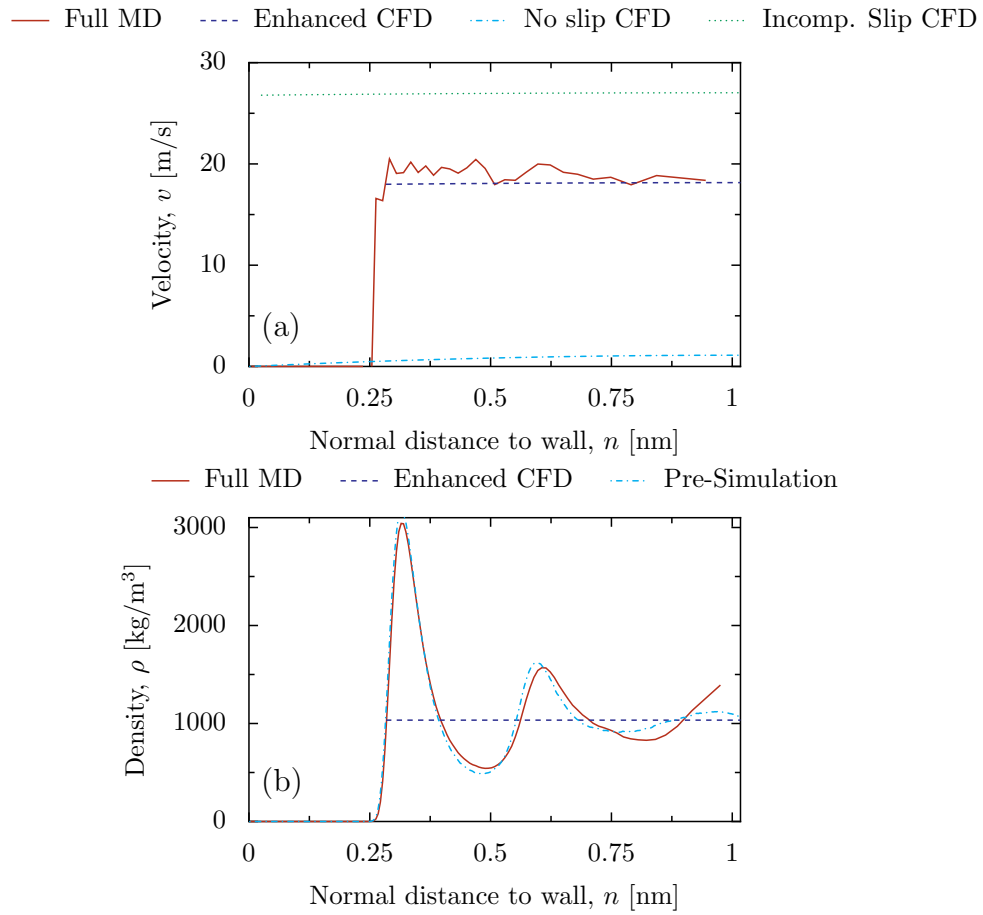

Figure 5.5: (a) Streamwise velocity cross-sectional profile in the longitudinal center of the CNT, and (b) the radial water density profile within the CNT. The vertical lines at $x = 0.266\,\text{nm}$ indicate the position of the CFD surface; the CNT surface atom centres are at $x = 0$.

5.7 Summary

We have shown in this chapter that it is possible to obtain reasonable predictions for three-dimensional flows through nano channels at the continuum limit. The likely reason that our enhanced CFD estimates are reasonable is that the flow in the CNT is dictated by the liquid interaction with the smooth graphitic surface (which is adequately modelled), despite the non-continuum conditions within the fluid. However, there is possibly a curvature dependence on the slip length, which was not included in the MD pre-simulations. This could be rectified by performing pre-simulations of a section of the CNT to capture any geometry dependence on the slip length or surface displacement. As mentioned in Section 3.3.3, if too many pre-simulations are required to obtain data for the parameter space, a concurrent

Table 5.1: Water mass flow rate predictions for each model of the CNT. The percentage difference (error) between the mass flow rates predicted by the CFD models and the full MD results are presented in parentheses.

	full MD ($\dot{m}_{md} \times 10^{14}$ kg/s)	enhanced CFD ($\dot{m}_A \times 10^{14}$ kg/s)	no-slip CFD ($\dot{m}_B \times 10^{14}$ kg/s)	incomp. slip CFD ($\dot{m}_C \times 10^{14}$ kg/s)
CNT	4.3	3.3 (-23%)	0.15 (-97%)	9.0 (+109%)

hybrid methodology, such as using the IMM [125], could be more appropriate to accurately model CNTs of this size.

Chapter 6

Application 2: design optimisation

6.1 Introduction

We now demonstrate how the efficient enhanced CFD model can be used in design optimisation problems at the nano-scale. The example we choose is the optimal design of a bifurcating nano-channel network (see Figure 6.1); such a design exploration would not be feasible using full MD simulations. The problem is to find the optimal geometry of the channels in a bifurcating channel (i.e. that gives greatest mass flow rate), for a constant pressure difference Δp between the inlet and the outlets, and a constant volume V. At the macro-scale the solution to this problem is given by Murray's Law [100, 101, 102], which was first derived using the Hagen-Poiseuille Law to minimise the power required to sustain the flow of blood through vessels. It has also since been shown to describe the water transport though vessels in plants [97], and at the micro-scale it has been used to optimally design MEMS devices having rectangular or trapezoid cross sections [38].

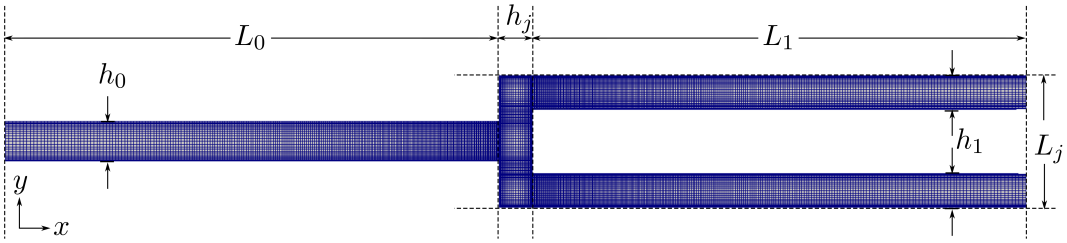

Figure 6.1: The bifurcating channel domain used for the design optimisation. The width of the parent channel is h_0; the width of the two daughter channels are h_1.

Applications of a nano-scale geometry of this type are often referred to being a 'lab-on-a-chip'. Substantial research effort has been put into these because of their ability to provide high, accurate throughput of small amounts of biological and chemical reagents [76, 70, 26]. There have been many proposed applications in nanomedicine and water purification [117]. Y-junction carbon nanotubes [82] have been suggested for the separation of ions [113].

6.2 Optimal channel widths

For a 2D two-level network, like the geometry in Figure 6.1, Murray's Law is

$$h_0^2 = \sum_{n=1}^{N} h_n^2, \tag{6.1}$$

where h_0 is the width of the inlet parent channel, and h_1 to h_N are the widths of the outlet daughter channels. For a symmetric bifurcating channel, where $N = 2$ and $h_1 = h_2$, the optimum ratio of channel widths is

$$\frac{h_0}{h_1} = \sqrt{2}. \tag{6.2}$$

The optimisation we perform, with the given constraints of constant volume and fixed pressure difference, is a linear search on channel width (equal increments) to find the maximum mass flow rate. We choose a volume of $1100\,\mathrm{nm}^3$, a pressure difference of 10 MPa, channel lengths $L_0 = L_1 = 75\,\mathrm{nm}$, a junction length $L_j = 20\,\mathrm{nm}$ and junction width, $h_j = 4\,\mathrm{nm}$. The volume V can be calculated as:

$$V = h_0 L_0 + h_j L_j + 2h_1 L_1. \tag{6.3}$$

If this geometry was optimised using MD, each simulation would take approximately 30 days, whereas, each enhanced CFD simulation takes approximately 500 seconds to perform. Figure 6.2 shows the results from this optimisation with our enhanced CFD model used on a micro-scale channel and on a nano-scale channel. We see that for a micro scale channel, the optimum width occurs when $h_0^2/2h_1^2 = 1$: this is the expected result according to Murray's Law. At the nano-scale, however, we observe a significant deviation from the standard Murray's Law.

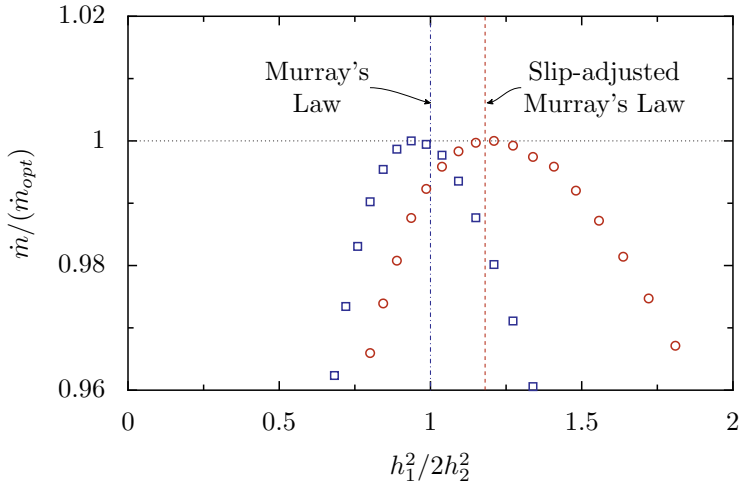

Figure 6.2: The normalised mass flow rate for different ratios of mother/daughter channels widths for micro-scale channels (squares) where the dash-dotted line is the expected optimum, and for nano-scale channels (circles) where the dashed line is the expected optimum.

6.3 Slip-adjusted Murray's law

A deviation from the standard Murray's Law has been noted for rarefied gases [46] but has not so far been demonstrated for a liquid. To uncover the origin of this deviation we derive Murray's Law using Poiseuille's equations with Navier slip at the walls, i.e. $u(h) = u(-h) = \xi \frac{\mathrm{d}u}{\mathrm{d}y}$ where ξ is the slip length, and the velocity is at a maximum at $y = 0$ i.e. $\frac{\mathrm{d}u}{\mathrm{d}y}\big|_{y=0} = 0$. The mass flow rate is then

$$\dot{m} = \frac{2\rho}{3\mu}\frac{\Delta p}{l}h^3\left(1 + \frac{3\xi}{h}\right), \tag{6.4}$$

where $\dot{m}$ is the mass flow rate, ρ is the density, μ is the dynamic viscosity and Δp is the pressure difference between the inlet of the parent channel and the outlet of the daughter channel. Murray's Law is found by minimising the power P required to maintain flow, which for flow through a channel is

$$P = \dot{m}\Delta p + 2bhl, \tag{6.5}$$

where b is a constant of proportionality. By eliminating Δp with equation (6.4) in this equation and differentiating, we find that when the power is minimised the mass flow rate is

$$\dot{m} = kh^2\frac{(1 + 3\xi/h)}{(1 + 2\xi/h)^{1/2}}, \tag{6.6}$$

where $k = 2/3\sqrt{\rho b/\mu}$. When branching occurs the total mass flow rates must remain constant, i.e. $\dot{m}_0 = \sum_{n=1}^{N} \dot{m}_n$, and then Murray's Law (Eqn. 6.1) becomes

$$h_0^2 \frac{(1 + 3\xi/h_0)}{(1 + 2\xi/h_0)^{1/2}} = \sum_{n=1}^{N} h_n^2 \frac{(1 + 3\xi/h_n)}{(1 + 2\xi/h_n)^{1/2}}. \tag{6.7}$$

For a symmetric bifurcating channel, the mass flow rate through the parent channel must equal the total mass flow rate through the daughter channels, i.e. $\dot{m}_0 = 2\dot{m}_1$, therefore, the optimal ratio of channel widths becomes

$$\frac{h_0}{h_1} = \sqrt{2} \left(\frac{1 + 3\xi/h_1}{1 + 3\xi/h_0} \right)^{1/2} \left(\frac{1 + 2\xi/h_0}{1 + 2\xi/h_1} \right)^{1/4}. \tag{6.8}$$

It is clear that when h_0, $h_1 \gg \xi$ this becomes equation (6.2), as expected. It can also be noted that when the flow becomes plug like, i.e. h_0, $h_1 \ll \xi$, this ratio becomes $h_0/h_1 = 2^{2/3}$.

We can now use equations (6.3) and (6.8) to calculate the expected value of $h_0^2/2h_1^2$. When comparing this to the optimum found by the CFD we get excellent agreement, as seen in Figure 6.2. This shows that the slip at the walls is the important factor in the deviation from the expected optimum. A CFD model including an accurate model of the wall-fluid interaction is, therefore, potentially very important in designing nano-scale devices.

6.4 Optimum angle of bifurcation

Some lab-on-a-chip applications involve the flow of fluid through a Y-junction, therefore, an understanding of how slip boundary conditions affect the optimal design of the junction is required. In a follow-up paper to his original papers on optimal channel widths, Murray calculated the optimum angles that arteries branch at [100]. In this Section, we use the same derivation that Murray performed to find the optimal angle between branching channels, but use slip boundary conditions to find the influence that this has on the optimal branching angle. We then show how the optimal channel widths and branching angle changes with slip length.

We derive here an analytical solution of the optimum angle α for a 2D two-level network, see the geometry in Figure 6.3. For this derivation, we have a parent channel h_0 that branches into two daughter channels h_1 and h_2, these daughter channels branch at angles α and β, respectively. The derivation is performed by considering how making a small change to the lengths of the channels affects the

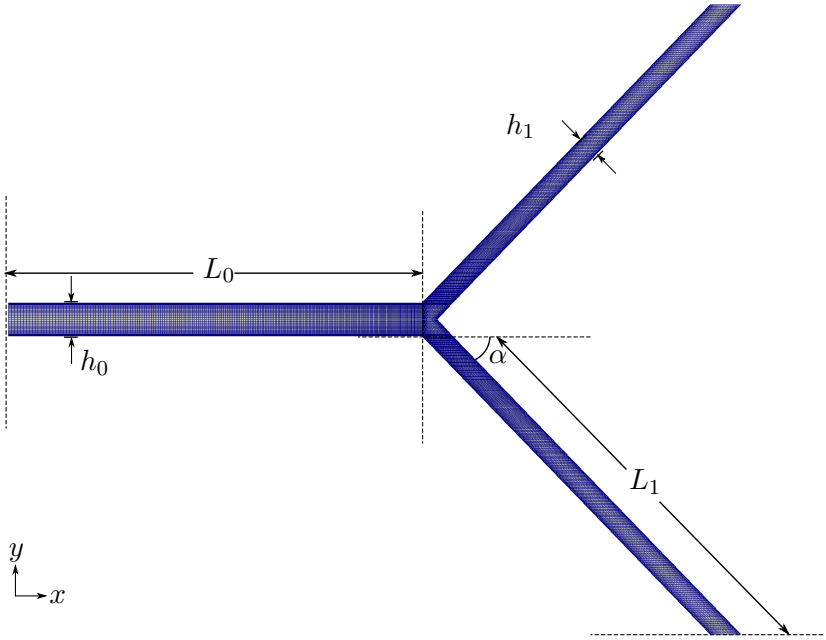

Figure 6.3: The bifurcating channel domain used for the design optimisation. The width of the parent channel is h_0; the width of the two daughter channels are h_1.

angle of branching, Figure 6.4. By doing this, we obtain three equations; not all three are truly required, as we have three equations and two unknowns α and β, but they make the derivation simpler. The three equations are

$$h_0 \mathrm{d}l_0 = \cos\alpha h_1 \mathrm{d}l_0 + \cos\beta h_2 \mathrm{d}l_0, \tag{6.9}$$

$$h_1 \mathrm{d}l_1 = -\cos(\alpha+\beta) h_2 \mathrm{d}l_1 + \cos\alpha h_0 \mathrm{d}l_1, \tag{6.10}$$

and

$$h_2 \mathrm{d}l_2 = -\cos(\alpha+\beta) h_0 \mathrm{d}l_2 + \cos\beta h_1 \mathrm{d}l_2. \tag{6.11}$$

These can be rearranged to give the following:

$$\cos\alpha = \frac{h_0^2 + h_1^2 - h_2^2}{2h_0h_1}, \tag{6.12}$$

$$\cos\beta = \frac{h_0^2 + h_2^2 - h_1^2}{2h_0h_2}, \tag{6.13}$$

and

$$\cos(\alpha+\beta) = \frac{h_0^2 - h_1^2 - h_2^2}{2h_1h_2}. \tag{6.14}$$

By assuming a symmetric bifurcation, i.e. $h_1 = h_2$ and $\alpha = \beta$, these equations are

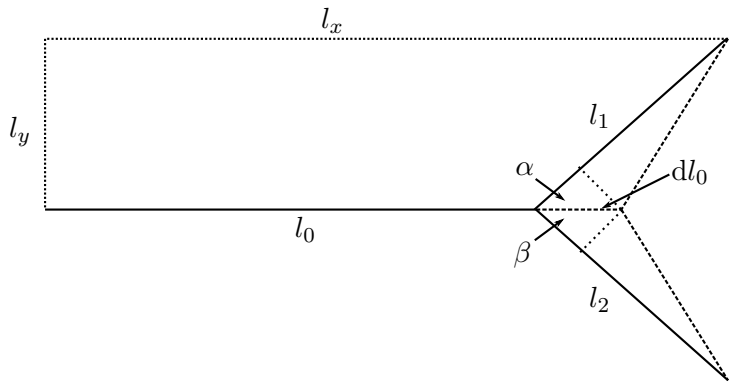

Figure 6.4: A schematic representation of a symetric bifurcation showing how it changes with a change in the length of l_0.

simplified to

$$\cos\alpha = \cos\beta = \frac{h_0}{2h_1} \tag{6.15}$$

and

$$\cos 2\alpha = \frac{h_0^2 - 2h_1^2}{2h_1^2}. \tag{6.16}$$

If we now also assume that there is no-slip at the walls, we can use equation (6.1) to find the optimum angle: $\alpha = \beta = \pi/4$. Whereas, if Navier slip boundary conditions are used, as in §6.3, then we can use equation (6.8) to find an equation for how the optimum angle changes with slip length:

$$\cos\alpha = \frac{\sqrt{2}}{2}\left(\frac{1+3\xi/h_1}{1+3\xi/h_0}\right)^{1/2}\left(\frac{1+2\xi/h_0}{1+2\xi/h_1}\right)^{1/4}. \tag{6.17}$$

Clearly, when $\xi = 0$ this gives the no-slip result. Also, at the plug-flow limit, when h_0, $h_1 \ll \xi$, we find that $\cos\alpha = 2^{-1/3}$.

We perform a design optimisation procedure on the geometry in Figure 6.3 using incompressible CFD for different values slip length between 0 and 50 nm. We assume that the optimal widths of the channels are independent of the optimal angle of bifurcation, therefore, we can, firstly, find the optimal widths of the channels and then optimise for the angle of bifurcation. The optimisation is performed by using a conjugate gradient optimization, with the given constraints of constant volume and fixed pressure difference, we find the maximum mass flow rate. We choose a volume of 1100 nm^3, a pressure difference of 20 MPa. The position of the inlet and outlets are fixed. The center of the inlet is set at (0, 0) the outlets are fixed at (l_x, $\pm l_y$), where $l_x = 130\,\mathrm{nm}$ $l_y = 57\,\mathrm{nm}$. The lengths of the channels can be calculated as

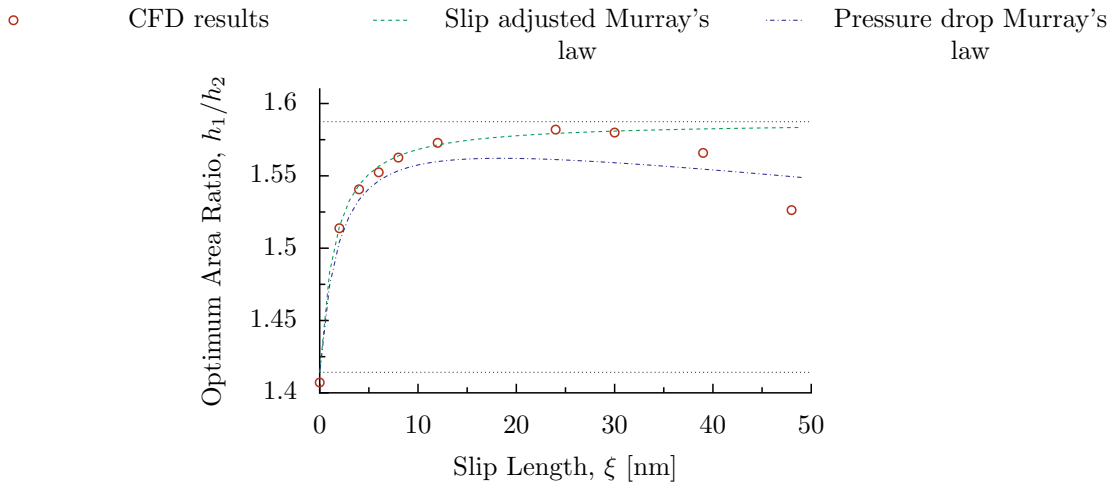

Figure 6.5: How the optimum area ratio h_0/h_1 changes with slip length ξ

$l_0 = l_x - l_y/\tan\alpha$ and $l_1 = l_y/\sin\alpha$, therefore, the volume V of the network can be calculated as:

$$V = h_0\left(l_x - \frac{l_y}{\tan\alpha}\right) + \frac{2h_1 l_y}{\sin\alpha} + \frac{1}{2}h_0 h_1 \cos\alpha. \tag{6.18}$$

The analytical results are found by solving the three equations (6.8), (6.17) and (6.18) with chosen slip lengths, to find the three unknowns h_0, h_1 and α, using a non-linear solver.

Figure 6.5 shows how the optimum width ratio h_0/h_1 changes with increasing slip length. We find that the analytical results agree well with the CFD until the slip length is about 30 nm. At this point the optimum width ratio decreases rather than converging to an asymptote. Figure 6.6 shows how the optimum angle changes. In this case the agreement is poor, the no-slip CFD result is the same as Murray's results, but, as the slip length increase the deviation between the analytical result and the CFD increases. The probable reason for this deviation is that the pressure losses in the junction become dominant as the slip length increases — in a similar way to the CNT case in the previous chapter. In Figure 6.7 we show how the pressure varies along the parent channel for an example case for various slip lengths. It can be seen that as the slip length increases the pressure loss becomes significantly higher.

We can test this hypothesis by estimating the pressure drop due to a junction Δp_j in a network by

$$\Delta p_j = \frac{\rho \bar{v}^2 K}{2}, \tag{6.19}$$

where K is a pressure loss coefficient (this is geometry dependant) and $\bar{v}$ is the

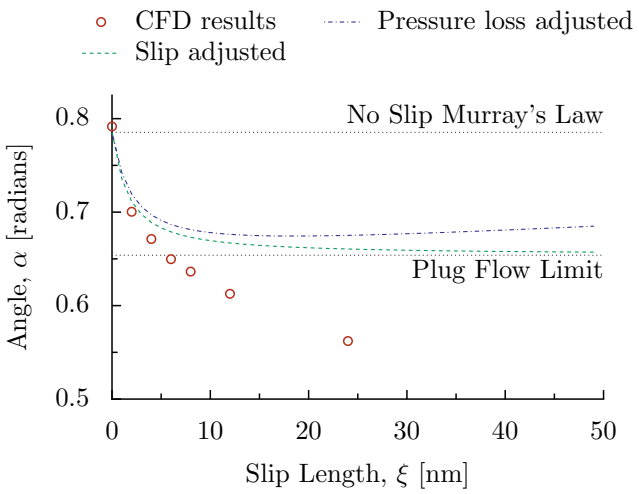

Figure 6.6: optimum angle α changes with slip length ξ

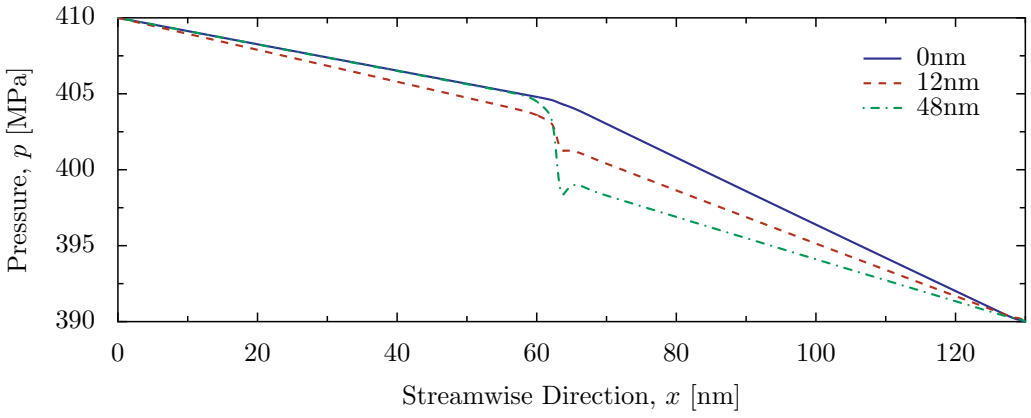

Figure 6.7: Liquid pressure along the center of the parent channel and then up though the center of a daughter channel of an example network. Each line represents the pressure variation for a different slip length.

average velocity. We can approximate $\bar{v}$ as

$$\bar{v} = \frac{\dot{m}}{\rho h_0}. \tag{6.20}$$

It is then possible to write an equation for the flow resistance R, across the whole network:

$$R = \frac{\Delta p}{\dot{m}} = \frac{3\mu l_0}{2\rho h_0^3(1 + 3\xi/h_0)} + \frac{3\mu l_1}{4\rho h_1^3(1 + 3\xi/h_1)} + \frac{\dot{m}K}{2\rho h_0^2}. \tag{6.21}$$

If we say the volume of the network is

$$V = h_0 l_0 + 2h_1 l_1 \tag{6.22}$$

then we can say $h_1 = a - bh_0$, where $a = V/2l_1$ and $b = l_0/2l_1$. By doing this we can now eliminate h_1 and minimise the flow resistance, i.e. $\mathrm{d}R/\mathrm{d}h_0 = 0$, to obtain

$$\frac{(1 + 2\xi/h_0)}{h_0^4(1 + 3\xi/h_0)^2} = \frac{(1 + 2\xi/h_1)}{4h_1^4(1 + 3\xi/h_1)^2} + \frac{2\dot{m}K}{9\mu h_0^3 l_0}. \tag{6.23}$$

As required, when $K = 0$ this becomes equation (6.8). We solve equations (6.21), (6.22) and (6.23) with $K = 25$. We plot the optimal widths against slip length in Figure 6.5. This equation does not give a good agreement due to the crude approximations made, but it does show that the pressure loss at the junction can have a significant effect on the optimum geometry.

6.5 Summary

We demonstrate the enhanced CFD approach applied to a design optimisation problem: that of a bifurcating nanofluidic network. The widths of channels in the network are optimised to maximise mass flow rate through the network, for a fixed pressure drop and network volume. We have shown that the influence of slip at the nano-scale can have a very significant effect on the optimum channel dimensions, and have derived an analytical equation which corrects the well-known Murray's law to accommodate this. This is one of many possible cases where nano-scale flow effects modify the optimal design of nanofluidic systems from their macroscopic counterparts. However, we also found that as mass flow rate increases with the slip length, pressure losses at the junction can dominate, and significantly influence the optimal network design.

Chapter 7

Conclusion and future work

In recent years there has been much excitement and study in nanofluidic technologies because of the potentially revolutionary applications that they could provide. However, there are challenges in accurately and efficiently performing numerical modelling of these technologies, which is holding them back. We have developed a 'sequential' hybrid molecular dynamics (MD)-computational fluid dynamics (CFD) model, which uses a single framework of MD simulations to provide constitutive relationships and boundary conditions for the CFD. This framework provides a more efficient method of modelling nanofluidic applications so that engineering relevant problems can be studied and solved.

We discussed different possible methodologies to obtain the required data for CFD simulations from MD simulations. We chose to make the method as general as possible by using non-equilibrium MD simulations, therefore it is capable of obtaining non-linear behaviour of fluids that occur far from equilibrium. It would be possible to use equilibrium MD simulations if the problem being studied does not deviate far from equilibrium and only linear behaviour of fluid properties is important; this could make obtaining the relationships required more efficient.

Once the data has been obtained from the MD simulations they have to be processed into a form that can be input into the CFD simulations. We developed a partial slip boundary condition for the CFD based on the shear rate dependence found by Thompson and Troian [143], but also incorporating a linear dependence on fluid density. We also incorporated a non-linear equation of state and equation of viscosity by fitting second-order polynomials to the MD results.

We gave a discussion of the impact of incorporating a surface displacement into our CFD model. This displacement is used to alter the width of a channel so that the CFD is only modelling where the fluid is, thereby not including the depletion

layer. We developed a simple measure to approximate how large a channel would need to be for this surface displacement to not affect the mass flow rate significantly. We found that for 2D channels the width must be greater than 75 nm for the mass flow rate to change by less than 1 %, and for a cylinder the radius must be greater than 100 nm.

We validated this new hybrid model against full MD simulations for different non-trivial geometries for steady and unsteady flows. We found that our model was capable of accurately predicting the steady-state mass flow rate through channels that could be used as a filtration membrane, while showing that other CFD models are incapable of this. We also found that our enhanced CFD model was capable of predicting transient behaviour of fluid flowing through a converging-diverging channel, with different gravity-type forces applied. Four different forces were tested to guarantee that the model was able to predict fast and slow variations in the mass flow rate.

The model was then applied to the three-dimensional case of water flow through a CNT. We were able to obtain reasonable predictions of fluid properties despite the size of the channel being near the continuum limit and the geometry that the slip was being applied to varying from the geometry that it was measured from. We demonstrated that the high mass flow rate, caused by the high slip length, is the cause of the high pressure losses that occur at the inlet and outlet of CNTs, by comparing no-slip and partial slip solutions. These pressure losses hinder the mass flow rate through the channel, therefore, the ability to reduce these losses could improve the flow rate even more. Possible ways to do this are to have curved entrance and exits or to apply an electric field to the entrance and exit [125].

Finally we applied the enhanced CFD model to the classic design optimisation problem of branching channels, which is relevant for lab-on-a-chip applications. The geometry of the network is optimised to maximise the mass flow rate through the network, for a fixed pressure drop and network volume. The classic solution to this problem is known as Murray's law [101, 102]. We found that the slip boundary conditions at the wall have a significant impact on the optimal design of the network. We derived a alternative form of Murray's law to accommodate this influence. In similarity with the CNT case, we found that as the mass flow rate increases with slip length, a significant pressure loss at the junction of the branching occurs. These losses also affect the optimal geometry of the network but more work is required to correctly predict this behaviour analytically.

There is still significant future work to develop the model to make it applicable to a variety of different applications and make it more efficient. Some of these

possibilities are:

- The acquisition of the parameter models for the CFD could be made more efficient by using machine learning techniques. This would minimize the number of simulations that must be performed to obtain an accurate model of the required boundary conditions and constitutive relations.
- A more rigorous definition of the surface displacement could be developed to guarantee its accuracy.
- The geometry dependence of different parameters needs to be studied and characterised further. Such as curvature dependence of slip length and geometry dependence of surface displacement. This would make the model more applicable and accurate for a higher variety of problems.
- In some applications, such as in nanomedicine [117], complex molecules are manipulated and analysed. These are non-Newtonian fluids and would require extending the pre-simulation framework to obtain extensional viscosity. A possible way to do this is to use the SLLOD NEMD equations [39, 148, 37].
- Many applications of nanofluidic devices control the flow using electrokinetics rather than being pressure driven because the pressure gradients required to obtain a high enough flow rate have to be excessively higher than would be industrially viable [117]. In addition, many applications involve the manipulation of ions within the fluid, such as water purification through CNTs [3] and ion separation [113]. These models can be modelled by coupling the Nernst-Plank equations, the Poisson-Boltzman equations and the Navier-Stokes equations [78, 69].
- The CFD model could easily be extended to model multiphase problems. However, this would require obtaining data for each fluid and interface properties (e.g. surface tension) between each fluid from the pre-simulations. This would introduce a substantial computational overhead.
- More work needs to be done to study the effects slip boundary conditions and other nanofluidic properties have on design optimisation. For example, the effect that the slip length and, in turn, the effect that high pressure losses at junctions have on optimal parameters of the geometry.

Bibliography

[1] J. L. F. Abascal and C. Vega. A general purpose model for the condensed phases of water: TIP4P/2005. *The Journal of Chemical Physics*, 123(23):234505, 2005.

[2] B. J. Alder and T. E. Wainwright. Studies in molecular dynamics. I. General method. *The Journal of Chemical Physics*, 31(2):459–466, 1959.

[3] A. Alexiadis and S. Kassinos. Molecular simulation of water in carbon nanotubes. *Chemical Reviews*, 108(12):5014–5034, 2008.

[4] A. Alexiadis, D. A. Lockerby, M. K. Borg, and J. M. Reese. A laplacian-based algorithm for non-isothermal atomistic-continuum hybrid simulation of micro and nano-flows. *Computer Methods in Applied Mechanics and Engineering*, 264(0):81–94, 2013.

[5] M. P. Allen and D. J. Tildesley. *Computer Simulation of Liquids*. Oxford Science Publ. Oxford University Press, 1989.

[6] H. C. Andersen. Molecular dynamics simulations at constant pressure and/or temperature. *The Journal of Chemical Physics*, 72(4):2384–2393, 1980.

[7] P. Angelikopoulos, C. Papadimitriou, and P. Koumoutsakos. Data driven, predictive molecular dynamics for nanoscale flow simulations under uncertainty. *The Journal of Physical Chemistry B*, 117(47):14808–14816, 2013.

[8] N. Asproulis and D. Drikakis. Wall-mass effects on hydrodynamic boundary slip. *Physical Review E*, 84(3):031504, 2011.

[9] N. Asproulis, M. Kalweit, and D. Drikakis. A hybrid molecular continuum method using point wise coupling. *Advances in Engineering Software*, 46(1):85–92, 2012.

[10] H. J. C. Berendsen, J. R. Grigera, and T. P. Straatsma. The missing term in effective pair potentials. *Journal of Physical Chemistry*, 91(24):6269–6271, 1987.

[11] H. J. C. Berendsen, J. P. M. Postma, W. F. van Gunsteren, A. DiNola, and J. R. Haak. Molecular dynamics with coupling to an external bath. *The Journal of Chemical Physics*, 81(8):3684–3690, 1984.

[12] H. J.C. Berendsen, J. P. M. Postma, W. F. Van Gunsteren, and J. Hermans. Interaction models for water in relation to protein hydration. In *Intermolecular Forces*, pages 331–342. Springer, 1981.

[13] S. Bernardi, B. D. Todd, and D. J. Searles. Thermostating highly confined fluids. *The Journal of Chemical Physics*, 132(24):244706, 2010.

[14] I. T. K. M. Bitsanis, T. K. Vanderlick, M. Tirrell, and H. T. Davis. A tractable molecular theory of flow in strongly inhomogeneous fluids. *The Journal of Chemical Physics*, 89(5):3152, 1988.

[15] L. Bocquet and J.-L. Barrat. Hydrodynamic boundary conditions, correlation functions, and kubo relations for confined fluids. *Physical Review E*, 49(4):3079, 1994.

[16] L. Bocquet and J.-L. Barrat. Flow boundary conditions from nano- to micro-scales. *Soft Matter*, 3(6):685–693, 2007.

[17] L. Bocquet and E. Charlaix. Nanofluidics, from bulk to interfaces. *Chemical Society Reviews*, 39(3):1073–1095, 2010.

[18] M. K. Borg. *Hybrid Molecular-Continuum Modelling of Nano-Scale Flows*. PhD thesis, University of Strathclyde, 2010.

[19] M. K. Borg, D. A. Lockerby, and J. M. Reese. Fluid simulations with atomistic resolution: a hybrid multiscale method with field-wise coupling. *Journal of Computational Physics*, 255:149–165, 2013.

[20] M. K. Borg, D. A. Lockerby, and J. M. Reese. A hybrid molecular-continuum simulation method for incompressible flows in micro/nanofluidic networks. *Microfluidics and Nanofluidics*, 15(4):541–557, 2013.

[21] M. K. Borg, D. A. Lockerby, and J. M. Reese. A multiscale method for micro/nano flows of high aspect ratio. *Journal of Computational Physics*, 233(0):400–413, 2013.

[22] M. K. Borg, D. A. Lockerby, and J. M. Reese. The FADE mass-stat: a technique for inserting or deleting particles in molecular dynamics simulations. *The Journal of Chemical Physics*, 140(7):074110, 2014.

[23] M. K. Borg, G. B. Macpherson, and J. M. Reese. Controllers for imposing continuum-to-molecular boundary conditions in arbitrary fluid flow geometries. *Molecular Simulation*, 36(10):745–757, 2010.

[24] J. L. Bouvard, D. K. Ward, D. Hossain, S. Nouranian, E. B. Marin, and M. F. Horstemeyer. Review of hierarchical multiscale modeling to describe the mechanical behavior of amorphous polymers. *Journal of Engineering Materials and Technology*, 131(4):041206, 2009.

[25] P. J. Cadusch, B. D. Todd, J. Zhang, and P. J Daivis. A non-local hydrodynamic model for the shear viscosity of confined fluids: analysis of a homogeneous kernel. *Journal of Physics A: Mathematical and Theoretical*, 41(3):035501, 2008.

[26] A. N. Chatterjee and N. R. Aluru. Combined circuit/device modeling and simulation of integrated microfluidic systems. *Microelectromechanical Systems, Journal of*, 14(1):81–95, 2005.

[27] C. C. Cruickshank, R. F. Minchin, A. C. Le Dain, and B. Martinac. Estimation of the pore size of the large-conductance mechanosensitive ion channel of escherichia coli. *Biophysical Journal*, 73(4):1925, 1997.

[28] W. A. Curtin and R. E. Miller. Atomistic/continuum coupling in computational materials science. *Modelling and Simulation in Materials Science and Engineering*, 11(3):R33, 2003.

[29] P. J. Daivis and B. D. Todd. A simple, direct derivation and proof of the validity of the sllod equations of motion for generalized homogeneous flows. *The Journal of Chemical Physics*, 124(19):194103, 2006.

[30] G. De Fabritiis, M. Serrano, R. Delgado-Buscalioni, and P. V. Coveney. Fluctuating hydrodynamic modeling of fluids at the nanoscale. *Physical Review E*, 75(2):026307, 2007.

[31] R. Delgado-Buscalioni and P. V. Coveney. Continuum-particle hybrid coupling for mass, momentum, and energy transfers in unsteady fluid flow. *Physical Review E*, 67(4):046704, 2003.

[32] R. Delgado-Buscalioni and P. V. Coveney. USHER: an algorithm for particle insertion in dense fluids. *The Journal of Chemical Physics*, 119(2):978–987, 2003.

[33] R. Delgado-Buscalioni, E. G. Flekkøy, and P. V. Coveney. Fluctuations and continuity in particle-continuum hybrid simulations of unsteady flows based on flux-exchange. *Europhysics Letters*, 69(6):959, 2005.

[34] S. Y. Docherty, W. D. Nicholls, M. K. Borg, D. A Lockerby, and J. M. Reese. Boundary conditions for molecular dynamics simulations of water transport through nanotubes. *Proceedings of the Institution of Mechanical Engineers, Part C: Journal of Mechanical Engineering Science*, 228(1):186–195, 2014.

[35] W. E and B. Engquist. The heterognous multiscale methods. *Communications in Mathematical Sciences*, 1(1):87–132, 2003.

[36] W. E, W. Ren, and E. Vanden-Eijnden. A general strategy for designing seamless multiscale methods. *Journal of Computational Physics*, 228(15):5437–5453, 2009.

[37] B. J. Edwards and M. Dressler. A reversible problem in non-equilibrium thermodynamics: Hamiltonian evolution equations for non-equilibrium molecular dynamics simulations. *Journal of Non-Newtonian Fluid Mechanics*, 96(1):163–175, 2001.

[38] D. R. Emerson, K. Cieślicki, X. Gu, and R. W. Barber. Biomimetic design of microfluidic manifolds based on a generalised Murray's law. *Lab on a Chip*, 6(3):447–454, 2006.

[39] D. J. Evans, E. G. D. Cohen, and G. P. Morriss. Viscosity of a simple fluid from its maximal lyapunov exponents. *Physical Review A*, 42(10):5990, 1990.

[40] J. H. Ferziger and M. Perić. *Computational methods for fluid dynamics*, volume 3. Springer Berlin, 2002.

[41] E. G. Flekkøy, G. Wagner, and J. Feder. Hybrid model for combined particle and continuum dynamics. *Europhysics Letters*, 52(3):271, 2000.

[42] D. Frenkel and B. Smit. *Understanding molecular simulation: from algorithms to applications*, volume 1. Academic press, 2001.

[43] M. Gad-el Hak. *MEMS: Introduction and Fundamentals*. CRC press, 2010.

[44] M. Gărăjeu, H. Gouin, and G. Saccomandi. Scaling navier-stokes equation in nanotubes. *Physics of Fluids*, 25(8):082003, 2013.

[45] J. W. Gibbs. *Elementary principles in statistical mechanics: developed with especial reference to the rational foundation of thermodynamics*. New York: Charles Scribner's Sons, 1902.

[46] L. Gosselin and A. K. da Silva. Constructal microchannel networks of rarefied gas with minimal flow resistance. *Journal of Applied Physics*, 101(11):114902, 2007.

[47] L. Grinberg, M. Deng, G. E. Karniadakis, and A. Yakhot. Window proper orthogonal decomposition: Application to continuum and atomistic data. In *Reduced Order Methods for Modeling and Computational Reduction*, pages 275–303. Springer, 2014.

[48] B. Guillot. A reappraisal of what we have learnt during three decades of computer simulations on water. *Journal of Molecular Liquids*, 101(1):219–260, 2002.

[49] N. G. Hadjiconstantinou. Discussion of recent developments in hybrid atomistic-continuum methods for multiscale hydrodynamics. *Technical Sciences*, 53(4):335–342, 2005.

[50] N. G. Hadjiconstantinou, A. L. Garcia, M. Z. Bazant, and G. He. Statistical error in particle simulations of hydrodynamic phenomena. *Journal of Computational Physics*, 187(1):274–297, 2003.

[51] N. G. Hadjiconstantinou and A. T. Patera. Heterogeneous atomistic-continuum representations for dense fluid systems. *International Journal of Modern Physics C*, 08(04):967–976, 1997.

[52] J.-P. Hansen and I. R. McDonald. *Theory of simple liquids*. Elsevier, 1990.

[53] S. C. Harvey. Treatment of electrostatic effects in macromolecular modeling. *Proteins: Structure, Function, and Bioinformatics*, 5(1):78–92, 1989.

[54] S. C. Harvey, R. K.-Z. Tan, and T. E. Cheatham. The flying ice cube: velocity rescaling in molecular dynamics leads to violation of energy equipartition. *Journal of Computational Chemistry*, 19(7):726–740, 1998.

[55] J. He and C. Song. Evaluation of pedestrian winds in urban area by numerical approach. *Journal of Wind Engineering and Industrial Aerodynamics*, 81(1):295–309, 1999.

[56] J. K. Holt. Methods for probing water at the nanoscale. *Microfluidics and Nanofluidics*, 5(4):425–442, 2008.

[57] J. K. Holt, H. G. Park, Y. Wang, M. Stadermann, A. B. Artyukhin, C. P. Grigoropoulos, A. Noy, and O. Bakajin. Fast mass transport through sub-2-nanometer carbon nanotubes. *Science*, 312(5776):1034–1037, 2006.

[58] M. F. Horstemeyer and P. Wang. Cradle-to-grave simulation-based design incorporating multiscale microstructure-property modeling: Reinvigorating design with science. *Journal of Computer-Aided Materials Design*, 10(1):13–34, 2003.

[59] C. Huang, P. Y. Choi, K. Nandakumar, and L. W. Kostiuk. Comparative study between continuum and atomistic approaches of liquid flow through a finite length cylindrical nanopore. *The Journal of Chemical Physics*, 126(22):224702–224702, 2007.

[60] D. M. Huang, C. Sendner, D. Horinek, R. R. Netz, and L. Bocquet. Water slippage versus contact angle: A quasiuniversal relationship. *Physical Review Letters*, 101(22):226101, 2008.

[61] D. J. Huggins. Correlations in liquid water for the TIP3P-Ewald, TIP4P-2005, TIP5P-Ewald, and SWM4-NDP models. *The Journal of Chemical Physics*, 136(6):064518, 2012.

[62] J. H. Irving and J. G. Kirkwood. The statistical mechanical theory of transport processes. iv. the equations of hydrodynamics. *The Journal of Chemical Physics*, 18:817–829, 1950.

[63] J. Jamali and S. Nabati. Shoghl. Computational fluid dynamics modeling of fluid flow and heat transfer in the central pore of carbon nanopipes. *RSC Advances*, 4(101):57958–57966, 2014.

[64] W. L. Jorgensen, J. Chandrasekhar, J. D. Madura, R. W. Impey, and M. L. Klein. Comparison of simple potential functions for simulating liquid water. *The Journal of Chemical Physics*, 79(2):926–935, 1983.

[65] W. L. Jorgensen and J. D. Madura. Temperature and size dependence for monte carlo simulations of TIP4P water. *Molecular Physics*, 56(6):1381–1392, 1985.

[66] S. Joseph and N. R. Aluru. Hierarchical multiscale simulation of electrokinetic transport in silica nanochannels at the point of zero charge. *Langmuir*, 22(21):9041–9051, 2006.

[67] S. Joseph and N. R. Aluru. Why are carbon nanotubes fast transporters of water? *Nano Letters*, 8(2):452–458, 2008.

[68] M. Kalweit and D. Drikakis. Coupling strategies for hybrid molecular-continuum simulation methods. *Proceedings of the Institution of Mechanical Engineers, Part C: Journal of Mechanical Engineering Science*, 222(5):797–806, 2008.

[69] G. Karniadakis, A. Beskok, and N. Aluru. *Microflows and nanoflows: fundamentals and simulation*, volume 29. Springer, 2006.

[70] M. B. Kerby, M. Spaid, S. Wu, J. W. Parce, and R.-L. Chien. Selective ion extraction: a separation method for microfluidic devices. *Analytical Chemistry*, 74(20):5175–5183, 2002.

[71] I. G. Kevrekidis, C. W. Gear, and G. Hummer. Equation-free: The computer-aided analysis of complex multiscale systems. *AIChE Journal*, 50(7):1346–1355, 2004.

[72] I. G. Kevrekidis, C. W. Gear, J. M. Hyman, P. G. Kevrekidid, O. Runborg, and C. Theodoropoulos. Equation-free, coarse-grained multiscale computation: Enabling mocroscopic simulators to perform system-level analysis. *Communications in Mathematical Sciences*, 1(4):715–762, 2003.

[73] S. Kohlhoff and S. Schmauder. A new method for coupled elastic-atomistic modelling. In *Atomistic Simulation of Materials*, pages 411–418. Springer, 1989.

[74] K. Kremer and F. Müller-Plathe. Multiscale problems in polymer science: simulation approaches. *MRS bulletin*, 26(03):205–210, 2001.

[75] R Kubo. The fluctuation-dissipation theorem. *Reports on Progress in Physics*, 29(1):255, 1966.

[76] T.-C. Kuo, D. M. Cannon, Y. Chen, J. J. Tulock, M. A. Shannon, J. V. Sweedler, and P. W. Bohn. Gateable nanofluidic interconnects for multilayered microfluidic separation systems. *Analytical Chemistry*, 75(8):1861–1867, 2003.

[77] M. Levitt and A. Warshel. Computer simulation of protein folding. *Nature*, 253(5494):694–698, 1975.

[78] D. Li. *Electrokinetics in microfluidics*, volume 2. Academic Press, 2004.

[79] J. Li, D. Liao, and S. Yip. Coupling continuum to molecular-dynamics simulation: Reflecting particle method and the field estimator. *Physical Review E*, 57(6):7259, 1998.

[80] J. Li, D. Liao, and S. Yip. Imposing field boundary conditions in MD simulation of fluids: optimal particle controller and buffer zone feedback. volume 538, page 473. MRS Proceedings, 1998.

[81] J. Li, D. Liao, and S. Yip. Nearly exact solution for coupled continuum/md fluid simulation. *Journal of Computer-Aided Materials Design*, 6(2-3):95–102, 1999.

[82] J. Li, C. Papadopoulos, and J. Xu. Nanoelectronics: Growing y-junction carbon nanotubes. *Nature*, 402(6759):253–254, 1999.

[83] P. J. Linstrom and W. G. Mallard. NIST chemistry webbook; NIST standard reference database no. 69. 2001. `http://webbook.nist.gov`.

[84] P.-L. Lions. On the schwarz alternating method. I. In *First international symposium on domain decomposition methods for partial differential equations*. Paris, France, 1988.

[85] W. K. Liu, H. S. Park, D. Qian, E. G. Karpov, H. Kadowaki, and G. J. Wagner. Bridging scale methods for nanomechanics and materials. *Computer Methods in Applied Mechanics and Engineering*, 195(13–16):1407–1421, 2006.

[86] D. A. Lockerby, C. A. Duque-Daza, M. K. Borg, and J. M. Reese. Time-step coupling for hybrid simulations of multiscale flows. *Journal of Computational Physics*, 237:344–365, 2013.

[87] D. A. Lockerby, A. Patronis, M. K. Borg, and J. M. Reese. Asynchronous coupling of hybrid models for efficient simulation of multiscale systems. *Journal of Computational Physics*, 284, 2015.

[88] D. A. Lockerby and J. M. Reese. On the modelling of isothermal gas flows at the microscale. *Journal of Fluid Mechanics*, 604:235–261, 2008.

[89] G. B. Macpherson, M. K. Borg, and J. M. Reese. Generation of initial molecular dynamics configurations in arbitrary geometries and in parallel. *Molecular Simulation*, 33(15):1199–1212, 2007.

[90] G. B. Macpherson and J. M. Reese. Molecular dynamics in arbitrary geometries: parallel evaluation of pair forces. *Molecular Simulation*, 34(1):97–115, 2008.

[91] M. W. Mahoney and W. L. Jorgensen. A five-site model for liquid water and the reproduction of the density anomaly by rigid, nonpolarizable potential functions. *The Journal of Chemical Physics*, 112(20):8910–8922, 2000.

[92] M. Majumder, N. Chopra, R. Andrews, and B. J. Hinds. Nanoscale hydrodynamics: enhanced flow in carbon nanotubes. *Nature*, 438(7064):44–44, 2005.

[93] D. Mantzalis, N. Asproulis, and D. Drikakis. Filtering carbon dioxide through carbon nanotubes. *Chemical Physics Letters*, 506(1):81–85, 2011.

[94] A. Martini, H.-Y. Hsu, N. A. Patankar, and S. Lichter. Slip at high shear rates. *Physical Review Letters*, 100(20):206001, 2008.

[95] D. Mattia and F. Calabrò. Explaining high flow rate of water in carbon nanotubes via solid–liquid molecular interactions. *Microfluidics and Nanofluidics*, 13(1):125–130, 2012.

[96] D. Mattia and Y. Gogotsi. Review: static and dynamic behavior of liquids inside carbon nanotubes. *Microfluidics and Nanofluidics*, 5(3):289–305, 2008.

[97] K. A. McCulloh, J. S. Sperry, and F. R. Adler. Water transport in plants obeys Murray's law. *Nature*, 421(6926):939–942, 2003.

[98] D. L. McDowell. A perspective on trends in multiscale plasticity. *International Journal of Plasticity*, 26(9):1280–1309, 2010.

[99] K. M. Mohamed and A. A. Mohamad. A review of the development of hybrid atomistic–continuum methods for dense fluids. *Microfluidics and Nanofluidics*, 8(3):283–302, 2010.

[100] C. D. Murray. The physiological principle of minimum work applied to the angle of branching of arteries. *The Journal of General Physiology*, 9(6):835–841, 1926.

[101] C. D. Murray. The physiological principle of minimum work: I. The vascular system and the cost of blood volume. *Proceedings of the National Academy of Sciences of the United States of America*, 12(3):207, 1926.

[102] C. D. Murray. The physiological principle of minimum work: II. Oxygen exchange in capillaries. *Proceedings of the National Academy of Sciences of the United States of America*, 12(5):299, 1926.

[103] W. D. Nicholls. *Molecular Dynamics Simulations of Liquid Flow in and around Carbon Nanotubes*. PhD thesis, University of Strathclyde, 2012.

[104] W. D. Nicholls, M. K. Borg, D. A. Lockerby, and J. M. Reese. Water transport through (7, 7) carbon nanotubes of different lengths using molecular dynamics. *Microfluidics and Nanofluidics*, 12(1-4):257–264, 2012.

[105] W. D. Nicholls, M. K. Borg, D. A. Lockerby, and J. M. Reese. Water transport through carbon nanotubes with defects. *Molecular Simulation*, 38(10):781–785, 2012.

[106] X. B. Nie, S. Y. Chen, and M. O. Robbins. A continuum and molecular dynamics hybrid method for micro-and nano-fluid flow. *Journal of Fluid Mechanics*, 500:55–64, 2004.

[107] S. Nosé. A unified formulation of the constant temperature molecular dynamics methods. *The Journal of Chemical Physics*, 81(1):511–519, 1984.

[108] S. T. O'Connell and P. A. Thompson. Molecular dynamics-continuum hybrid computations: A tool for studying complex fluid flows. *Physical Review E*, 52:R5792–R5795, 1995.

[109] L. Onsager and S. Machlup. Fluctuations and irreversible processes. *Physical Review*, 91(6):1505, 1953.

[110] OpenFOAM. Programmer's guide, Version 2.3.1, 2014.

[111] OpenFOAM. User guide, Version 2.3.1, 2014.

[112] OpenFOAM. The open source CFD toolbox. http://www.openfoam.org, 2015.

[113] J. H. Park, S. B. Sinnott, and N. R. Aluru. Ion separation using a Y-junction carbon nanotube. *Nanotechnology*, 17(3):895, 2006.

[114] M. Parrinello and A. Rahman. Crystal structure and pair potentials: A molecular-dynamics study. *Physical Review Letters*, 45(14):1196, 1980.

[115] A. Patronis, D. A. Lockerby, M. K. Borg, and J. M. Reese. Hybrid continuum–molecular modelling of multiscale internal gas flows. *Journal of Computational Physics*, 255:558–571, 2013.

[116] A. Popadić, J. H. Walther, P. Koumoutsakos, and M. Praprotnik. Continuum simulations of water flow in carbon nanotube membranes. *New Journal of Physics*, 16(8):082001, 2014.

[117] S. Prakash, A. Piruska, E. N. Gatimu, P. W. Bohn, J. V. Sweedler, and M. A. Shannon. Nanofluidics: systems and applications. *Sensors Journal, IEEE*, 8(5):441–450, 2008.

[118] N. V. Priezjev. Rate-dependent slip boundary conditions for simple fluids. *Physical Review E*, 75(5):051605, 2007.

[119] N. V. Priezjev and S. M. Troian. Molecular origin and dynamic behavior of slip in sheared polymer films. *Physical Review Letters*, 92(1):018302, 2004.

[120] X. Qin, Q. Yuan, Y. Zhao, S. Xie, and Z. Liu. Measurement of the rate of water translocation through carbon nanotubes. *Nano Letters*, 11(5):2173–2177, 2011.

[121] D.C. Rapaport. *The Art of Molecular Dynamics Simulation*. Cambridge University Press, 2004.

[122] J. C. Rasaiah, S. Garde, and G. Hummer. Water in nonpolar confinement: From nanotubes to proteins and beyond. *Annual Review Physical Chemistry*, 59:713–740, 2008.

[123] J. M. Reese, M. A. Gallis, and D. A. Lockerby. New directions in fluid dynamics: non-equilibrium aerodynamic and microsystem flows. *Philosophical Transactions of the Royal Society of London. Series A: Mathematical, Physical and Engineering Sciences*, 361(1813):2967–2988, 2003.

[124] W. Ren and W. E. Heterogeneous multiscale method for the modeling of complex fluids and micro-fluidics. *Journal of Computational Physics*, 204(1):1–26, 2005.

[125] K. Ritos. *Water flow at the nanoscale: a computational molecular and fluid dynamics investigation*. PhD thesis, University of Strathclyde, 2014.

[126] K. Ritos, D. Mattia, F. Calabró, and J. M. Reese. Flow enhancement in nanotubes of different materials and lengths. *The Journal of Chemical Physics*, 140(1):014702, 2014.

[127] R. J. Sadus. *Molecular simulation of fluids*. Elsevier, 2002.

[128] R. Saidur, K. Y. Leong, and H. A. Mohammad. A review on applications and challenges of nanofluids. *Renewable and Sustainable Energy Reviews*, 15:1646–1668, 2011.

[129] M. Salloum, K. Sargsyan, R. Jones, B. Debusschere, H. N. Najm, and H. Adalsteinsson. A stochastic multiscale coupling scheme to account for sampling noise in atomistic-to-continuum simulations. *Multiscale Modeling & Simulation*, 10(2):550–584, 2012.

[130] R. A. Sampson. On stokes's current function. *Philosophical Transactions of the Royal Society of London A: Mathematical, Physical and Engineering Sciences*, 182:449–518, 1891.

[131] C. Sendner, D. Horinek, L. Bocquet, and R. R. Netz. Interfacial water at hydrophobic and hydrophilic surfaces: Slip, viscosity, and diffusion. *Langmuir*, 25(18):10768–10781, 2009.

[132] M. E. Sheehan and P. N. Sharratt. Molecular dynamics methodology for the study of the solvent effects on a concentrated diels-alder reaction and the separation of the post-reaction mixture. *Computers & Chemical Engineering*, 22:S27–S33, 1998.

[133] T. B. Sisan and S. Lichter. The end of nanochannels. *Microfluidics and Nanofluidics*, 11(6):787–791, 2011.

[134] F. Sofos, T. Karakasidis, and A. Liakopoulos. Transport properties of liquid argon in krypton nanochannels: Anisotropy and non-homogeneity introduced by the solid walls. *International Journal of Heat and Mass Transfer*, 52(3–4):735–743, 2009.

[135] C. C. S. Song and M. Yuan. A weakly compressible flow model and rapid convergence methods. *Journal of Fluids Engineering*, 110(4):441–445, 1988.

[136] D. Stephenson, D. A. Lockerby, M. K. Borg, and J. M. Reese. Multiscale simulation of nanofluidic networks of arbitrary complexity. *Microfluidics and Nanofluidics*, 2014.

[137] M. E. Suk and N. R. Aluru. Water transport through ultrathin graphene. *The Journal of Physical Chemistry Letters*, 1(10):1590–1594, 2010.

[138] M. E. Suk and N. R. Aluru. Molecular and continuum hydrodynamics in graphene nanopores. *RSC Advances*, 3(24):9365–9372, 2013.

[139] D. N. Theodorou. Understanding and predicting structure–property relations in polymeric materials through molecular simulations. *Molecular Physics*, 102(2):147–166, 2004.

[140] J. A. Thomas and A. J. H. McGaughey. Water flow in carbon nanotubes: transition to subcontinuum transport. *Physical Review Letters*, 102(18):184502, 2009.

[141] M. Thomas and B. Corry. Thermostat choice significantly influences water flow rates in molecular dynamics studies of carbon nanotubes. *Microfluidics and Nanofluidics*, 18(1):41–47, 2015.

[142] P. A. Thompson and M. O. Robbins. Shear flow near solids: Epitaxial order and flow boundary conditions. *Physical Review A*, 41(12):6830, 1990.

[143] P. A. Thompson and S. M. Troian. A general boundary condition for liquid flow at solid surfaces. *Nature*, 389(6649):360–362, 1997.

[144] D. P. Tieleman, H. Leontiadou, A. E. Mark, and S.-J. Marrink. Simulation of pore formation in lipid bilayers by mechanical stress and electric fields. *Journal of the American Chemical Society*, 125(21):6382–6383, 2003.

[145] B. D. Todd. Cats, maps and nanoflows: some recent developments in nonequilibrium nanofluidics. *Molecular Simulation*, 31(6-7):411–428, 2005.

[146] B. D. Todd, J. S. Hansen, and P. J. Daivis. Nonlocal shear stress for homogeneous fluids. *Physical Review Letters*, 100(19):195901, 2008.

[147] K. P. Travis, B. D. Todd, and D. J. Evans. Departure from Navier-Stokes hydrodynamics in confined liquids. *Physical Review E*, 55(4):4288, 1997.

[148] M. E. Tuckerman, C. J. Mundy, S. Balasubramanian, and M. L. Klein. Modified nonequilibrium molecular dynamics for fluid flows with energy conservation. *The Journal of Chemical Physics*, 106(13):5615–5621, 1997.

[149] C. Vega and J. L. F. Abascal. Simulating water with rigid non-polarizable models: a general perspective. *Physical Chemistry Chemical Physics*, 13(44):19663–19688, 2011.

[150] L. Verlet. Computer "experiments" on classical fluids. I. Thermodynamical properties of Lennard-Jones molecules. *Physical Review*, 159(1):98, 1967.

[151] H. K. Versteeg and W. Malalasekera. *An introduction to computational fluid dynamics: the finite volume method*. Pearson Education, 2007.

[152] O. I. Vinogradova. Drainage of a thin liquid film confined between hydrophobic surfaces. *Langmuir*, 11(6):2213–2220, 1995.

[153] J. H. Walther, K. Ritos, E. R. Cruz-Chu, C. M. Megaridis, and P. Koumoutsakos. Barriers to superfast water transport in carbon nanotube membranes. *Nano Letters*, 13(5):1910–1914, 2013.

[154] L. Wang, R. S. Dumont, and J. M. Dickson. Nonequilibrium molecular dynamics simulation of water transport through carbon nanotube membranes at low pressure. *The Journal of Chemical Physics*, 137:044102, 2012.

[155] H. L. Weissberg. End correction for slow viscous flow through long tubes. *Physics of Fluids*, 5(9):1033–1036, 1962.

[156] D. Wen, G. Lin, S. Vafaei, and K. Zhang. Review of nanofluids for heat transfer applications. *Particuology*, 7(2):141–150, 2009.

[157] T. Werder, J. H. Walther, and P. Koumoutsakos. Hybrid atomistic–continuum method for the simulation of dense fluid flows. *Journal of Computational Physics*, 205(1):373–390, 2005.

[158] M. Whitby and N. Quirke. Fluid flow in carbon nanotubes and nanopipes. *Nature Nanotechnology*, 2(2):87–94, 2007.

[159] S. Yasuda and R. Yamamoto. A model for hybrid simulations of molecular dynamics and computational fluid dynamics. *Physics of Fluids*, 20(11):113101, 2008.

[160] D. M. York, T. A. Darden, and L. G. Pedersen. The effect of long-range electrostatic interactions in simulations of macromolecular crystals: a comparison of the ewald and truncated list methods. *The Journal of Chemical Physics*, 99(10):8345–8348, 1993.

[161] H. Zhang, Z. Zhang, and H. Ye. Molecular dynamics-based prediction of boundary slip of fluids in nanochannels. *Microfluidics and Nanofluidics*, 12(1-4):107–115, 2012.